Development of Magnetorotation as a Signal Transduction Method for Protein Detection

by

Ariel Hecht

A dissertation submitted in partial fulfillment
of the requirements for the degree of
Doctor of Philosophy
(Biomedical Engineering)
in the University of Michigan
2013

Doctoral Committee:

Professor Raoul Kopelman, Chair
Associate Professor Xudong Fan
Professor Ari Gafni
Professor Robert T. Kennedy
Professor Shuichi Takayama

To my parents,

for everything.

Acknowledgments

First and foremost, I would like to begin by thanking my advisor, Dr. Raoul Kopelman, for his support and guidance over the past five years. Completing this degree has been among the most challenging and rewarding things I've ever done. From our starting point five years ago, we went through many unexpected twists and turns on the journey to our destination. It would not have been possible to navigate this voyage without Dr. Kopelman's sage assistance, and for this I am extremely grateful.

I would next like to thank my committee members, Dr. Fan, Dr. Gafni, Dr. Kennedy, and Dr. Takayama, for their advice, support and feedback over the past several years. It has been a pleasure working with them, and I am very grateful for their service. Dr. Alan Hunt served on my committee until his sudden and untimely passing in the fall of 2012. It was a pleasure to work with him, and I would like to thank him for his service and acknowledge his contributions to this dissertation.

Daily life in the lab would not have been possible without the wonderful support and assistance from, and the occasional watching of midday soccer games with, my labmates. Specifically, I would like to thank Taey Curry, Remy Elbez, Kristen Herrmann, Lesh Karamchand, and Ani Ray for being wonderful friends and the best labmates. Coming to lab every day would not be the same without all of you, I am very fortunate to have had such terrific colleagues.

Over the past few years, I have had the honor and privilege of mentoring two wonderful students, Nicholas Shah and Patrick Commiskey. They are wonderful scientists, whose talents and skills were essential in the completion of this thesis. They were a pleasure to work with, brought joy and enthusiasm with them to work every day, and I wish them much success in their future endeavors.

Before coming to Michigan, I was very fortunate to have had many incredible teachers and mentors. I would like to thank my 9th grade Biology teacher, Ms. Marla Weiss, who first opened me up to the world of science, and was one of the best teachers I ever had. I would like to thank Dr. Richard Casaburi and Dr. Janos Porszasz of the Los Angeles Biomedical Research Institute, who gave me my first research experience as a post-high school summer intern. They gave me my first opportunity to do research, they gave me the freedom to explore and develop my skills, and their belief in me helped me believe in myself. At UCLA, Dr. Tim Deming and Dr. Chih-Ming Ho took me into their labs, and gave me very valuable research experiences. At Sandia National Labs, Dr. Greg Sommer and Dr. Anson Hatch provided me with a wonderful summer internship experience that very fortuitously introduced me to aptamers and led to key developments in my research at Michigan. Finally, I owe an insurmountable debt of gratitude to Dr. Daniel Kamei of UCLA, who for the past nine years has been the kind of mentor, teacher, and friend that most students dream about. His support, friendship and assistance have been invaluable to me in my personal and professional development, and for this I am eternally grateful.

I'm not really sure how best to thank my friends, who have been there for me for so many years, through countless adventures, and have meant so much to me, so I will

simply say to Max Landaw, Aaron Filene, Phil Mehdipour, and Ben Chapman, keep in touch. CPM. To Eric Livak-Dahl, I hope you finally make it onto the wall at Ashley's.

Finally, I would like to thank the most important people in my life, my family, for putting up with me for all these years, and for providing with me so much love and support. I would like to thank my grandparents for their sage wisdom, perspective and advice. My discussions with them have always been so valuable to me. I would like to thank my little brother Avi, and my little sister, Vivian, for being the best little siblings that anyone could ever ask for. Don't worry; I'm not going to mention that thing that I promised I wasn't going to mention. And finally, my parents. They raised me with so much love, always guided me in the right direction, and helped me make it through every stage in life. They provided me with every opportunity one could ever hope for, and they are the primary support behind any of my accomplishments. For all of the little things, like enforcing *sitzfleisch* when I didn't want to do my homework, teaching me how to drive stick, or helping me proofread my entire thesis in under a week, and for all of the big things, which I don't even need to mention here, my parents have been there for me, at every step of the way, and I dedicate this thesis to them.

Table of Contents

List of Figures

List of Tables

List of Appendices

Abstract

The concentration of protein biomarkers in the bloodstream can be an effective indicator of disease processes. Rapid, simple, portable and inexpensive diagnostic devices can improve healthcare by increasing access to protein-based diagnostic technologies, shifting them from centralized laboratories to decentralized point-of-care locations. This dissertation describes the development of two signal transductions methods, Label-Acquired Magnetorotation (LAM), and its successor, Bead Assembly Magnetorotation (BAM) as a magnetic bead-based signal transduction mechanism for decentralized protein diagnostic applications. LAM and BAM use the concentration of the target protein to mediate the formation of a magnetic bead assembly. LAM is performed by taking 1 μm magnetic beads and 10 μm nonmagnetic spheres, functionalizing them with affinity molecules against the target protein, mixing them with a solution containing the protein, and then allowing the protein to mediate the attachment of the 1 μm magnetic beads to the 10 μm nonmagnetic spheres. In an asynchronously rotating magnetic field, the rotational frequency of the nonmagnetic sphere depends on the number of attached magnetic beads, which depends on the concentration of the protein. BAM is performed by taking the same functionalized 1 μm magnetic beads, mixing them with a solution containing the protein, and then plating 1 μL inverted droplets of the solution on a Teflon-coated slide. As the beads fall through the solution to the bottom of the droplet, the protein mediates the formation of the beads into an

assembly. In the case of high protein concentration, the beads form a loosely-packed assembly. In the case of no or low protein concentration, and the beads form a tightly-packed assembly. In an asynchronously rotating magnetic field, the rotational period of the assembly will depend on its packing density, which depends on the concentration of the protein. This thesis discusses the development of LAM and BAM, where BAM yields one of the lowest limits of detection ever reported for the protein thrombin. Additionally, it discusses the development of a portable laser-and-photodiode diagnostic platform prototype, as well as attempts to translate BAM into serum. A separate project shows the use of aptamers as affinity molecules for a gel electrophoresis platform.

Chapter 1

Introduction

The concentration of certain key proteins in the bloodstream can yield insight into disease and other physiological processes. [1, 2] The goal of a protein diagnostic system is to rapidly and accurately measure the concentration of these proteins. Reducing the size, cost, analysis time, and the complexity of these diagnostic systems could increase the accessibility of these technologies to greater segments of the population, by moving them from centralized laboratories to decentralized point-of-care locations. [3, 4] There are three primary components in a protein diagnostic system: the target protein that the system is attempting to detect, the affinity molecules used to capture the target, and the signal transduction mechanism by which a successful binding event is transduced into a signal that can be quantified and recorded by the user. The focus of this thesis is on the third part of these systems, the signal transduction mechanism.

There are a wide variety of signal transduction mechanisms currently in use, including fluorescent probes, [5-10] electrochemistry, [11-18] surface plasmon resonance (SPR), [19-22] and a number of magnetic-based methods, including giant magnetoresistance (GMR), [23-27], magnetic relaxation (MR), [28-31] and Hall probes. [32-34]

The primary challenge associated with using fluorescent probes as signal transducers is the cost of the detection apparatus, [35] and the primary challenge

associated with using electrochemistry as the signal transducer is false positives, due to electrolytes and nonspecific signals generated by proteins and other molecules found in biological fluids. [36] Of the magnetic signal transduction systems, none are currently in clinical use; all remain in the stage of laboratory development.

This dissertation focuses on the development of a novel protein diagnostic signal transduction mechanism based on the asynchronous magnetic rotation of magnetic beads, using aptamers as affinity molecules, as well as on a project demonstrating the use of aptamers as affinity reagents in an integrated electrophoretic lab-on-a-chip platform. This introductory chapter discusses affinity molecules, other key protein diagnostic systems currently in clinical use and laboratory development, and the theory of asynchronous magnetic rotation.

Affinity Molecules

Affinity molecules are molecules that bind with high specificity and selectivity to a molecular target, such as a protein or other small biomolecule. [2] The most common type of affinity molecule is an antibody, which is a protein that binds to its molecular target. Antibodies for research applications are produced by injecting an animal such as a mouse, goat, sheep, or rabbit with the molecular target, which will cause the animal to produce the antibodies through its own immune system. The antibodies are then harvested from the animal's blood stream (polyclonal antibodies) or from lymphocytes which are isolated from the animal and cloned *in vitro* (monoclonal antibodies). [37, 38] Antibodies have in their structure a target-specific variable region, which binds to the

target by non-covalent interactions between the antibody's variable region and the epitope region on the target molecule.

Aptamers, unlike amino acids, are synthetically-generated affinity molecules that are composed of single- or double-stranded nucleic acid sequences, typically on the order of 15-100 base pairs. [39, 40] Like antibodies, aptamers bind to the epitope region of their target protein via non-covalent interactions between a part of the aptamer and the epitope. Most aptamers are derived through the SELEX (systematic evolution of ligands by exponential enrichment) process, where a randomly generated pool of oligonucleotides is mixed with the molecular target and oligonucleotides that display affinity for the target are separated and amplified repeatedly until the highest affinity oligonucleotides are isolated. [39, 41] Aptamers have several advantages over antibodies for diagnostic applications. Because they are synthetic, aptamers can be developed against any molecular target, without needing to use any animals. Once an aptamer sequence is identified, additional copies of the aptamer can be produced for approximately 100-1000 times lower cost than antibodies. Aptamers are also significantly more robust than antibodies, maintaining stability at room temperature for periods of weeks or even months. [42]

Two of the most popular aptamers are the thrombin aptamers, the first of which, the 15-mer, was discovered in 1992, [43] and the second of which, the 29-mer, was discovered in 1997. [44] The aptamers bind to the fibrin exosite (15-mer) and heparin exosite (29-mer) of the thrombin protein, which is a blood protein that is a component in the fibrin coagulation cascade. These aptamers were originally thought to have therapeutic application as anti-clotting agents. [43-45] However, when that therapeutic

potential failed to materialize, [46] the aptamers took on a second life as a sandwich pair of affinity molecules for diagnostic device development.

A sandwich pair is a pair of affinity molecules that bind to opposite sides of a protein target. Having a sandwich pair of affinity molecules (as opposed to using only a single affinity molecule) allows for two-step diagnostic systems: the first is the capture step, where the target is captured by a larger substrate; and the second is the detection step, where a label binds to the captured protein, allowing for the transduction of a signal. The advantage of this two-step method is the increased specificity of the system, reducing the rate of false positives. [47] Given that the thrombin aptamers were the only sandwich pair of aptamers available, and the numerous advantages of using aptamers listed above, the thrombin aptamers have become a very popular choice for demonstrating proof-of-principle of new diagnostic systems. [15-18, 48-61] For these same reasons the thrombin aptamers are the focus of most of the work in this dissertation. An added benefit of this choice is that it makes it easier to benchmark the work here against the work of others.

Another important set of affinity molecules are streptavidin and biotin. Streptavidin is a tetrameric protein (MW ~ 60 kDa) isolated from the bacteria *Streptomyces avidinii*, and biotin is a small molecule (MW ~ 244 Da), also known as Vitamin B7. [62] Streptavidin and biotin form the strongest non-covalent bond found in nature, with a dissociation constant on the order of 10^{-15} M. [63] Streptavidin and biotin have two primary uses within diagnostic systems: one is to serve as an affinity molecule system for very early stage system development, and the other is to facilitate conjugation reactions by coating one substrate with streptavidin, and coating the other with biotin.

Biodetection Methodologies

The gold standard in diagnostic assays is ELISA, the Enzyme Linked Immunosorbent Assay. Invented in the 1960s, ELISA has become the most popular method for performing diagnostic assays. The fundamental principle behind ELISA is to use the presence (or absence) of an enzymatic label, which binds to the target via an affinity molecule, to induce a colorimetric change in proportion to the concentration of the target protein. [64] There are several different types of ELISA assays that can be performed. Some of the more popular types are the indirect, direct and sandwich ELISA.

An indirect ELISA assay tests for the presence of antibodies against a specific antigen, rather than for the presence of the antigen itself. In an indirect ELISA, the antigen of interest is immobilized to the surface of a plate, after which a solution containing the target antibody is added to the plate. The target antibody binds to the antigen immobilized on the surface of the plate. The plate is washed to remove any unbound antibodies, and the enzyme-labeled secondary antibody is introduced. If the primary antibody was present in the original solution, then the enzymatically-labeled secondary antibody will bind to it, causing the desired color change to occur in the solution. If the primary antibody was not present, then the enzymatically-labeled secondary antibody will not remain in the solution, and the color change will not occur. If the test requires only a qualitative detection of color change (e.g. low, medium or high intensity), then visual observation is usually sufficient to yield an answer. If a quantitative result is required, then a plate reader is typically used to measure the intensity of the color signal in the solution. A direct ELISA is similar to an indirect ELISA, except the primary antibody is labeled with the enzyme, so that the secondary

antibody is not needed. Using two antibodies in an ELISA rather than just one typically result in greater specificity and lower rates of false positives.

A sandwich assay can be performed to detect either an antigen or an antibody, although it is most frequently used for antigen detection. The sandwich assay requires two antibodies against the target antigen, a capture antibody and a detection antibody. The capture antibody is immobilized to the surface of a plate. A solution containing the target antigen is added, allowed to incubate for a specified period of time, and then washed to remove any unbound antigen. The detection antibody is then introduced, which binds to any antigens that were captured in the first step. A washing step then removes any unbound detection antibody. Finally, an enzymatically-labeled secondary antibody is introduced, which binds specifically to any detection antibodies that are present. A washing step then removes any unbound secondary antibody. After the enzymes are allowed to react for a specified amount of time, the plate can be analyzed to determine the concentration of antigen that was present. Typically, a greater concentration of antigen will result in a greater color change.

Unlike ELISA-based sensors, which use a colorimetric or fluorescent change as the signal transduction mechanism, electrochemical sensors use changes in current as the signal transduction mechanism. [13] Electrochemical sensors are similar to ELISA-based sensors in that the target analyte is captured by an affinity molecule(s), but instead of being conjugated to an enzyme or molecule that produces a chromometric change, they are conjugated to an enzyme or molecule that produces an electrochemical change. There are several different classes of electrochemical sensors: amperometric, potentiometric, and impedimetric. Amperometric sensors use the product of a reduction or oxidation

reaction to generate the signal-transducing current. [11, 12] Potentiometric sensors use ion-selective electrodes to generate their signal-transducing currents. [14, 15] Impedimetric sensors use the binding of the target and associated labeling molecules to cause a change in the impedance of a conductor. [16, 17, 36] ELISA- and electrochemical-based biosensors are probably the two most popular classes of biosensor signal transduction methods.

Another class of biodetectors is capillary electrophoresis. In capillary electrophoresis, molecules are separated through a viscous medium (a gel or a fluid) by an electric field on the basis of differences in their charge-to-mass ratio. [65, 66] The target molecule is captured by a fluorescently-tagged affinity molecule, at which point two classes of fluorescent compounds exist in the solution: target-fluorophore complexes, and free fluorophore. These two compounds are separated in the electrophoretic gel on the basis of their different migration times, and are detected by a fluorescent detector at the end of the capillary. The capillaries used are typically microfluidic, which enables them to be miniaturized for point-of-care detection. [5, 41, 67]

There are several signal transduction methods that make use of magnetic particles, including giant magnetoresistance (GMR) and magnetic relaxation (MR). GMR is similar in concept to impedimetric electrochemical sensing. The surface of an electromagnetic sensor is functionalized with capture affinity molecules for the target. After the target is captured, detection affinity molecules functionalized with magnetic particles are introduced, and sandwich the target. The proximity of the particles to the sensor surface changes the resistivity of the sensor, which can be detected by passing a constant current through the sensor and measuring the change in the voltage across the sensor. [24, 68]

The most successful example of GMR is probably the work of Shan Wang. Using 50 nm magnetic nanoparticles with a sensor size of 100 μm, his group was able to detect the biomarkers TNF-α (tumor necrosis factor alpha), hCG (human chorionic gonadotropin), CEA (carcinoembryonic antigen), and IFN-γ (interferon gamma) at levels ranging from femtomolar in buffer to low picomolar in serum. [23]

Magnetic Relaxation is perhaps the method most similar to the work presented in this thesis. The MR detection method is based on functionalizing magnetic nanoparticles with affinity molecules against the target, and mixing them with a solution containing the target. The target will mediate the binding of the particles to each other to form clusters, with larger clusters corresponding to greater concentrations of protein. The signal is transduced by applying a strong, high-frequency magnetic field to the solution containing the particles, and measuring the relaxation time of the particles, which will depend on the size of the clusters that they form. [25, 30] The most successful example of MR is the work of Ralph Weissleder. The Weissleder group built an MR detection system using both 38 nm magnetic particles and 1 μm magnetic beads, and generated a 0.5 T, 21 MHz excitation field using a 1.25 kg permanent magnet, with microfabricated microcoils as the detection sensors. [28] The system was able to detect IgG in buffer below 1 pM, [69] and VEGF (vascular endothelial growth factor) in serum at 4.7 pM. [70]

Magnetism

There are three types of magnetic materials: ferromagnetic, paramagnetic, and diamagnetic. Ferromagnetic materials, such as iron, have a permanent magnetic moment that exists even in the absence of an external magnetic field. Paramagnetic materials do

not have a permanent magnetic moment, and exhibit a weak magnetic attraction only in the presence of an external magnetic field. Diamagnetic materials also do not have a permanent magnetic moment, and exhibit a weak magnetic repulsion only in the presence of an external magnetic field. [71] There is a special class of magnetic materials, called superparamagnetic, that is a combination of ferromagnetism and paramagnetism. A ferromagnetic material is composed of many small magnetic domains (typically on the order of tens of nanometers) that maintain their magnetic moment based on nearest-neighbor interactions. However, if a ferromagnetic material is broken up into very small segments, below the single domain size (~ 30 nm), then the domain no longer has any neighbors, and therefore it cannot maintain a permanent magnetic moment. In the presence of an external magnetic field, the domain will reassume the strong magnetic attraction (much stronger than typical paramagnetic attractions) associated with its multidomain version. Such materials are called superparamagnetic materials. [72] Superparamagnetic beads (micron-sized polystyrene beads with embedded 8-nm superparamagnetic iron oxide particles) are very useful for biological applications because they have no net magnetic moment, which allows for them to mix well in solution without clumping, and then when a field is applied, exhibit strong magnetization.

The rotation of a superparamagnetic bead in a rotating magnetic field can take place in two regimes: the synchronous regime, and the asynchronous regime. In the synchronous regime, the bead is phase locked with the field, and so rotates with the same period as the field. As the frequency of the field is increased beyond a critical frequency, the viscous drag forces opposing the rotation of the bead increase, such that the bead can no longer keep up with the rotation of the field, and it enters the asynchronous regime,

rotating with a non-constant phase lag relative to the field. [73, 74] The synchronous regime is less useful for making measurements, because the rate at which the bead rotates is fixed relative to that of the driving field. The asynchronous regime, however, is very useful for making measurements, because the rotational period of the bead depends on several parameters, including the volume, shape, and magnetic content of the bead. In this thesis we use the asynchronous magnetic rotation of superparamagnetic beads as signal transducers for measuring protein concentration.

Significant work in the theory of asynchronous magnetic rotation was done by Connolly and St. Pierre, [75] Fannin et. al, [76] and Janssen et. al, [77] and much of the theoretical foundation of the work in this thesis was built upon their ideas. To describe the behavior of the beads, we start with the equation for magnetic torque, $\boldsymbol{\tau} = \mathbf{m} \times \mathbf{B}$, where **m** is the magnetic moment of the bead, and **B** is the strength of the external magnetic field. Assuming steady state rotation, the rotational driving forces are equal in magnitude and opposite in direction to the viscous drag forces. Setting up a torque balance, the drag term can be expanded, $\tau = \kappa \eta V_H / T$, where κ is the shape factor, η is the fluid viscosity, V_H is the hydrodynamic volume, and T is the rotational period. The rotational driving forces can be expanded with the following substitutions, $\mathbf{B} = \mu_0 \mathbf{H}$, where μ_0 is the permeability of free space, **H** is the magnetizing field; $\mathbf{m} = V_m \mathbf{M}$, where V_m is the volume of magnetic material, and **M** is the volumetric magnetic moment; $\mathbf{M} = \chi \mathbf{H}$, where χ is the magnetic susceptibility of the bead; and $\chi = \chi' - i\chi''$, where χ' is the real component of the bead susceptibility, and χ'' is the imaginary component of the bead susceptibility. We can combine all of these expressions to create an equation for the rotational period of the bead:

$$T = \frac{\kappa \eta V_H}{\mu_0 V_m \chi'' H^2} \tag{1.1}$$

This equation can be expressed in terms of experimentally measurable parameters by making further substitutions: $\chi'' = \chi_0 \left(\Omega \tau_N\right) / \left(1 + \Omega^2 \tau_N^2\right)$, where χ_0 is the DC bead susceptibility, Ω is the frequency of the driving field, and τ_N is the Neel relaxation time; $\tau_N = \exp\left\{\left(KV_p\right) / \left(k_B T_K\right)\right\}$, where K is the magnetic anisotropy constant, V_p is the volume of the magnetic nanoparticles, k_B is Boltzmann's constant and T_K is the ambient temperature. These expressions can be combined to produce a single equation that describes the asynchronous rotation of a superparamagnetic bead in a rotating magnetic field.

$$T = \kappa \eta V_H \frac{1}{\mu_0 V_m H^2} \frac{\sum_n V_n^2}{\chi_0} \frac{1}{\sum_n \Omega \tau_0 \exp\left(\frac{KV_p}{k_B T_K}\right) V_n^2} \tag{1.2}$$

The asynchronous rotation of magnetic beads has been used for a variety of other sensing applications, including measuring solution viscosity, [74] pH, [78] the growth of single bacteria, [73, 79-83] and cancer cells. [84] Additional examples include measuring the binding of bacteriophage by Brownian relaxation of magnetic beads, [29, 31, 85, 86] the rotation of analyte-linked magnetic particle chains, [87-90] and fluorescently-labeled rotating bead immunosensing. [91]

Chapter Summaries

This thesis will discuss the development of the rotation of magnetic bead assemblies as a signal transduction mechanism for the detection of proteins. It will trace its development from inception, through two different generations, (1) the sandwich complex and (2) the bead assembly, with both biotin and thrombin as the detection targets; the development of a laser-and-photodiode setup to perform off-microscope detection; and fractal analysis. It concludes with a discussion about performance in serum and possibilities for future work.

Chapter 2 will discuss the beginning of the idea of magnetorotation for biosensing, Label-Acquired Magnetorotation (LAM). LAM involves two primary components: a 10 μm nonmagnetic "mother sphere," and a 1 μm superparamagnetic "daughter bead." The mother sphere and daughter bead are coated with a sandwich pair of affinity molecules. The mother sphere is labeled with the capture molecule, and the daughter bead is labeled with the detection molecule. In the performance of LAM, a solution containing the mother spheres is mixed with a solution containing the target of interest. After this initial capture step, the detection step is performed by the addition of the superparamagnetic daughter beads to the solution. If the target has been captured on the surface of the mother spheres, the daughter beads will bind to the target on the surface of the mother sphere. In this manner, the mother sphere is covered with labeling daughter beads in proportion to the concentration of protein in solution. The mother sphere has "acquired" the daughter beads through the presence of the target bound to its surface. In a rotating magnetic field, the rotational frequency of a mother sphere is proportional to the number of daughter beads attached to it. Specifically, the target was a 40 nm biotinylated

nanoparticle, and the affinity molecules were streptavidin. This biotin-streptavidin setup was used to mimic the presence of a real affinity-molecule—protein pair, for the initial development and proof-of-principle of this concept.

Chapter 3 extends LAM to the next step by using a real affinity-molecule—protein pair. The protein thrombin, a blood coagulation co-factor, along with two aptamers, known as the 15-mer and the 29-mer, against thrombin as the affinity molecules, are used. The same basic mother sphere and daughter bead LAM model of Chapter 2 is used. Results are shown with a limit of detection (LOD) down to below 1 nM in buffer for thrombin. Additionally, simulation results are shown showing the potential for improvement in the system.

Chapter 4 introduces a new model, called Bead Assembly Magnetorotation (BAM), which is the second generation of LAM. The same thrombin and aptamer system from Chapter 3 is used. The 10 μm mother sphere is removed from the system, and only 1 μm daughter beads are used. Half of the daughter beads are coated with the capture aptamer, and the other half of the daughter beads are coated with the detection aptamer. Instead of creating many mother spheres with beads attached to them, an inverted droplet is used to concentrate all the beads in the droplet into a single assembly, composed of between hundreds to thousands of beads. The size and shape of the assembly determine its response to a rotating magnetic field. If the concentration of the protein in solution is high, then as the beads fall to the center of the droplet, they will bind to each other, and be unable to tightly aggregate at the center of the droplet; the assembly will be loosely packed, with a lot of void space within it. If the concentration of the protein is low, then as the beads fall to the center of the droplet, they will not bind to each other via thrombin

chains, but will reach the center of the droplet and the assembly will be densely packed. The higher the packing density of the assembly, the greater its rotational period in a rotating magnetic field will be. This method was shown to be extremely sensitive, with a limit of detection of 80 fM in buffer, which is one of the lowest ever reported with this very popular aptamer-protein pair. In addition to magnetorotation, a second signal transduction mechanism was developed, fractal analysis. By performing an analysis of images of the bead assemblies, the fractal dimension and lacunarity could be determined, which proved as well to be good indicators of the concentration of protein in solution, though with a higher LOD. Finally, a laser-and-photodiode setup was developed, to allow for portable, microscope-free detection of magnetorotation. This setup proved to be robust, and could form the basis for the development of a portable point-of-care detection setup for the performance of BAM.

Chapter 5 discusses the attempts to translate BAM to serum analysis. The final step in demonstrating the potential of BAM as a clinically relevant technology is its translation into serum. The experiments described in the previous three chapters were performed in buffer, but for the work described in this chapter we attempt to perform BAM in serum. The primary challenge with working in serum is mitigating nonspecific interactions between serum proteins and the beads. The strategy we used to mitigate these interactions was functionalizing the beads with poly(ethylene glycol) (PEG). PEG is an extremely hydrophilic molecule that is frequently used for this purpose. PEG was shown to be fairly effective at mitigating interactions between serum proteins and the beads. However, significant nonspecific-binding interactions also occurred between the aptamers and serum proteins, which were harder to mitigate, and which we believe are

due to the basic structure of the thrombin aptamers. Due to the high level of nonspecific binding between the aptamer and the serum proteins, the LOD was reduced by about four orders of magnitude when transitioning from buffer to serum; however, BAM still remained competitive with the leading reports of thrombin detection in serum. An unexpected challenge was encountered due to the collapse of the assemblies during magnetorotation, which we suspect is due to the high flexibility of the PEG molecule compared to the relatively rigid aptamer.

Chapter 6 discusses a project that is different from the rest of the work in this dissertation. As part of the conditions of the fellowship which supported the first three years of my research at Michigan, I spent a summer as an intern at Sandia National Labs in Livermore, CA. While there, I explored a concept related to the rest of the work in this dissertation, which is the use of aptamers in capillary electrophoresis, which is a different type of signal transduction mechanism. This project is connected to the rest of the work in this dissertation because it studied aptamers for diagnostic purposes, and the challenges associated with their use in serum. The knowledge and understanding of aptamers that was gained in this project informed much of the work that was conducted in the rest of this dissertation. This project studied the role of aptamers as affinity reagents in capillary electrophoresis towards an integrated lab-on-a-chip platform. The target analyte being studied was the nuclear transcription factor NF-κB. The affinity molecule used was a single fluorescently-labeled aptamer. This project shows that aptamers are generally better suited than antibodies to be affinity molecules in capillary electrophoresis, because they typically posses a much smaller mass than antibodies (approximately 10-20 kDa for aptamers, 150 kDa for antibodies). Since capillary

electrophoresis is based on the difference between the mass of the free affinity molecule and the mass of the affinity molecule-target complex, a smaller affinity molecule results in better signal resolution. Additionally, the problem of nonspecific interference from serum proteins was solved by the addition of an excess of nonspecific aptamer. Finally, the use of an on-chip preconcentration membrane was shown to increase the sensitivity of the system.

At the end of this dissertation, two appendices are included that discuss additional experimental avenues that were explored. The first discusses attempts to perform BAM in larger droplets, which calculations suggested would lower the LOD, but were unsuccessful due to the presence of convection currents within these larger droplets. The addition of glycerol to the droplets as a way to mitigate the currents was investigated. The second discusses the exploration of two potential signal transduction methods, the angles between adjacent beads within an assembly, and the radius of gyration of the assembly, that ultimately were not as useful as the other methods discussed in this dissertation.

Overall the work presented in this dissertation discusses the development of magnetorotation as a protein diagnostic tool, as well as some of the challenges associated with using aptamers as affinity reagents in serum, and potential strategies for mitigating them. The LOD obtained for the protein thrombin in buffer is one of the best LODs reported for this protein-aptamer combination, which demonstrates the potential of magnetorotation as a diagnostic tool.

References

1. Yager, P., T. Edwards, E. Fu, K. Helton, et al. Microfluidic diagnostic technologies for global public health. *Nature*, 2006. **442**(7101): p. 412-418.
2. Wild, D., The Immunoassay handbook. 2nd ed. 2001, London: Nature Pub. Group. xxix, 906 p.
3. Yager, P., G.J. Domingo, and J. Gerdes. Point-of-Care Diagnostics for Global Health. *Annual Review of Biomedical Engineering*, 2008. **10**(1): p. 107-144.
4. Sia, S. and L. Kricka. Microfluidics and point-of-care testing. *Lab Chip*, 2008. **8**: p. 1982-1983.
5. Meagher, R.J., A.V. Hatch, R.F. Renzi, and A.K. Singh. An integrated microfluidic platform for sensitive and rapid detection of biological toxins. *Lab on a Chip*, 2008. **8**(12): p. 2046-2053.
6. Hayes, M.A., M.M. Petkus, A.A. Garcia, T. Taylor, et al. Demonstration of sandwich and competitive modulated supraparticle fluoroimmunoassay applied to cardiac protein biomarker myoglobin. *Analyst*, 2009. **134**(3): p. 533-541.
7. Song, M., Y. Zhang, T. Li, Z. Wang, et al. Highly sensitive detection of human thrombin in serum by affinity capillary electrophoresis/laser-induced fluorescence polarization using aptamers as probes. *Journal of Chromatography A*, 2009. **1216**(5): p. 873-878.
8. Tennico, Y.H., D. Hutanu, M.T. Koesdjojo, C.M. Bartel, et al. On-Chip Aptamer-Based Sandwich Assay for Thrombin Detection Employing Magnetic Beads and Quantum Dots. *Analytical Chemistry*, 2010. **82**(13): p. 5591-5597.
9. Alivisatos, A.P. Semiconductor Clusters, Nanocrystals, and Quantum Dots. *Science*, 1996. **271**(5251): p. 933-937.
10. Grant, S.A., M.E. Pierce, D.J. Lichlyter, and D.A. Grant. Effects of immobilization on a FRET immunosensor for the detection of myocardial infarction. *Analytical and Bioanalytical Chemistry*, 2005. **381**(5): p. 1012-1018.
11. Ferapontova, E.E., E.M. Olsen, and K.V. Gothelf. An RNA aptamer-based electrochemical biosensor for detection of theophylline in serum. *J. Am. Chem. Soc.*, 2008. **130**: p. 4256-4258.
12. Lai, R.Y., K.M. Plaxco, and A.J. Heeger. Aptamer-based electrochemical detection of picomolar platelet-derived growth factor directly in blood-serum. *Anal. Chem.*, 2007. **79**: p. 229-233.
13. Wang, J. Electrochemical biosensors: Towards point-of-care cancer diagnostics. *Biosensors and Bioelectronics*, 2006. **21**(10): p. 1887-1892.
14. Lin, J. and H. Ju. Electrochemical and chemiluminescent immunosensors for tumor markers. *Biosensors and Bioelectronics*, 2005. **20**(8): p. 1461-1470.

15. Hianik, T., V. Ostatná, Z. Zajacová, E. Stoikova, et al. Detection of aptamer-protein interactions using QCM and electrochemical indicator methods. *Bioorganic & Medicinal Chemistry Letters*, 2005. **15**(2): p. 291-295.

16. Zhang, Z., W. Yang, J. Wang, C. Yang, et al. A sensitive impedimetric thrombin aptasensor based on polyamidoamine dendrimer. *Talanta*, 2009. **78**(4-5): p. 1240-1245.

17. Cai, H., T.M.-H. Lee, and I.M. Hsing. Label-free protein recognition using an aptamer-based impedance measurement assay. *Sensors and Actuators B: Chemical*, 2006. **114**(1): p. 433-437.

18. Kim, K.S., H.-S. Lee, J.-A. Yang, M.-H. Jo, et al. The fabrication, characterization and application of aptamer-functionalized Si-nanowire FET biosensors. *Nanotechnology*, 2009. **20**(23): p. 235501.

19. Chinowsky, T.M., M.S. Grow, K.S. Johnston, K. Nelson, et al. Compact, high performance surface plasmon resonance imaging system. *Biosensors and Bioelectronics*, 2007. **22**(9-10): p. 2208-2215.

20. Huang, J.-G., C.-L. Lee, H.-M. Lin, T.-L. Chuang, et al. A miniaturized germanium-doped silicon dioxide-based surface plasmon resonance waveguide sensor for immunoassay detection. *Biosensors and Bioelectronics*, 2006. **22**(4): p. 519-525.

21. Seefeld, T.H., W.-J. Zhou, and R.M. Corn. Rapid Microarray Detection of DNA and Proteins in Microliter Volumes with Surface Plasmon Resonance Imaging Measurements. *Langmuir*, 2011. **27**(10): p. 6534-6540.

22. Soelberg, S.D., R.C. Stevens, A.P. Limaye, and C.E. Furlong. Surface Plasmon Resonance Detection Using Antibody-Linked Magnetic Nanoparticles for Analyte Capture, Purification, Concentration, and Signal Amplification. *Analytical Chemistry*, 2009. **81**(6): p. 2357-2363.

23. Osterfeld, S.J., H. Yu, R.S. Gaster, S. Caramuta, et al. Multiplex protein assays based on real-time magnetic nanotag sensing. *Proceedings of the National Academy of Sciences of the United States of America*, 2008. **105**(52): p. 20637-20640.

24. Wang, S.X. and L. Guanxiong. Advances in Giant Magnetoresistance Biosensors With Magnetic Nanoparticle Tags: Review and Outlook. *Magnetics, IEEE Transactions on*, 2008. **44**(7): p. 1687-1702.

25. Amalou, F. and M.A.M. Gijs. Giant magnetoimpedance of amorphous ribbon/Cu/amorphous ribbon trilayer microstructures. *Journal of Applied Physics*, 2004. **95**(3): p. 1364-1371.

26. Miller, M.M., P.E. Sheehan, R.L. Edelstein, C.R. Tamanaha, et al. A DNA array sensor utilizing magnetic microbeads and magnetoelectronic detection. *Journal of Magnetism and Magnetic Materials*, 2001. **225**(1-2): p. 138-144.

27. Edelstein, R.L., C.R. Tamanaha, P.E. Sheehan, M.M. Miller, et al. The BARC biosensor applied to the detection of biological warfare agents. *Biosensors & Bioelectronics*, 2000. **14**(10-11): p. 805-813.

28. Lee, H., E. Sun, D. Ham, and R. Weissleder. Chip-NMR biosensor for detection and molecular analysis of cells. *Nature Medicine*, 2008. **14**(8): p. 869-874.

29. Chung, S.H., A. Hoffmann, S.D. Bader, C. Liu, et al. Biological sensors based on Brownian relaxation of magnetic nanoparticles. *Applied Physics Letters*, 2004. **85**(14): p. 2971-2973.

30. Eberbeck, D., F. Wiekhorst, U. Steinhoff, and L. Trahms. Quantification of biomolecule agglutination by magnetorelaxometry. *Applied Physics Letters*, 2009. **95**(21): p. 213701.

31. Astalan, A.P., F. Ahrentorp, C. Johansson, K. Larsson, et al. Biomolecular reactions studied using changes in Brownian rotation dynamics of magnetic particles. *Biosensors & Bioelectronics*, 2004. **19**(8): p. 945-951.

32. Besse, P.-A., G. Boero, M. Demierre, V. Pott, et al. Detection of a single magnetic microbead using a miniaturized silicon Hall sensor. *Applied Physics Letters*, 2002. **80**(22): p. 4199-4201.

33. Sandhu, A., H. Handa, and M. Abe. Synthesis and applications of magnetic nanoparticles for biorecognition and point of care medical diagnostics. *Nanotechnology*, 2010. **21**(44): p. 442001.

34. Ejsing, L., M.F. Hansen, A.K. Menon, H.A. Ferreira, et al. Planar Hall effect sensor for magnetic micro- and nanobead detection. *Applied Physics Letters*, 2004. **84**(23): p. 4729-4731.

35. Mohammed, M.-I. and M.P.Y. Desmulliez. Lab-on-a-chip based immunosensor principles and technologies for the detection of cardiac biomarkers: a review. *Lab on a Chip*, 2011. **11**(4): p. 569-595.

36. Pohanka, M. and P. Skladal. Electrochemical biosensors--principles and applications. *Journal of Applied Biomedicine*, 2008. **6**: p. 57-64.

37. Cole, S.P.C., B.G. Campling, T. Atlaw, D. Kozbor, et al. Human monoclonal antibodies. *Molecular and Cellular Biochemistry*, 1984. **62**(2): p. 109-120.

38. Kabir, S. Immunoglobulin Purification By Affinity Chromatography Using Protein A Mimetic Ligands Prepared By Combinatorial Chemical Synthesis. *Immunological Investigations*, 2002. **31**(3-4): p. 263-278.

39. Turek, C. and L. Gold. Systematic evolution of ligands by exponential enrichment: RNA ligands to bacteriophage T4 DNA polymerase. *Science*, 1990. **249**: p. 505-510.

40. Ellington, A.D. and J.W. Szostak. In vitro selection of RNA molecules that bind specific ligands. *Nature*, 1990. **346**: p. 818-822.

41. Hecht, A.H., G.J. Sommer, R.H. Durland, X. Yang, et al. Aptamers as Affinity Reagents in an Integrated Electrophoretic Lab-on-a-Chip Platform. *Analytical Chemistry*, 2010. **82**(21): p. 8813-8820.

42. Jayasena, S.D. Aptamers: An emerging class of molecules that rival antibodies in diagnostics. *Clinical Chemistry*, 1999. **45**(9): p. 1628-1650.

43. Bock, L.C., L.C. Griffin, J.A. Latham, E.H. Vermaas, et al. Selection of single-stranded DNA molecules that bind and inhibit human thrombin. *Nature*, 1992. **355**(6360): p. 564-566.

44. Tasset, D.M., M.F. Kubik, and W. Steiner. Oligonucleotide inhibitors of human thrombin that bind distinct epitopes. *Journal of Molecular Biology*, 1997. **272**(5): p. 688-698.

45. Furie, B. and B.C. Furie. Thrombus formation in vivo. *The Journal of Clinical Investigation*, 2005. **115**(12): p. 3355-3362.

46. Osborne, S.E., I. Matsumura, and A.D. Ellington. Aptamers as therapeutic and diagnostic reagents: problems and prospects. *Current Opinion in Chemical Biology*, 1997. **1**(1): p. 5-9.

47. Nielsen, U.B. and B.H. Geierstanger. Multiplexed sandwich assays in microarray format. *Journal of Immunological Methods*, 2004. **290**(1–2): p. 107-120.

48. Centi, S., S. Tombelli, M. Minunni, and M. Mascini. Aptamer-Based Detection of Plasma Proteins by an Electrochemical Assay Coupled to Magnetic Beads. *Analytical Chemistry*, 2007. **79**(4): p. 1466-1473.

49. An, T., K.S. Kim, S.K. Hahn, and G. Lim. Real-time, step-wise, electrical detection of protein molecules using dielectrophoretically aligned SWNT-film FET aptasensors. *Lab on a Chip*, 2010. **10**(16): p. 2052-2056.

50. Cho, H., B.R. Baker, S. Wachsmann-Hogiu, C.V. Pagba, et al. Aptamer-Based SERRS Sensor for Thrombin Detection. *Nano Letters*, 2008. **8**(12): p. 4386-4390.

51. Hu, J., T. Wang, J. Kim, C. Shannon, et al. Quantitation of Femtomolar Protein Levels via Direct Readout with the Electrochemical Proximity Assay. *Journal of the American Chemical Society*, 2012. **134**(16): p. 7066-7072.

52. Jiang, L., R. Yuan, Y. Chai, Y. Yuan, et al. Aptamer-based highly sensitive electrochemical detection of thrombin via the amplification of graphene. *Analyst*, 2012. **137**(10): p. 2415-20.

53. Li, Y., L. Guo, F. Zhang, J. Tang, et al. High-sensitive determination of human a-thrombin by its 29-mer aptamer in affinity probe capillary electrophoresis. *Electrophoresis*, 2008. **29**: p. 2570-2577.

54. Liu, X., R. Aizen, R. Freeman, O. Yehezkeli, et al. Multiplexed aptasensors and amplified DNA sensors using functionalized graphene oxide: application for logic gate operations. *ACS Nano*, 2012. **6**(4): p. 3553-63.

55. Pavlov, V., Y. Xiao, B. Shlyahovsky, and I. Willner. Aptamer-Functionalized Au Nanoparticles for the Amplified Optical Detection of Thrombin. *Journal of the American Chemical Society*, 2004. **126**(38): p. 11768-11769.

56. Rahman, M.A., J.I. Son, M.S. Won, and Y.B. Shim. Gold nanoparticles doped conducting polymer nanorod electrodes: ferrocene catalyzed aptamer-based thrombin immunosensor. *Analytical Chemistry,* 2009. **81**(16): p. 6604-11.

57. Tang, J., D. Tang, R. Niessner, D. Knopp, et al. Hierarchical dendritic gold microstructure-based aptasensor for ultrasensitive electrochemical detection of thrombin using functionalized mesoporous silica nanospheres as signal tags. *Analytica Chimica Acta,* 2012. **720**: p. 1-8.

58. Xiao, Y., A.A. Lubin, A.J. Heeger, and K.W. Plaxco. Label-Free Electronic Detection of Thrombin in Blood Serum by Using an Aptamer-Based Sensor. *Angewandte Chemie*, 2005. **117**(34): p. 5592-5595.

59. Zhang, X., B. Qi, Y. Li, and S. Zhang. Amplified electrochemical aptasensor for thrombin based on bio-barcode method. *Biosensors & Bioelectronics,* 2009. **25**(1): p. 259-62.

60. Zhou, W.J., A.R. Halpern, T.H. Seefeld, and R.M. Corn. Near infrared surface plasmon resonance phase imaging and nanoparticle-enhanced surface plasmon resonance phase imaging for ultrasensitive protein and DNA biosensing with oligonucleotide and aptamer microarrays. *Analytical Chemistry,* 2012. **84**(1): p. 440-5.

61. Hansen, J.A., J. Wang, A.-N. Kawde, Y. Xiang, et al. Quantum-Dot/Aptamer-Based Ultrasensitive Multi-Analyte Electrochemical Biosensor. *Journal of the American Chemical Society*, 2006. **128**(7): p. 2228-2229.

62. Weber, P.C., D.H. Ohlendorf, J.J. Wendoloski, and F.R. Salemme. Structural Origins of High-Affinity Biotin Binding to Streptavidin. *Science*, 1989. **243**(4887): p. 85-88.

63. Piran, U. and W.J. Riordan. Dissociation rate constant of the biotin-streptavidin complex. *Journal of Immunological Methods*, 1990. **133**(1): p. 141-143.

64. Lequin, R.M. Enzyme Immunoassay (EIA)/Enzyme-Linked Immunosorbent Assay (ELISA). *Clinical Chemistry*, 2005. **51**(12): p. 2415-2418.

65. Trojanowicz, M. Recent developments in electrochemical flow detections—A review: Part I. Flow analysis and capillary electrophoresis. *Analytica Chimica Acta*, 2009. **653**(1): p. 36-58.

66. Monnig, C.A. and R.T. Kennedy. Capillary Electrophoresis. *Analytical Chemistry*, 1994. **66**(12): p. 280R-314R.

67. Herr, A.E., A.V. Hatch, D.J. Throckmorton, H.M. Tran, et al. Microfluidic Immunoassays as Rapid Saliva-Based Clinical Diagnostics. *Proc. Natl. Acad. Sci.*, 2007. **104**(13): p. 5268-5273.

68. Tamanaha, C.R., S.P. Mulvaney, J.C. Rife, and L.J. Whitman. Magnetic labeling, detection, and system integration. *Biosensors & Bioelectronics*, 2008. **24**(1): p. 1-13.

69. Koh, I., R. Hong, R. Weissleder, and L. Josephson. Sensitive NMR Sensors Detect Antibodies to Influenza. *Angewandte Chemie*, 2008. **120**(22): p. 4187-4189.

70. Koh, I., R. Hong, R. Weissleder, and L. Josephson. Nanoparticle−Target Interactions Parallel Antibody−Protein Interactions. *Analytical Chemistry*, 2009. **81**(9): p. 3618-3622.

71. Pamme, N. Magnetism and microfluidics. *Lab on a Chip*, 2006. **6**(1): p. 24-38.

72. Krishnan, K. Biomedical nanomagnetics: A spin through possibilities in imaging, diagnositcs and therapy. *IEEE Transactions on Magnetics*, 2010. **46**(7): p. 2523-2558.

73. McNaughton, B.H., R.R. Agayan, R. Clarke, R.G. Smith, et al. Single bacterial cell detection with nonlinear rotational frequency shifts of driven magnetic microspheres. *Applied Physics Letters*, 2007. **91**(22): p. 224105.

74. McNaughton, B.H., R.R. Agayan, J.X. Wang, and R. Kopelman. Physiochemical microparticle sensors based on nonlinear magnetic oscillations. *Sensors and Actuators B-Chemical*, 2007. **121**(1): p. 330-340.

75. Connolly, J. and T.G. St Pierre. Proposed biosensors based on time-dependent properties of magnetic fluids. *Journal of Magnetism and Magnetic Materials*, 2001. **225**(1-2): p. 156-160.

76. Fannin, P.C., L. Cohen-Tannoudji, E. Bertrand, A.T. Giannitsis, et al. Investigation of the complex susceptibility of magnetic beads containing maghemite nanoparticles. *Journal of Magnetism and Magnetic Materials*, 2006. **303**(1): p. 147-152.

77. Janssen, X.J.A., A.J. Schellekens, K. van Ommering, L.J. van Ijzendoorn, et al. Controlled torque on superparamagnetic beads for functional biosensors. *Biosensors & Bioelectronics*, 2009. **24**(7): p. 1937-1941.

78. McNaughton, B.H., J.N. Anker, and R. Kopelman. Magnetic microdrill as a modulated fluorescent pH sensor. *Journal of Magnetism and Magnetic Materials*, 2005. **293**(1): p. 696-701.

79. Kinnunen, P., I. Sinn, B.H. McNaughton, and R. Kopelman. High frequency asynchronous magnetic bead rotation for improved biosensors. *Applied Physics Letters*, 2010. **97**(22): p. 223701-223701-3.

80. Kinnunen, P., I. Sinn, B.H. McNaughton, D.W. Newton, et al. Monitoring the growth and drug susceptibility of individual bacteria using asynchronous magnetic bead rotation sensors. *Biosensors and Bioelectronics*, 2011. **26**(5): p. 2751-2755.

81. McNaughton, B.H., R.R. Agayan, V.A. Stoica, R. Clarke, et al. Single Cell Detection with Driven Magnetic Beads. *Functionalized Nanoscale Materials, Devices and Systems*, 2008: p. 403-408.

82. McNaughton, B.H., K.A. Kehbein, J.N. Anker, and R. Kopelman. Sudden breakdown in linear response of a rotationally driven magnetic microparticle and application to physical and chemical microsensing. *Journal of Physical Chemistry B*, 2006. **110**(38): p. 18958-18964.

83. Sinn, I., T. Albertson, P. Kinnunen, D.N. Breslauer, et al. Asynchronous Magnetic Bead Rotation Microviscometer for Rapid, Sensitive, and Label-Free Studies of Bacterial Growth and Drug Sensitivity. *Analytical Chemistry*, 2012. **84**(12): p. 5250-5256.

84. Elbez, R., B.H. McNaughton, L. Patel, K.J. Pienta, et al. Nanoparticle Induced Cell Magneto-Rotation: Monitoring Morphology, Stress and Drug Sensitivity of a Suspended Single Cancer Cell. *Plos One*, 2011. **6**(12): p. e28475.

85. Chung, S.H., A. Hoffmann, K. Guslienko, S.D. Bader, et al. Biological sensing with magnetic nanoparticles using Brownian relaxation (invited). *Journal of Applied Physics*, 2005. **97**(10): p. 10R101.

86. Rauwerdink, A.M. and J.B. Weaver. Measurement of molecular binding using the Brownian motion of magnetic nanoparticle probes. *Applied Physics Letters*, 2010. **96**(3): p. 033702.

87. Biswal, S.L. and A.P. Gast. Rotational dynamics of semiflexible paramagnetic particle chains. *Physical Review E*, 2004. **69**(4): p. 041406.

88. Li, D., J. Rogers, and S.L. Biswal. Probing the Stability of Magnetically Assembled DNA-Linked Colloidal Chains. *Langmuir*, 2009. **25**(16): p. 8944-8950.

89. Petkus, M.M., M. McLauchlin, A.K. Vuppu, L. Rios, et al. Detection of FITC-cortisol via modulated supraparticle lighthouses. *Analytical Chemistry*, 2006. **78**(5): p. 1405-1411.

90. Vuppu, A.K., A.A. Garcia, and M.A. Hayes. Video Microscopy of Dynamically Aggregated Paramagnetic Particle Chains in an Applied Rotating Magnetic Field. *Langmuir*, 2003. **19**(21): p. 8646-8653.

91. Weizmann, Y., F. Patolsky, E. Katz, and I. Willner. Amplified DNA Sensing and Immunosensing by the Rotation of Functional Magnetic Particles. *Journal of the American Chemical Society*, 2003. **125**(12): p. 3452-3454.

Chapter 2

Label-Acquired Magnetorotation for Biosensing: A Magnetic Label Induced Asynchronous Rotation Biosensor

Introduction

Magnetic microbeads have been used in a variety of methods as labels to indicate the presence of a biological molecule. [1-3] The basic structure of these assays involves capturing the target of interest, either an antigen or an antibody, on a surface, and using antibody-labeled magnetic beads or particles to bind to the target. The presence of the magnetic labels can be measured in a variety of ways, including changes in magnetoresistance, [4, 5] relaxation time, [6, 7] translational motion, [8, 9] and particle agglutination. [10-12] In this chapter, we demonstrate label-acquired magnetorotation, in which the target facilitates the binding of magnetic label beads to a nonmagnetic sphere, and the rotational frequency of the resulting sandwich complex in a rotating magnetic field depends on the number of attached magnetic label beads. Label-Acquired Magnetorotation (LAM) is based on the principles of Asynchronous Magnetic Bead Rotation (AMBR), where magnetic particles rotate at a different rate than that of a driving magnetic field. AMBR has previously been used in our lab to measure magnetic properties of magnetic particles, [13] dynamic viscosity, [13] detect bacterial cells with

single cell sensitivity, [14] and for designing a portable sensor. [15] Asynchronous rotation of microparticles has also been studied in a variety of other systems. [16-27]

Superparamagnetic beads, which here are micron-sized beads, each typically composed of an inert polymer sphere embedded with superparamagnetic nanoparticles, have several advantageous properties for use as labels. [2] The magnetic material of the superparamagnetic beads is stable over time, and the beads are stable over long term storage and under most physiological conditions. Biological samples typically have little, if any, naturally occurring magnetic material, thus reducing the likelihood of background interference (with the exception of rare counterexamples, such as magnetotactic bacteria [28]). Superparamagnetic beads are readily manipulated by external magnetic fields, and can be quantitatively detected by a variety of methods.

Sandwich immunoassays are common assay techniques used to detect biological molecules. A sandwich assay includes three components: a solid phase to isolate the analyte from solution; the analyte itself; and a label or indicator, which binds specifically to the analyte. This results in the analyte being "sandwiched" between the solid phase and the label [29]. Some of the more frequently used labels include fluorescent molecules, enzymes, and superparamagnetic beads. [30-32] Here we perform a sandwich assay on the surface of a non-magnetic sphere with superparamagnetic beads as labels.

Micron-scale spheres, particles and magnetic beads, are readily available commercially, in a variety of sizes, coated with biotin or streptavidin, making them an ideal model system for developing new immunoassays. Streptavidin is a tetrameric protein (MW ~ 60 kDa) isolated from the bacteria *Streptomyces avidinii*, and forms a very strong noncovalent bond ($K_d \approx 10^{-15}$ M) with the biomolecule biotin (MW ~ 244).

[33] This protein pair has been used previously to develop spin valve sensors [34] and photonic surface crystal wave [35] assays. In this chapter, the biotin-coated particles serve as a mimic for a biological analyte. In future work, biotin and streptavidin will be replaced by proteins and antibodies of clinical interest.

A schematic of the sensor is shown in Figure 2.1. The setup consists of three components: 6.7 μm streptavidin-coated solid phase spheres, 40 nm biotin-coated particles serving as an analyte mimic, and 1 μm streptavidin-coated superparamagnetic label beads. This figure demonstrates the concept of label-acquired magnetorotation: the sandwich complex rotates only when it has acquired magnetic labels. To the best of our knowledge, this design represents the first combination of label-acquired magnetic rotation with a sandwich assay for the detection of a biological target.

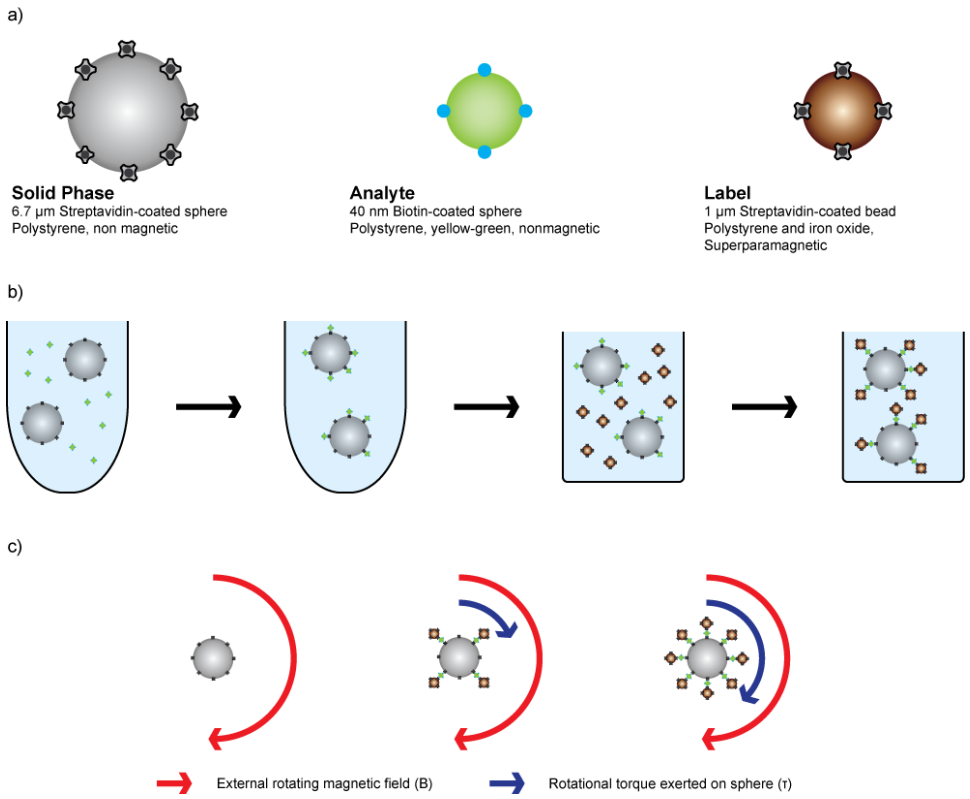

Figure 2.1—Schematic of the design of label-acquired magnetorotation. (a) The three components of the sandwich assay are shown, the solid phase sphere (6.7 µm streptavidin coated sphere), the analyte mimic (40 nm biotin-coated particle) and the label (1 µm streptavidin-coated superparamagnetic bead). Streptavidin is a 60 kDa tetrameric protein, and is represented by the cloverleaf symbol in the schematic, while the actual structure of biotin is shown. (b) Initially, the analyte is incubated with the spheres in a microcentrifuge tube. Following removal of the unbound analyte, the solution is transferred to a square-bottom 384-well plate, where the spheres are incubated with magnetic beads that bind selectively to the analyte, which forms a sandwich complex. (c) In the presence of a rotating magnetic field of constant magnitude, where $\boldsymbol{\tau} = \mathbf{m} \times \mathbf{B}$, the rotational torque exerted on the sphere, and hence its rotational frequency, is a function of the number of attached superparamagnetic label beads.

Materials and Methods

1x Dulbecco's Phosphate-Buffered Saline (PBS) was obtained from MP Biomedicals (Solon, OH). Tween-20 was obtained from Acros Organics (Geel, Belgium). 10% Bovine Serum Albumin (BSA) Blocker solution was obtained from Pierce

(Rockford, IL). 6.7 μm streptavidin-coated polystyrene solid phase spheres (Spherotech, Lake Forest, IL), with density $\rho = 1$ g/cm^3, were washed three times by centrifuging and discarding the supernatant. The spheres were then resuspended and diluted 1:10 in a PBS solution that contained 0.1% Tween-20 and 0.1% BSA (which will be referred to as PBS-TB) to reduce nonspecific adsorption, resulting in a final concentration of 3.02×10^3 spheres/μL. 40 nm yellow-green fluorescent biotin-coated particles (Invitrogen, Carlsbad, CA) were diluted in PBS-TB to final concentrations ranging from 1.62×10^5 particles/μL to 5.12×10^7 particles/μL. 10 μL of the diluted 6.7 μm streptavidin-coated solid phase spheres were mixed with 10 μL of each biotin-coated particle solution and incubated end-over-end on a Sarmix SR1 (Sarstedt, Numbrecht, Germany) rotating mixer for 18 hours. Excess biotin-coated particles were removed by centrifuging the solution and discarding the supernatant three times, and the sample was then resuspended in PBS-TB. (This step was necessary because free biotin-coated particles would cause the streptavidin-coated superparamagnetic label beads to clump.) Successful binding and washing was confirmed by fluorescent microscopy with a 488 nm wavelength light excitation.

1 μm Dynal T1 streptavidin-coated superparamagnetic label beads (Invitrogen), $\rho = 1.8$ g/cm^3, were washed three times, and were then resuspended and diluted 50x in PBS-TB, for a final concentration of 1.94×10^5 beads/μL. 2 μL of the biotin-coated 6.7 μm spheres and 2 μL of the 1 μm streptavidin-coated superparamagnetic label beads were mixed and diluted with 26 μL of PBS-TB, and then transferred to a well on a non-binding surface 384-well plate (Corning, Corning, NY). The components were incubated at room temperature for 4 hours. The 1 μm streptavidin-coated superparamagnetic label beads bound to the exposed biotin-coated particles on the 6.7 μm streptavidin-coated solid

phase spheres, forming a sphere-particle-bead sandwich complex. A coverslip fluidic cell was fashioned between two 22 x 40 mm No. 0 thickness coverslips (Pierce, Rockford, IL) separated by a single piece of double-sided clear tape (3M, St. Paul, MN). The sandwich complexes were transferred from the 384-well plate and pipetted into the coverslip fluidic cell. The ends of the fluidic cell were sealed with Apiezon L grease (Apiezon, Manchester, UK) to prevent drift and evaporation.

A schematic of the experimental setup is shown in Figure 2.2. A rotating magnetic field was created with a pair of orthogonal Helmholtz coils that fits onto an inverted microscope. One pair of coils was driven by a sine wave, and the other pair was driven by a cosine wave, generating a uniform rotating magnetic field between the coils. The driving frequency and amplitude were controlled by an in-house custom-built function generator and amplifier. The field in the center of the coils was 1 mT rotating at a frequency of 20 Hz, as measured by a 3-axis magnetic field transducer (SENIS GmbH, Zurich, Switzerland). The rotation of the spheres was observed using two setups. The first was an Olympus IMT-2 inverted microscope (Olympus, Melville, NY) connected to a Photometrics Cool Snap ES camera (Roper Scientific, Trenton, NJ). Videos were recorded on a computer using MetaMorph (Meta Imaging Software, Downington, PA). The second was an Olympus IX71 inverted microscope with an oil-immersion 100x objective connected to a Basler pIA640-210gm camera (Basler, Highland, IL). Videos were recorded on a computer using an in-house program written in LabVIEW (National Instruments, Austin, TX).Videos were analyzed using the St. Andrews particle tracker (with custom modification to allow for tracking of angular orientation), [36] a sophisticated LabVIEW-based particle tracking program.

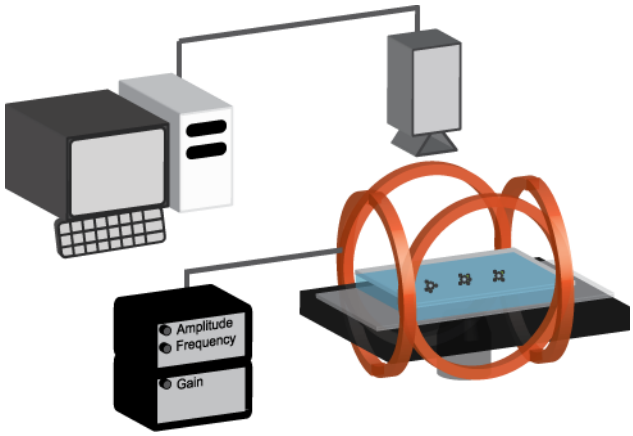

Figure 2.2—Schematic of the setup used in this chapter. Sandwich complexes are pipetted into a coverslip fluidic cell. A rotating magnetic field is created by two orthogonally oriented Helmholtz coils with each coil wrapped with 90 turns of copper wire. The field is controlled by a function generator and an amplifier. Parallel coils are considered part of a "pair." The pairs are driven 90˚ out of phase with each other. The spheres are observed through 60x and 100x objectives connected to a digital camera. Videos are analyzed to determine rotational frequency.

Theory

Overview

For a magnetic object actively rotating in a fluid, the magnetic torque ($\boldsymbol{\tau}_{\text{mag}} = \mathbf{m} \times \mu_0 \mathbf{H}$) and the rotational fluidic drag ($\tau_{\text{drag}} = \gamma \, d\theta/dt$) oppose each other, and are the primary factors determining the rotational dynamics. The magnetic torque is composed of the induced (e.g. paramagnetic and superparamagnetic) and permanent (e.g. ferromagnetic) magnetic moments of the bead. This relationship is expressed below

$$\boldsymbol{\tau}_{\text{drag}} = -\boldsymbol{\tau}_{\text{mag}} \tag{2.1}$$

$$\boldsymbol{\tau}_{\text{mag}} = \boldsymbol{\tau}_{\text{ind}} + \boldsymbol{\tau}_{\text{perm}} \tag{2.2}$$

$$\gamma \frac{d\theta}{dt} = \left| \left(\mathbf{m}_{\text{ind}} + \mathbf{m}_{\text{perm}} \right) \times \mu_0 \mathbf{H} \right| \tag{2.3}$$

where $\mathbf{m}_{\text{ind}}$ is the induced magnetic moment of the bead, $\mathbf{m}_{\text{perm}}$ is the permanent magnetic moment of the bead, μ_0 is the permeability of free space, **H** is the magnetizing field, γ is the drag coefficient, θ is the angular orientation of the object, and $d\theta/dt$ is the rotational rate in radians/s. Note that for this case, other torques, such as inertial and Brownian, are neglected. For a rotating body, $\gamma = \kappa\eta V_H$, where κ is the shape factor (equal to 6 for a sphere), η is the dynamic viscosity, and V_H is the volume of the rotating body. The magnetic torque arising from the induced magnetic moment can be obtained by combining the relationships $\mathbf{m}_{\text{ind}} = \mathbf{M}V_m$ and $\mathbf{M} = \chi\mathbf{H}$, where **M** is the magnetization of the material, χ is the magnetic susceptibility and V_m is the magnetic volume. In a rotating magnetic field, the magnetic susceptibility can be separated into real and imaginary parts $\chi = \chi' - i\chi''$, corresponding to in-phase and out-of-phase components of the magnetization. When the above relationships are substituted into $\boldsymbol{\tau}_{\text{ind}} = \mathbf{m}_{\text{ind}} \times \mu_0\mathbf{H}$ and the cross product is carried out (namely $\left|(\chi'\mathbf{H} - i\chi''\mathbf{H}) \times \mathbf{H}\right| = \chi'' H^2$), one arrives at equation (2.4), which describes the torque arising from induced magnetic moment:

$$\left|\boldsymbol{\tau}_{\text{ind}}\right| = \mu_0 V_m \chi'' H^2 . \tag{2.4}$$

The torque arising from the permanent moment in a rotating magnetic field can be expressed as:

$$\left|\boldsymbol{\tau}_{\text{perm}}\right| = \left|\mathbf{m}_{\text{perm}} \times \mu_0\mathbf{H}\right| = m\mu_0 H \sin\left(\Omega t - \theta\right) \tag{2.5}$$

where t is time and Ω is the rotational frequency of the field. Combining equations (2.1) – (2.5) yields

$$\gamma \frac{d\theta}{dt} = \mu_0 V_m \chi'' H^2 + m\mu_0 H \sin\left(\Omega t - \theta\right) \tag{2.6}$$

Equation (2.6) describes the behavior of the rotating sandwich complex, composed of 1 μm superparamagnetic beads (with a small ferromagnetic component), in a rotating magnetic field.

The magnetic beads used in this study are composed of 1 μm polymer spheres embedded with superparamagnetic nanoparticles. In the presence of a magnetic field, the magnetic moments of these nanoparticles align with the field and then undergo Neel relaxation. If the frequency of a rotating field is sufficiently high, the magnetic behavior is dominated by the imaginary susceptibility, which has been discussed in detail in the literature. [26, 37-40] When dealing with only an induced moment, equation (2.6) reduces to

$$\gamma \frac{d\theta}{dt} = \mu_0 \chi'' H^2 V_m \tag{2.7}$$

When dealing with only permanent magnetic dipoles, equation (2.6) reduces to:

$$\gamma \frac{d\theta}{dt} = m\mu_0 H \sin\left(\Omega t - \theta\right) \tag{2.8}$$

As has been previously shown, [18, 37] this equation can be analytically solved.

Theory for Rotating Sandwich Complex

For the frequency and magnetic field amplitude used in this chapter, 20 Hz and 1 mT, the rotation rate scales with the square of the magnetic field amplitude, as given by $d\theta / dt \propto H^2$ (data not shown). Additionally, the rotation rate increases with increasing driving frequencies, Ω. Both observations indicate that, under these conditions, the induced moment of the beads dominates over their permanent moment and is the primary cause of the driven rotation. As a result, we obtain the following relationship

$$\frac{d\theta}{dt} \propto V_m \tag{2.9}$$

where the changes in the hydrodynamic volume and the shape factor are assumed to be negligible. For a collection of particles with induced dipoles, the total moment is simply the sum of the individual induced moments of each particle. Therefore, equation (2.9) can be rewritten as

$$\frac{d\theta}{dt} \propto N_{particles} \tag{2.10}$$

This dependence can be seen in Figure 2.5b, and equation (2.8) holds for materials that do not have permanent dipoles. Equation (2.10) establishes that the rotational frequency in Hz (e.g. $(1/2\pi)*(d\theta/dt)$) of a sandwich complex in a rotating magnetic field is a function of the number of 1 μm superparamagnetic beads in the rotating sandwich complex. Since the beads attach proportionally to the concentration of the analyte, we can rewrite equation (2.10) as

$$\frac{d\theta}{dt} \propto [analyte] \tag{2.11}$$

Indeed, this general behavior of increased rotational rate with increased analyte coverage is observed over two orders of magnitude as shown in Figure 2.6 and is discussed in detail below.

Results and Discussion

Sandwich complex assays were performed with biotin-coated particles as the analyte, which mimic a biological target. The concentration of biotin-coated particles was measured by observing the rate of rotation of the (solid phase sphere)-(biotin-coated

particle)-(superparamagnetic label bead) sandwich complex. The 6.7 μm solid phase sphere has a surface area of 141 μm^2. Given that a 40 nm biotin-coated particle would occupy an area of 1.26 x 10^{-3} μm^2, one 6.7 μm sphere could bind up to 10^5 biotin-coated particles. The superparamagnetic label beads have a diameter of 1 μm, and occupy an area of 0.866 μm^2, which, given the limits of the packing efficiency of spheres, suggest that 145 superparamagnetic label beads can bind to that surface. This configuration would be expected to produce a sensor with approximately 2 orders of magnitude of dynamic range, as indicated by equation 2.5, assuming that the magnetic moments of the beads are additive. The position at which the beads bind to the sphere should mostly affect the rotation at low numbers of binding beads. A variation in the binding location of a few beads could affect the rotational speed, which would result from differences in location-dependent torque and drag. However, as the number of beads on the sphere increases, this effect will have a smaller contribution. A full theoretical investigation into the specifics of this effect warrants further study, potentially using Hydro++, [38] but is beyond the scope of this chapter. Furthermore, the 6.7 μm "mother" sphere is more than 300 times bigger than a 1 μm label bead, thus the binding of a single bead to the sphere should not significantly alter the sphere's center of rotation or shape factor. Size 1 μm beads were selected as labels for these experiments so that they could still be individually distinguished by using optical microscopy.

Scanning electron micrographs of the sandwich complexes are shown in Figure 2.3. The three complexes shown were from samples with total biotin-coated particle concentrations of 2.88x 10^7 particles/μL, 2.88x 10^6 particles/μL, and 2.88x 10^5 particles/μL, respectively. Figure 2.3a shows a reasonably dense coverage of the sphere

by the superparamagnetic label beads, while Figure 2.3b shows fewer beads, and figure 2.3c show only two beads. This trend confirms that a greater number of superparamagnetic label beads are present with increasing amounts of biotin-coated particle.

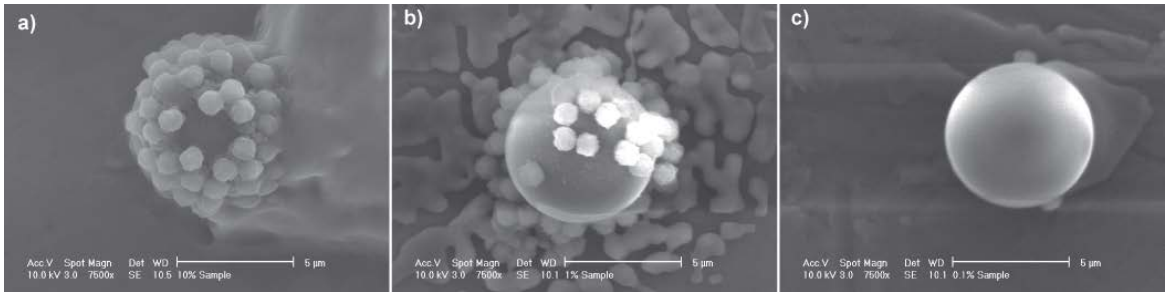

Figure 2.3—Scanning electron micrographs of sandwich complexes incubated with three different concentrations of biotin-coated particles, (a) 2.88 x 10^7 μL^{-1}, (b) 2.88 x 10^6 μL^{-1}, and (c) 2.88 x 10^5 μL^{-1}. 1 μm superparamagnetic label beads can be seen attached to the surface of the 6.7 μm solid phase spheres. The structures in the background of these images likely resulted from salts left by the buffer after evaporation.

The frame-by-frame analysis of sandwich complexes, from four 15 seconds videos recorded at 20 frames per seconds, is shown in Figure 2.4a. The angle of the sandwich complex in each frame is calculated against the first frame in the video, which is defined as the zero angle. One complete rotation is 360 degrees. The sandwich complexes occasionally were out of focus, which caused the tracker to mistrack the complexes for those frames. These outlying points were removed from Figure 2.4a, based on calculating the jackknife residuals for each point and discarding outliers whose residuals exceeded the Bonferroni criteria. [39] The MATLAB code for performing this procedure is included in Appendix C-1.The four videos represent sandwich complexes with rotational frequencies of 133 mHz, 231 mHz, 303 mHz, and 396 mHz. The traces

demonstrate the stability and consistency of the rotation of a sandwich complex during a 15 second observational period. 10 frames from each of the four videos, 0.5 seconds apart, are shown in Figure 2.4b. These images show the sandwich complexes rotating clockwise.

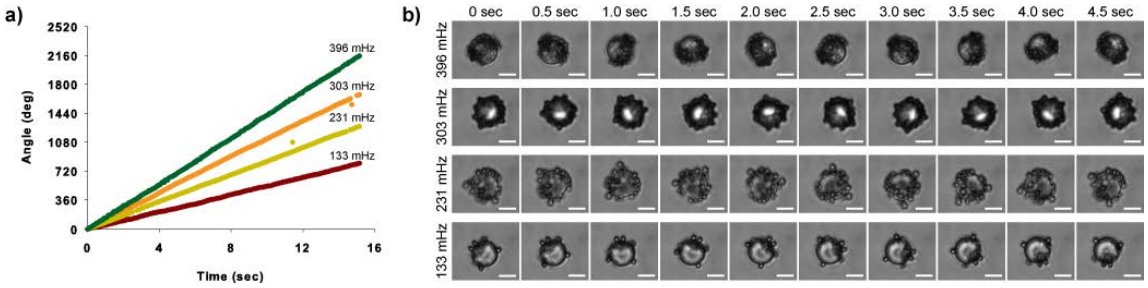

Figure 2.4—Examination of the behavior of individual sandwich complexes. (a) Frame-by-frame analysis of four different rotating sandwich complexes. The angle at each time point represents the number of degrees through which the complex has rotated since t_0 (360˚ represents one full rotation). The rotational frequency of the complex is shown above each trace. (b) Ten frames from each of the videos in part (a), in 0.5 second intervals. The top sandwich complex completes about 1.75 rotations over the 10 frames, while the bottom sandwich complex completes about 0.75 rotations over the 10 frames. The driving frequency is 20 Hz for all samples. Scale bar is 5 μm.

The stability of the rotational frequency of sandwich complexes was also measured. Sandwich complexes were observed for 60 minutes, with 15 second videos of the rotating complex captured every five minutes. Eight sandwich complexes were observed in total; four adhered to the coverslip before the end of the 60 minutes, and were excluded from the analysis. The use of PBS-TB decreased nonspecific adherence to the coverslips, but did not completely prevent it. The average (±SD) rotational frequencies of the four complexes determined from the videos over the observational period are: 124.1 ± 6.2 mHz, 203.3 ± 5.1 mHz, 302.1 ± 4.2 mHz, and 410.8 ± 6.3 mHz.

The rotational frequencies of the four sandwich complexes are shown in Figure 2.5a, and demonstrate that the rotational frequency of a rotating complex is stable over at least 60 minutes.

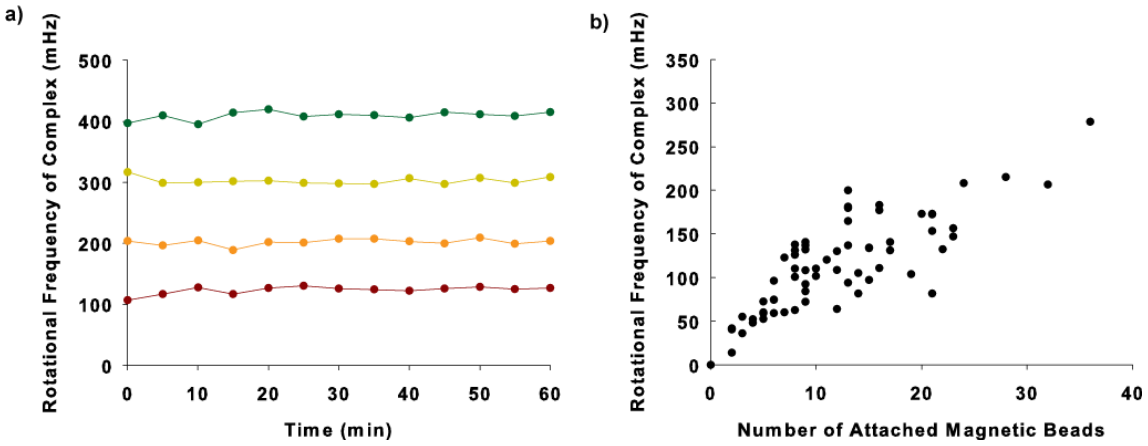

Figure 2.5—(a) The stability of the rotation of a sandwich complex over time. The rotational frequency of the complex was obtained every five minutes over a sixty minute observational period. The mean ± standard deviation of the rotational frequency for the four complexes over the observational period is 124.1 ± 6.2 mHz, 203.3 ± 5.1 mHz, 302.1 ± 4.2 mHz, and 410.8 ± 6.3 mHz. (b) Relationship between the rotational frequency of the sandwich complex and the number of attached superparamagnetic beads. A linear trendline fits the data ($r^2 = 0.649$). Note that a sandwich complex will rotate with as little as two attached beads.

The behavior of individual sandwich complexes was found to determine the relationship between the rotational frequency and the number of attached superparamagnetic label beads. The number of superparamagnetic label beads attached to the complex was determined by visual inspection. The rotating magnetic field was then turned on, and the rotational frequency of each complex was measured. These results are shown in Figure 2.5b. (During observations, it was difficult to distinguish individual beads when more than 40 were on a solid phase sphere, so complexes with more than 40 attached beads were excluded from this analysis.) It should also be noted that a complex

will rotate with as little as two attached superparamagnetic label beads, which suggests that the theoretical lower detection limit of the system could be on the order of a few analyte molecules bound to the surface, for this solid phase sphere and magnetic label bead combination.

Having established the stability of the rotation of a sandwich complex, and the relationship between rotational frequency and the number of attached superparamagnetic label beads, label-acquired magnetorotation (LAM) was then shown to be capable of measuring the concentration of biotin-coated particles in solution. Sandwich complexes with a range of biotin-coated particle concentrations were prepared as described in the experimental section, transferred into a coverslip fluidic cell, and placed in a rotating magnetic field. Eight sandwich complexes from each concentration of biotin-coated particles were chosen at random and 15 second videos of each sandwich complex were recorded. Complexes that adhered to the surface of the coverslip were not considered for analysis (the number of attached magnetic labels did not appear to be a factor in determining sandwich complex-surface adhesion). The results are shown in Figure 2.6. The rotational frequency of the sandwich complex increases with increasing biotin-coated particle concentration over the range from 1.62×10^5 to 9.70×10^6 biotin-coated particles/μL, and then plateaus at higher concentrations. This plateau is likely due to the saturation of the sphere by superparamagnetic beads labels. The lowest detected concentration of biotin-coated particles was 2.88×10^5 particles/μL. No formation of sandwich complexes, or rotation of the 6.7 μm spheres, was observed in control samples with no biotin-coated particles.

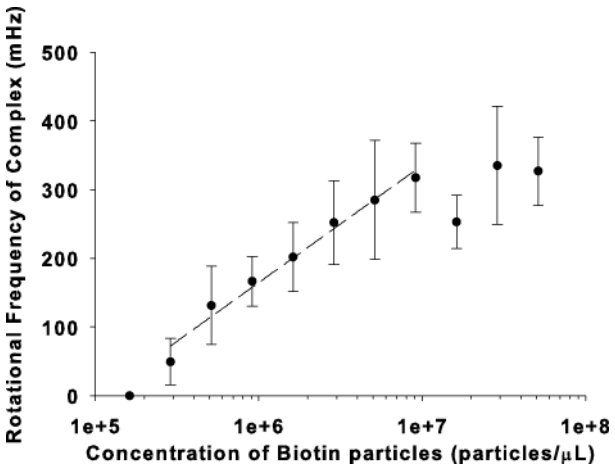

Figure 2.6—A log-linear plot of the relationship between rotational frequency of the complex and concentration of analyte incubated with the sphere. Each point represents an average of eight measurements (±SD). At high concentrations of biotin-coated particles, the sensor saturates and the rotational frequency plateaus. The sensor is linear over its dynamic range, indicated by the dashed line, $r^2 = 0.982$.

The results demonstrate that label-acquired magnetorotation can be used to detect the presence of biological targets. One of the challenges facing this system is the significant size distribution of the beads and spheres, which accounts for the wide distributions and large standard deviations in our data (Figures 2.5b and 2.6). When comparing one sandwich complex to another, the uniformity of the solid phase is important. The 6.7 μm solid phase spheres had a coefficient of variability in the diameter of 5.8 % as determined by fluorescent activated cell sorting. [40] Since the rotational frequency of the sphere depends on volume, this results in up to a 17.4 % variability in rotational frequency. Additionally, the superparamagnetic label beads, composed of magnetic nanoparticles embedded in a 1 μm non-magnetic bead, exhibit significant bead-to-bead variability. 2.8 μm superparamagnetic beads from the same manufacturer have been reported to have a variability in magnetic responsiveness (a combination of bead magnetic moment and shape factor) on the order of 30%, [41, 42] and observations in our

lab suggest a similar variability for the 1 μm beads. These high variabilities could be reflected by the data presented in Figure 2.5. Despite the variabilities, averaging through multiple samples allows for validation of this new method.

The potential sensitivity of this method was indicated by the rotation of a sandwich complex which was observed after the attachment of just two superparamagnetic label beads. The system described here presents a number of potential advantages for diagnostic applications, and we are exploring a number of avenues that could turn this new method into a clinically useful technology. We envision that label-acquired asynchronous magnetic bead rotation will be used in future diagnostic devices. Such a system could be applied to detect a wide range of biological targets, including proteins, viruses, bacteria and cancer cells, or any other target associateable with an affinity molecule. Currently, work is underway on label-acquired magnetorotation for the detection of antigens with antibodies, using a photodiode and a laser for monitoring rotation. [15] Additionally, work is underway to transfer this system onto a microfluidic chip.

Conclusion

This chapter presents a proof-of-principle for a new kind of biosensor, based on label-acquired asynchronous magnetic bead rotation. The sensor is based on a sandwich assay, with a nonmagnetic sphere as the solid phase and superparamagnetic beads as the analyte labels and utilizes asynchronous magnetic bead rotation (AMBR). The rotational frequency of the sandwich complex in a rotating magnetic field depends on the concentration of the analyte present in the solution. This sensor demonstrates the

potential for a simple and sensitive technique, with two orders of magnitude in dynamic range, which we hope would improve upon parameter optimization. Although further work remains to be done, this system exhibits potential for integration with other developing diagnostic devices for proteins and other biological macromolecules.

Acknowledgments

We thank Alex Hrin for creating the video capture LabVIEW program, Ron Smith for assistance with microscopy, and Haiping Sun, Kai Sun and the University of Michigan Electron Microbeam Analysis Laboratory (EMAL) for assistance with collecting the Scanning Electron Micrographs.

This research was partially supported by the Department of Homeland Security (DHS) Scholarship and Fellowship Program, administered by the Oak Ridge Institute for Science and Education (ORISE) through an interagency agreement between the U.S. Department of Energy (DOE) and DHS. ORISE is managed by Oak Ridge Associated Universities (ORAU) under DOE contract number DE-AC05-06OR23100. All opinions expressed in this chapter are the author's and do not necessarily reflect the policies and views of DHS, DOE, or ORAU/ORISE. BHM acknowledges supported by NIH grant UL1RR024986 (Postdoctoral Translational Scholar Program). Additional support was provided by grant NSF/DMR 0455330 (RK) and NIH R21 EB009550 (RK).

References

1. Gijs, M. Magnetic bead handling on-chip: new opportunities for analytical applications. *Microfluidics and Nanofluidics*, 2004. **1**(1): p. 22-40.
2. Gijs, M.A.M., F. Lacharme, and U. Lehmann. Microfluidic Applications of Magnetic Particles for Biological Analysis and Catalysis. *Chemical Reviews*, 2010. **110**(3): p. 1518-1563.
3. Pamme, N. Magnetism and microfluidics. *Lab on a Chip*, 2006. **6**(1): p. 24-38.
4. Edelstein, R.L., C.R. Tamanaha, P.E. Sheehan, M.M. Miller, et al. The BARC biosensor applied to the detection of biological warfare agents. *Biosensors & Bioelectronics*, 2000. **14**(10-11): p. 805-813.
5. Baselt, D.R., G.U. Lee, M. Natesan, S.W. Metzger, et al. A biosensor based on magnetoresistance technology. *Biosensors & Bioelectronics*, 1998. **13**(7-8): p. 731-9.
6. Lee, H., E. Sun, D. Ham, and R. Weissleder. Chip-NMR biosensor for detection and molecular analysis of cells. *Nature Medicine*, 2006. **14**(8): p. 869-874.
7. Chung, S.H., A. Hoffmann, S.D. Bader, C. Liu, et al. Biological sensors based on Brownian relaxation of magnetic nanoparticles. *Applied Physics Letters*, 2004. **85**(14): p. 2971-2973.
8. Hahn, Y.K., Z. Jin, J.H. Kang, E. Oh, et al. Magnetophoretic immunoassay of allergen-specific IgE in an enhanced magnetic field gradient. *Analytical Chemistry*, 2007. **79**(6): p. 2214-2220.
9. Kim, K.S. and J.K. Park. Magnetic force-based multiplexed immunoassay using superparamagnetic nanoparticles in microfluidic channel. *Lab on a Chip*, 2005. **5**(6): p. 657-664.
10. Baudry, J., E. Bertrand, N. Lequeux, and J. Bibette. Bio-specific recognition and applications: from molecular to colloidal scales. *Journal of Physics-Condensed Matter*, 2004. **16**(15): p. R469-R480.
11. Baudry, J., C. Rouzeau, C. Goubault, C. Robic, et al. Acceleration of the recognition rate between grafted ligands and receptors with magnetic forces. *Proceedings of the National Academy of Sciences of the United States of America*, 2006. **103**(44): p. 16076-16078.
12. Petkus, M.M., M. McLauchlin, A.K. Vuppu, L. Rios, et al. Detection of FITC-cortisol via modulated supraparticle lighthouses. *Analytical Chemistry*, 2006. **78**(5): p. 1405-1411.
13. McNaughton, B.H., R.R. Agayan, J.X. Wang, and R. Kopelman. Physiochemical microparticle sensors based on nonlinear magnetic oscillations. *Sensors and Actuators B-Chemical*, 2007. **121**(1): p. 330-340.

14. McNaughton, B.H., R.R. Agayan, R. Clarke, R.G. Smith, et al. Single bacterial cell detection with nonlinear rotational frequency shifts of driven magnetic microspheres. *Applied Physics Letters*, 2007. **91**(22): p. 224105.

15. McNaughton, B.H., P. Kinnunen, R.G. Smith, S.N. Pei, et al. Compact sensor for measuring nonlinear rotational dynamics of driven magnetic microspheres with biomedical applications. *Journal of Magnetism and Magnetic Materials*, 2009. **321**(10): p. 1648-1652.

16. McNaughton, B.H., R.R. Agayan, V.A. Stoica, R. Clarke, et al. Single Cell Detection with Driven Magnetic Beads. *Functionalized Nanoscale Materials, Devices and Systems*, 2008: p. 403-408.

17. McNaughton, B.H., J.N. Anker, and R. Kopelman. Magnetic microdrill as a modulated fluorescent pH sensor. *Journal of Magnetism and Magnetic Materials*, 2005. **293**(1): p. 696-701.

18. McNaughton, B.H., K.A. Kehbein, J.N. Anker, and R. Kopelman. Sudden breakdown in linear response of a rotationally driven magnetic microparticle and application to physical and chemical microsensing. *Journal of Physical Chemistry B*, 2006. **110**(38): p. 18958-18964.

19. Helgesen, G., P. Pieranski, and A.T. Skjeltorp. Nonlinear phenomena in systems of magnetic holes. *Physical Review Letters*, 1990. **64**(12): p. 1425-1428.

20. Biswal, S.L. and A.P. Gast. Micromixing with linked chains of paramagnetic particles. *Analytical Chemistry*, 2004. **76**(21): p. 6448-55.

21. Shelton, W.A., K.D. Bonin, and T.G. Walker. Nonlinear motion of optically torqued nanorods. *Phys Rev E Stat Nonlin Soft Matter Phys*, 2005. **71**(3 Pt 2A): p. 036204.

22. Yellen, B.B., R.M. Erb, H.S. Son, R. Hewlin, Jr., et al. Traveling wave magnetophoresis for high resolution chip based separations. *Lab on a Chip*, 2007. **7**(12): p. 1681-8.

23. Cebers, A. and M. Ozols. Dynamics of an active magnetic particle in a rotating magnetic field. *Physical Review E*, 2006. **73**: p. 021505.

24. Anker, J.N., C. Behrend, and R. Kopelman. Aspherical magnetically modulated optical nanoprobes (MagMOONs). *Journal of Applied Physics*, 2003. **93**(10): p. 6698-6700.

25. Anker, J.N. and R. Kopelman. Magnetically modulated optical nanoprobes. *Applied Physics Letters*, 2003. **82**(7): p. 1102-1104.

26. Janssen, X.J.A., A.J. Schellekens, K. van Ommering, L.J. van Ijzendoorn, et al. Controlled torque on superparamagnetic beads for functional biosensors. *Biosensors & Bioelectronics*, 2009. **24**(7): p. 1937-1941.

27. Bacri, J.C., A.O. Cebers, and R. Perzynski. Behavior of a magnetic fluid microdrop in a rotating magnetic field. *Physical Review Letters*, 1994. **72**(17): p. 2705.

28. Erglis, K., Q. Wen, V. Ose, A. Zeltins, et al. Dynamics of magnetotactic bacteria in a rotating magnetic field. *Biophysical Journal*, 2007. **93**(4): p. 1402-1412.

29. Wild, D., The Immunoassay handbook. 2nd ed. 2001, London: Nature Pub. Group. xxix, 906 p.

30. Baselt, D.R., G.U. Lee, and R.J. Colton. Biosensor based on force microscope technology. *Journal of Vacuum Science & Technology B*, 1996. **14**(2): p. 789-793.

31. MacBeath, G. Protein microarrays and proteomics. *Nature Genetics*, 2002. **32**: p. 526-532.

32. Park, S. and R.A. Durst. Immunoliposome sandwich assay for the detection of Escherichia coli O157 : H7. *Analytical Biochemistry*, 2000. **280**(1): p. 151-158.

33. Weber, P.C., D.H. Ohlendorf, J.J. Wendoloski, and F.R. Salemme. Structural Origins of High-Affinity Biotin Binding to Streptavidin. *Science*, 1989. **243**(4887): p. 85-88.

34. Ferreira, H.A., D.L. Graham, P.P. Freitas, and J.M.S. Cabral. Biodetection using magnetically labeled biomolecules and arrays of spin valve sensors (invited). *Journal of Applied Physics*, 2003. **93**(10): p. 7281-7286.

35. Konopsky, V.N. and E.V. Alieva. A biosensor based on photonic crystal surface waves with an independent registration of the liquid refractive index. *Biosensors & Bioelectronics*, 2010. **25**(5): p. 1212-1216.

36. Milne, G., *Optical Sorting and Manipulation of Microscopic Particles*. 2007, University of St. Andrews.

37. Connolly, J. and T.G. St Pierre. Proposed biosensors based on time-dependent properties of magnetic fluids. *Journal of Magnetism and Magnetic Materials*, 2001. **225**(1-2): p. 156-160.

38. Fannin, P.C., L. Cohen-Tannoudji, E. Bertrand, A.T. Giannitsis, et al. Investigation of the complex susceptibility of magnetic beads containing maghemite nanoparticles. *Journal of Magnetism and Magnetic Materials*, 2006. **303**(1): p. 147-152.

39. Astalan, A.P., F. Ahrentorp, C. Johansson, K. Larsson, et al. Biomolecular reactions studied using changes in Brownian rotation dynamics of magnetic particles. *Biosensors & Bioelectronics*, 2004. **19**(8): p. 945-951.

40. Krishnan, K. Biomedical nanomagnetics: A spin through possibilities in imaging, diagnositcs and therapy. *IEEE Transactions on Magnetics*, 2010. **46**(7): p. 2523-2558.

41. Cebers, A. and M. Ozols. Dynamics of an active magnetic particle in a rotating magnetic field. *Physical Review E*, 2006. **73**(2): p. -.

42. Garcia de la Torre, J., S. Navarro, M.C. Lopez Martinez, F.G. Diaz, et al. HYDRO: a computer program for the prediction of hydrodynamic properties of macromolecules. *Biophysical Journal*, 1994. **67**(2): p. 530-531.

43. Faraway, J.J., Linear models with R. Texts in statistical science v. 63. 2005, Boca Raton: Chapman & Hall/CRC. x, 229 p.

44. Kildrew-Shah, B., *Personal E-mail communication on the variability of spherotech SVP-60-5 lot AA01*. 2009.

45. Hafeli, U.O., M.A. Lobedann, J. Steingroewer, L.R. Moore, et al. Optical method for measurement of magnetophoretic mobility of individual magnetic microspheres in defined magnetic field. *Journal of Magnetism and Magnetic Materials*, 2005. **293**(1): p. 224-239.

46. Hafeli, U., R. Ciocan, and J.P. Dailey. Characterization of magnetic particles and microspheres and their magnetophoretic mobility using a digital microscopy method. *European Cells and Materials*, 2002. **3**(Suppl. 2): p. 24-27.

Chapter 3

Label-Acquired Magnetorotation as a signal transduction method for protein detection: aptamer-based detection of thrombin

Introduction

One of the primary goals in a point-of-care diagnostic system is measuring the concentration of a protein in order to assess the overall health of a patient. Effective screening methods have been shown to improve patient health, such as a recent large study, on a population at high risk for lung cancer, which found a 20% decrease in mortality due to better early screening. [1, 2] There are three primary components in a protein measurement system: the target biomarker to be measured, the affinity molecules used to capture the target, and the method of transducing a successful binding event into a quantifiable signal. There are several popular signal transduction methods, including optical, electrochemical and magnetic schemes. This chapter presents the continued development of the optomagnetic signal transduction method, called Label-Acquired Magnetorotation (LAM), which has the potential for eventual incorporation into a point-of-care diagnostic system. Previously, we published proof-of-principle work demonstrating the concept of LAM using a biotin and streptavidin system as protein and aptamer mimics. [3] Here, we demonstrate the next step by showing LAM used to detect proteins in solution using aptamers.

The most common set-up for measuring the concentration of a protein in solution is the sandwich assay, where the target is first captured by an affinity molecule bound to a surface, and is then sandwiched by a signal transducer attached to another affinity molecule. [4] Optical methods include sandwich-based ELISA, [5-7] fluorescence signaling [8-10] or quantum dots, [11, 12] and the non-sandwich based surface plasmon resonance methods. [13-15] The electrochemical methods include sandwich-based amperometric enzymatic methods [16, 17] and non-sandwich-based impedimetric sensing. [18, 19]

Magnetic beads are advantageous for use as signal transducers because they are biologically inert, are physically stable under most biological environments, and biological materials have no native magnetism that could interfere with a signal from the beads. [20, 21] Due to these advantages, magnetic beads have been used as signal transducers in a variety of applications, including giant magnetoresistance (GMR), [22-24] Hall probes, [25, 26] and magnetic relaxation. [27, 28] Additionally, magnetic beads have been used as carriers for magnetophoresis and to facilitate detection by other signal transduction methods. [29-31] In contrast, the method described here uses optical detection of the magnetic behavior.

The beads used in this study are 1 μm commercial beads that exhibit superparamagnetic behavior (DynaBeads®). These beads are composed of maghemite (γ-Fe_2O_3) nanoparticles, with a mean diameter of 8 nm dispersed within a polymer bead. The beads are 25.5% Fe by mass. [32] In the absence of a magnetic field, these beads have no net magnetization, but within a magnetic field, the magnetic moments of the beads align with the field and they become strongly magnetic. [32]

The work presented here uses these beads in a rotating magnetic field. Previous studies have examined and characterized the behavior of these beads in alternating magnetic fields. It was first shown that in a one-dimensional alternating magnetic field, the dominant relaxation mechanism of such superparamagnetic beads is the Neel relaxation of the nanoparticles embedded within the bead. [33] It was later shown that in a two-dimensional rotating magnetic field, at high driving frequencies, the dominant mechanism driving the rotation of these same beads is also related to Neel relaxation. [34] Brownian rotational effects are not significant for these beads because the time constant for the Brownian relaxation of a sphere with diameter on the order of a micron is on the order of seconds, while the time constant for the Neel relaxation of the inner magnetic nanoparticles is on the order of nanoseconds.

In a two-dimensional rotating magnetic field, at low driving frequencies, magnetic beads are able to rotate synchronously with the field. At higher driving frequencies (above the critical frequency [35]) these beads are not able to stay in phase with the field, and rotate asynchronously. In the asynchronous regime, the rotational frequency of the bead depends on a number of factors, including the magnetic moment of the bead, the amplitude and frequency of the driving field, the hydrodynamic volume of the bead, and the viscosity of the solution. This asynchronous rotation has already been demonstrated to be a useful tool for making biological measurements, specifically for monitoring the growth and antibiotic susceptibility of bacteria. [36-39]

Thrombin is a coagulation factor that is the first step in the coagulation cascade that leads to the formation of a blood clot, so as to stem blood loss. Aptamers are single- or double-stranded nucleic acid sequences that bind to proteins through favorable

electrostatic interactions, with an affinity similar to that of an antibody. [40, 41] One of the earliest aptamers to be identified binds to the fibrin exosite on thrombin, and has the following 15-base pair sequence: 5'-GGTTGGTGTGGTTGG-3'. [42] Later, a second, 29-base pair sequence against thrombin was identified, which binds to the heparin exosite: 5'-GTCCGTGGTAGGGCAGGTTGGGGTGAC-3'. [43] Since these aptamers bind to opposite sides of the thrombin molecule, they represent an ideal system for the development of an aptamer-based sandwich assay, and have been used in the development of many such assays. [44-46]

Materials and Methods

A schematic of LAM is shown in Figure 3.1. The mother spheres used were 10 μm nonmagnetic streptavidin-coated ProActive microspheres (Bangs Labs, Fishers, IN). The daughter beads used were Dynal MyOne 1 μm streptavidin-coated DynaBeads that exhibit superparamagnetic behavior (Invitrogen, Carlsbad, CA). Human α-thrombin was purchased from Haematologic Technologies (Essex Junction, VT). Biotinylated aptamers (with a 5' polyT_{20} tail for improved binding)[47] were purchased from Integrated DNA Technologies (Coralville, IA). Salts (NaCl, KCl, $MgCl_2$, EDTA and Tris-HCl) and Tween-20 were purchased from Sigma Aldrich (St. Louis, MO). Bovine serum albumin (BSA) Blocker solution was purchased from Thermo Scientific (Waltham, MA). Zero-thickness glass coverslips were obtained from Electron Microscopy Sciences (Hatfield, PA). OPI Top Coat clear nail protector was purchased from OPI Products Inc. (North Hollywood, CA). Formulations for wash buffer, aptamer binding buffer, and thrombin

binding buffer (containing 0.1% BSA, and with the addition of 10 mM KCl [48]) were based on previously published work. [47]

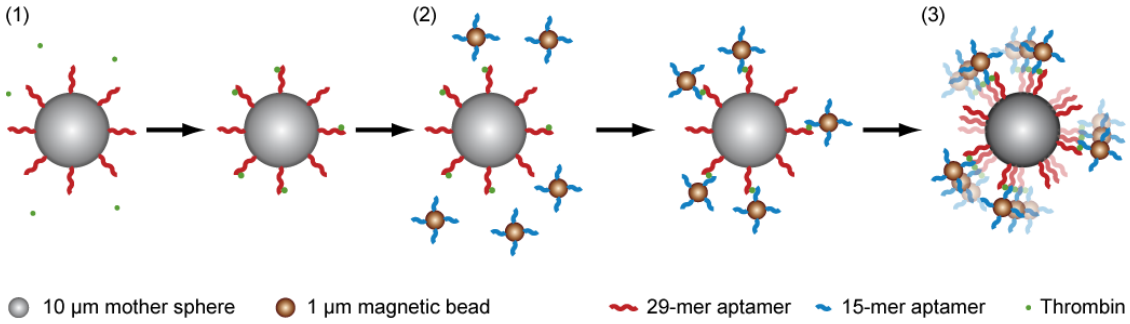

Figure 3.1—Schematic of LAM with thrombin as the analyte. (1) 10 µm nonmagnetic mother spheres coated with the 29-mer anti-thrombin aptamer are mixed with thrombin, which binds to the mother spheres. (2) 1 µm magnetic beads coated with the 15-mer anti-thrombin aptamer are mixed with the thrombin-coated mother spheres. The magnetic beads bind to the thrombin attached to the mother sphere, forming a sandwich complex. (3) The sandwich complex is transferred to a rotating magnetic field, where the rotational frequency of the sandwich complex depends on the number of attached magnetic beads.

An aliquot of 50 µL of the magnetic beads was washed three times by magnetic separation in 200 µL of wash buffer, and then resuspended in 500 µL of aptamer binding buffer, at a concentration of 1 mg/mL beads in a microcentrifuge tube. An aliquot of 50 µL of the mother spheres was washed three times by centrifugation in 200 µL of wash buffer, and then resuspended in 1 mL of aptamer binding buffer, at a concentration of 0.5 mg/mL spheres. A 10 µL aliquot of biotinylated-15-mer thrombin binding aptamer was added to the superparamagnetic beads, and a 10 µL aliquot of biotinylated-29-mer thrombin binding aptamer was added to the mother spheres. The two solutions were briefly vortexed then incubated on an end-over-end rotator for 1 hour. They were then washed (by magnetic separation and centrifugation, respectively) three times and

resuspended in thrombin binding buffer. An aliquot of human α-thrombin was serially diluted over a concentration range of 50 nM to 100 pM in thrombin binding buffer. In a separate tube, 100 μL of thrombin solution were mixed with 40 μL of mother sphere solution, and then incubated on an end-over-end rotator for 90 minutes. Finally, 10 μL of magnetic bead solution were added to the mother spheres and thrombin and incubated on an end-over-end rotator for 90 minutes.

Microfluidic flow cells were prepared from two zero-thickness glass coverslips (the bottom coverslip was coated with a thin layer of clear nail protector, to reduce particle sticking) separated by a single piece of double-sided Scotch tape (3M, St. Paul, MN). The solution containing the mother spheres and the magnetic beads was diluted with 140 μL of 0.2% Tween-20, and 20 μL of this solution were pipetted into the coverslip flow cell. The coverslip flow cell was then placed in a rotating magnetic field (amplitude 1.25 mT, frequency 200 Hz) built from two pairs of orthogonally-oriented Helmholtz coils driven by a pair of sinusoidal waves 90 degrees out of phase with each other. The magnetic field was located on top of an IX71 inverted microscope (Olympus, Melville, NY). The rotation of the sandwich complexes was observed through a 100x oil-immersion objective, imaged through a Basler piA640-210gm camera (Basler, Highland, IL) and recorded by an in-house program written in LabVIEW (National Instruments, Austin, TX). Videos were analyzed using the St. Andrews particle tracker [49] and an in-house program written in MATLAB, which is included in Appendix C-1.

Theory

The theory governing the behavior of superparamagnetic particles and beads in rotating magnetic fields has been discussed in detail elsewhere. [3, 33, 34, 50] Briefly, starting from the equation for the magnetic torque, $\boldsymbol{\tau} = \mathbf{m} \times \mathbf{B}$, where **m** is the magnetic moment of the bead and **B** is the external magnetic field, assuming steady-state rotation (allowing for the equating of rotational driving forces with drag forces, $\tau = \kappa \eta V_H \frac{d\theta}{dt}$, where κ is the shape factor (equal to 6 for a sphere), η is the viscosity of the surrounding fluid, and V_H is the hydrodynamic volume), and making some simple substitutions, $\mathbf{B} = \mu_0 \mathbf{H}$, $\mathbf{m} = \mathbf{M} V_m$, $\mathbf{M} = \chi \mathbf{H}$ and $\chi = \chi' - i\chi''$, (where **H** is the magnetizing field, μ_0 is the permeability of free space, **M** is the volume magnetization, V_m is the volume of the bead's magnetic material, χ is the bead susceptibility, χ' is the real component of the bead susceptibility and χ'' is the imaginary component of the bead susceptibility) we can get an expression for the rotational frequency dθ/dt:

$$\frac{d\theta}{dt} = \frac{1}{\kappa \eta V_H} \mu_0 V_m \chi'' H^2 \tag{3.1}$$

The definition of imaginary susceptibility, χ'', is $\chi'' = \chi_0 \frac{\Omega \tau_N}{1 + \Omega^2 \tau_N^2}$, where χ_0 is the DC susceptibility, Ω is the frequency of the driving field. The definition of Neel relaxation time, τ_N, is $\tau_N = \tau_0 \exp\left(\frac{KV_p}{k_B T}\right)$, where τ_0 is the attempt frequency, K is the anisotropy constant (equal to 5 x 10^4 J/m^3 for maghemite nanoparticles [51]), V_p is the volume of the maghemite nanoparticles, k_B is Boltzmann's constant, and T is the ambient temperature. The magnetic nanoparticles are not perfectly uniform; for a size distribution with n intervals, with average nanoparticle volume V_p, the total volume of nanoparticles in the

distribution is $V_{n.}$ The expression for Neel relaxation time, τ_N, can be substituted into the expression for imaginary susceptibility, χ'', which, along with considering the effects of the nanoparticle size distribution, can then be substituted into equation (3.1) to create a single expression describing the rotation of a superparamagnetic object in a magnetic field: [34]

$$\frac{d\theta}{dt} = \frac{1}{\kappa\eta V_H}\mu_0 V_m H^2 \chi_0 \frac{1}{\sum_n V_n^2}\sum_n \frac{\Omega\tau_0 \exp\left(\frac{KV_p}{k_B T}\right)}{1+\Omega^2 \exp\left(\frac{2KV_p}{k_B T}\right)} V_n^2 \tag{3.2}$$

In the low driving frequency ($\Omega << 1$ kHz) regime used in this chapter, $\Omega^2 \exp\left(\frac{2KV_p}{k_B T}\right) << 1$, so equation (3.2) can be simplified:

$$\frac{d\theta}{dt} = \frac{1}{\kappa\eta V_H}\mu_0 V_m H^2 \chi_0 \frac{1}{\sum_n V_n^2}\sum_n \Omega\tau_0 \exp\left(\frac{KV_p}{k_B T}\right) V_n^2 \tag{3.3}$$

Results and Discussion

To test whether the sandwich complexes follow the model of equation (3.3), we observed the response of the sandwich complexes to changes in amplitude and frequency. Holding all variables except for field amplitude constant, equation (3.3) reduces to $\frac{d\theta}{dt} \propto H^2$. Figure 3.2a shows indeed that the rotational frequency of a sandwich complex is directly proportional to the square of the amplitude of the driving field. Holding all variables constant except for field driving frequency, equation (3.3) reduces to $\frac{d\theta}{dt} \propto \Omega$. Figure 3.2b shows that the rotational frequency of a sandwich complex does increase

with the frequency of the driving field, but it does not exactly demonstrate the linear relationship that equation (3.3) suggests.

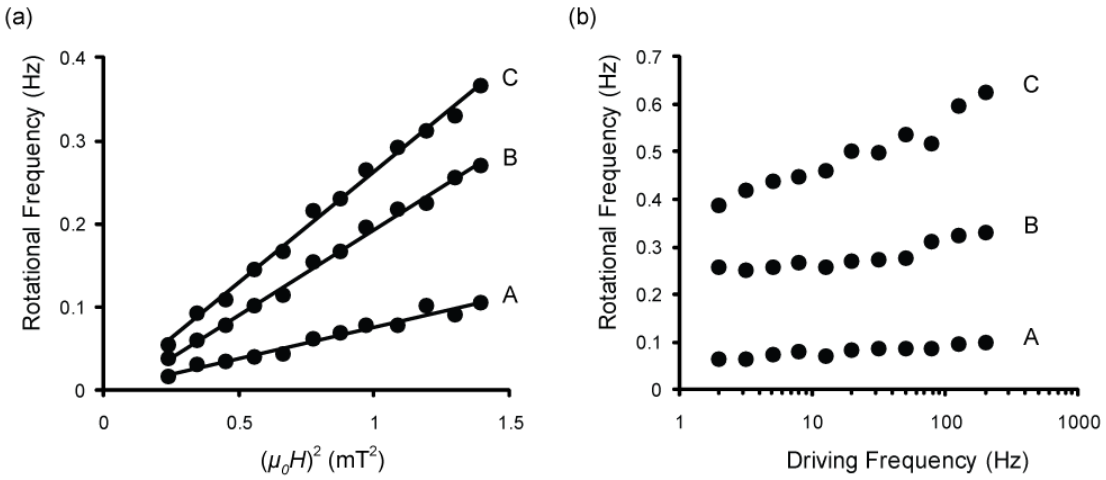

Figure 3.2—(a) Amplitude response curves showing that the rotational frequency of a sandwich complex is proportional to the square of the amplitude of the driving field (with $B=\mu_0 H$). The data are fit with a linear trendline with r^2 values of (A) 0.968, (B) 0.995, and (C) 0.994. (b) Frequency response curves showing that the rotational frequency of a sandwich complex increases with an increase in the frequency of the driving field.

We examined the stability of the rotation of sandwich complexes over 60 minutes of observation. The rotational frequency of four sandwich complexes was measured every 5 minutes for 60 minutes, as shown in Figure 3.3a. The coefficient of variation (standard deviation divided by the mean, times 100%) of the complexes (A-D) was 3.3%, 2.5%, 1.5% and 1.6%, respectively, demonstrating that the rotation of a sandwich complex is fairly stable over a 60 minute observation period. All other measurements reported here were made within an hour of the sandwich complexes being injected into the coverslip fluidic cell.

A dose-response curve of LAM used for measuring the concentration of thrombin in solution is shown in Figure 3.3b. At each thrombin concentration, the rotation of 15

sandwich complexes was measured, and each point in the figure represents the average of those 15 measurements (± standard deviation). The data was fit using the four-parameter logistic Hill equation. [52, 53] The dynamic range of the curve extends from about 1 nM to about 20 nM. Above 20 nM, the curve plateaus. Below 1 nM, there is still a detectable signal down to 300 pM. In the 300 pM to 1 nM range, there was still binding of beads to the mother sphere, but there was no significant difference between the different concentrations. Below 300 pM, no binding of beads to the mother sphere was observed. Similarly, in a control sample (no thrombin), there was also no binding detected. In the absence of the aptamers thrombin does not bind to the spheres and beads. Figure 3.3b demonstrates the viability of LAM as a tool for measuring the concentration of a protein in solution, with an LOD (limit of detection) of 300 pM.

Screenshots of the rotation of five of the sandwich complexes from Figure 3.3b are shown in Figure 3.4. These images show that the number of beads attached to each complex increases with the concentration of thrombin, and that the rotational frequency of the complexes increases with the number of attached beads. These images also show that a qualitative estimate of the protein concentration can be made merely by looking at the complexes under a microscope, without using rotation.

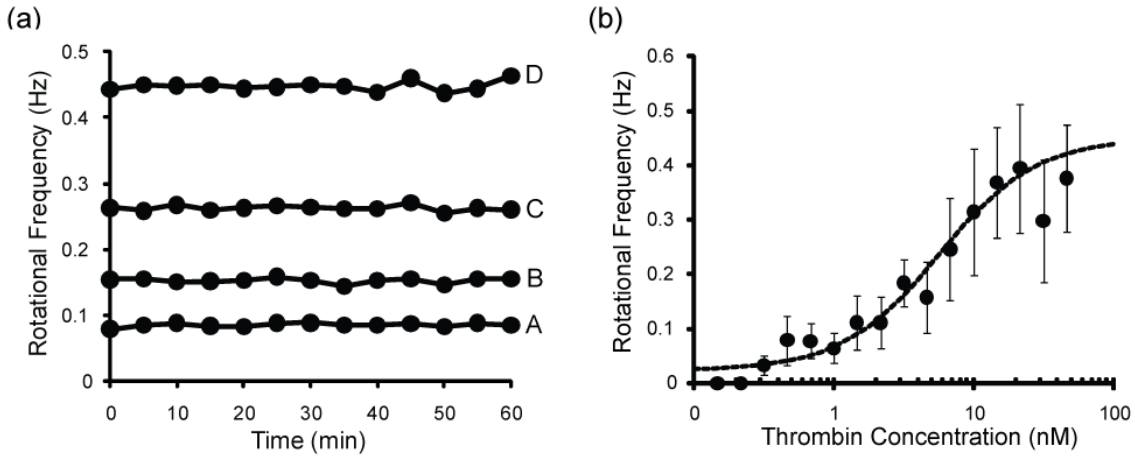

Figure 3.3—(a) The rotational frequency of four sandwich complexes measured every five minutes over the course of an hour. The rotational frequency means, ± SD (CV%) of the four sandwich complexes (A-D) are 0.0856 ± 0.0028 Hz (3.3%), 0.1523 ± 0.0038 Hz (2.5%), 0.263 ± 0.0040 Hz (1.5%) and 0.448 ± 0.0073 Hz (1.6%), respectively. This demonstrates that the rotation of the sandwich complexes is stable over time. (b) Dose-response curve for the detection of thrombin by LAM. The data are fit by a four-parameter logistic equation ($r^2 = 0.971$). Each data point represents the average ± SD of 15 sandwich complexes.

Figure 3.4—Screenshots of five sandwich complexes taken through a 100x oil-immersion objective. The thrombin concentration and the rotational frequency of each complex are shown below the picture. The number of magnetic beads on and the rotational frequency of each sandwich complex appear to increase with concentration of thrombin.

One of the advantages of using the thrombin aptamers is their popularity; many groups have used these aptamers for demonstration of signal transduction techniques.

When examining other methods that are sandwich-based and use single-step (non-amplified) methods, reported LODs typically are in the 0.1-1 nM range, including electrochemical detection, [18, 47] quantum dots, [11] Si-nanowire FETs, [19] and fluorescent molecular beacons. [54] There are many clinically relevant biomarkers found in plasma at concentrations around 1 nM. [55, 56] Within this context, we believe that LAM is certainly competitive with other detection technologies. Moreover, LAM has the advantage of simplicity, robustness and low cost, without requiring sensitive optical readers or other expensive and stationary sensing equipment.

We generated a model in MATLAB, shown in Appendix C-2, to simulate the optimal performance of LAM, assuming perfect mixing and no nonspecific interactions, based on a previously reported two-site immunoassay model. [57] Considering only specific interactions, there are two primary reactions that take place in our system:

$$Q_1 + P \underset{k_{-1}}{\overset{k_1}{\rightleftarrows}} Q_1P \tag{3.4}$$

$$Q_1P + Q_2 \underset{k_{-2}}{\overset{k_2}{\rightleftarrows}} Q_1PQ_2 \tag{3.5}$$

Where P is the protein of interest, Q_1 is the capture aptamer, and Q_2 is the detection aptamer. Also, there are two possible side reactions:

$$Q_2 + P \underset{k_{-3}}{\overset{k_3}{\rightleftarrows}} Q_2P \tag{3.6}$$

$$Q_2P + Q_1 \underset{k_{-4}}{\overset{k_4}{\rightleftarrows}} Q_1PQ_2 \tag{3.7}$$

The model is carried out in two parts, capture and detection. In the capture phase, only equation (3.4) is considered. After the capture reaction has reached equilibrium, the detection phase commences, in which equations (3.4)-(3.7) are all considered. The rate constants for the thrombin aptamers were obtained from previously published work. [58] The model is generated by simultaneously solving the six differential equations below:

$$\frac{d[Q_1]}{dt} = -k_1[Q_1][P] + k_{-1}[Q_1P] - k_4[Q_1][Q_2P] + k_{-4}[Q_1PQ_2] \quad (3.8)$$

$$\frac{d[Q_2]}{dt} = -k_3[Q_2][P] + k_{-3}[Q_2P] - k_2[Q_1P][Q_2] + k_{-2}[Q_1PQ_2] \quad (3.9)$$

$$\frac{d[P]}{dt} = -k_1[Q_1][P] + k_{-1}[Q_1P] - k_3[Q_2][P] + k_{-3}[Q_2P] \quad (3.10)$$

$$\frac{d[Q_1P]}{dt} = k_1[Q_1][P] - k_{-1}[Q_1P] - k_2[Q_1P][Q_2] + k_{-2}[Q_1PQ_2] \quad (3.11)$$

$$\frac{d[Q_2P]}{dt} = k_3[Q_2][P] - k_{-3}[Q_2P] - k_4[Q_1][Q_2P] + k_{-4}[Q_1PQ_2] \quad (3.12)$$

$$\frac{d[Q_1PQ_2]}{dt} = k_2[Q_1P][Q_2] + k_4[Q_1][Q_2P] - (k_{-2} + k_{-4})[Q_1PQ_2] \quad (3.13)$$

The simulated dose-response curve based on this model is shown in Figure 3.5. Deviations of the experimental data from this simulated dose-response curve could be due to nonspecific interactions between the aptamers and other proteins in solution, imperfect mixing, suboptimal aptamer-bead attachment, or experimental error. The rather abrupt plateau at the top of the dose-response curve is due to the saturation of the mother spheres with magnetic beads before saturation with thrombin; only a few hundred beads can bind to the mother sphere, but over a million thrombin molecules could bind to the mother sphere.

It is our long term goal to develop LAM into a signal transduction method that is suitable for use in a point-of-care clinical setting. In order to achieve this goal, several additional steps must be taken. We plan to translate LAM off the microscope and measure the rotation of the sandwich complex using a simple, compact-disc-like, laser-and-photodiode setup [59], together with automated and self-contained mixing, in a microfluidic chip. We also plan to reproduce these results in a biological fluid medium, such as serum. We believe that, after additional development, LAM will be an attractive

tool for use, because it will not require fluorescence readers or a microscope, and the actual detector (the laser and photodiode) would be low-cost. We recognize that these goals will require additional work. The goal of this chapter is to demonstrate the feasibility of LAM as a signal transduction method for measuring the concentration of a protein in solution, for possible future applications as a point-of-care signal transduction method.

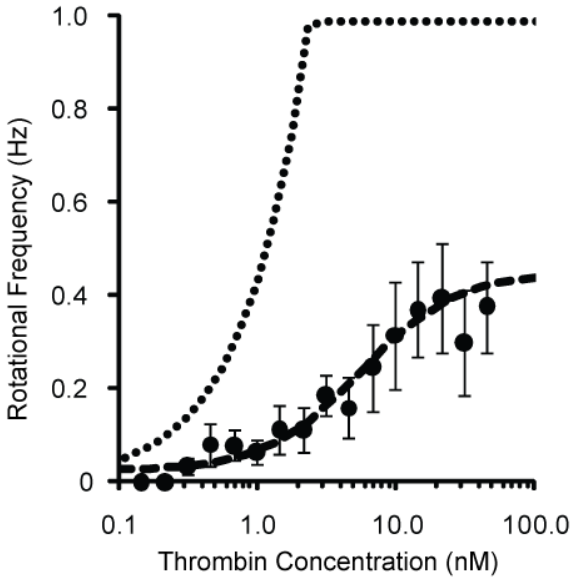

Figure 3.5—Simulated dose-response curve (dotted line) for LAM from a model based on the binding kinetics of the aptamers with thrombin. Also included in the plot are experimental data (dots), from Figure 3.3b, and a logistic curve fit (dashed line). The abrupt plateau at the top of the predicted dose-response curve represents the saturation of the sensor.

Conclusion

In summary, we have demonstrated that label-acquired magnetorotation is a viable signal transduction method for measuring the concentration of a protein in

solution, with a limit of detection of 300 pM of thrombin when using the classic thrombin aptamers. We have shown that the amplitude and frequency response of a sandwich complex generally follow the behavior predicted by the equations that describe superparamagnetic bead behavior. It is our hope for the future that, with further work, LAM will be developed into a viable signal transduction method for point-of-care testing.

Acknowledgments

We thank Alex Hrin for creating the video capture LabVIEW program, Ron Smith for assistance with microscopy and magnetic field setup. This research was partially supported by the Department of Homeland Security (DHS) Scholarship and Fellowship Program, administered by the Oak Ridge Institute for Science and Education (ORISE) through an interagency agreement between the U.S. Department of Energy (DOE) and DHS. ORISE is managed by Oak Ridge Associated Universities (ORAU) under DOE contract number DE-AC05-06OR23100. All opinions expressed in this chapter are the author's and do not necessarily reflect the policies and views of DHS, DOE, or ORAU/ORISE. Additional support came from NSF/DMR grant 0455330 (RK) and NIH R21 EB009550 (RK).

References

1. Institute, N.C. 2010 [cited 2011 5/31/2011]; Available from: http://www.cancer.gov/newscenter/pressreleases/2011/NLSTFastFacts.
2. NLSTRT. The National Lung Screening Trial: Overview and Study Design. *Radiology*, 2011. **258**(1): p. 243-253.
3. Hecht, A., P. Kinnunen, B. McNaughton, and R. Kopelman. Label-acquired magnetorotation for biosensing: An asynchronous rotation assay. *Journal of Magnetism and Magnetic Materials*, 2011. **323**(3-4): p. 272-278.
4. Ekins, R.P. Multi-analyte immunoassay. *Journal of Pharmaceutical and Biomedical Analysis*, 1989. **7**(2): p. 155-168.
5. Engvall, E. and P. Perlmann. Enzyme-Linked Immunosorbent Assay, Elisa. *The Journal of Immunology*, 1972. **109**(1): p. 129-135.
6. Cho, I.-H., E.-H. Paek, Y.-K. Kim, J.-H. Kim, et al. Chemiluminometric enzyme-linked immunosorbent assays (ELISA)-on-a-chip biosensor based on cross-flow chromatography. *Analytica Chimica Acta*, 2009. **632**(2): p. 247-255.
7. Guillet, C., M. Fourcin, S. Chevalier, A. Pouplard, et al. ELISA Detection of Circulating Levels of LIF, OSM, and CNTF in Septic Shock. *Annals of the New York Academy of Sciences*, 1995. **762**(1): p. 407-409.
8. Hayes, M.A., M.M. Petkus, A.A. Garcia, T. Taylor, et al. Demonstration of sandwich and competitive modulated supraparticle fluoroimmunoassay applied to cardiac protein biomarker myoglobin. *Analyst*, 2009. **134**(3): p. 533-541.
9. Yang, X., X. Li, T.W. Prow, L.M. Reece, et al. Immunofluorescence assay and flow-cytometry selection of bead-bound aptamers. *Nucleic Acids Res*, 2003. **31**(10): p. e54.
10. Urdea, M.S., B.D. Warner, J.A. Running, M. Stempien, et al. A comparison of non-radioisotopic hybridization assay methods using fluorescent, chemiluminescent and enzyme labeled synthetic oligodeoxyribonucleotide probes. *Nucleic Acids Research*, 1988. **16**(11): p. 4937-4956.
11. Tennico, Y.H., D. Hutanu, M.T. Koesdjojo, C.M. Bartel, et al. On-Chip Aptamer-Based Sandwich Assay for Thrombin Detection Employing Magnetic Beads and Quantum Dots. *Analytical Chemistry*, 2010. **82**(13): p. 5591-5597.
12. Su, X.-L. and Y. Li. Quantum Dot Biolabeling Coupled with Immunomagnetic Separation for Detection of Escherichia coli O157:H7. *Analytical Chemistry*, 2004. **76**(16): p. 4806-4810.
13. Soelberg, S.D., R.C. Stevens, A.P. Limaye, and C.E. Furlong. Surface Plasmon Resonance Detection Using Antibody-Linked Magnetic Nanoparticles for Analyte Capture, Purification, Concentration, and Signal Amplification. *Analytical Chemistry*, 2009. **81**(6): p. 2357-2363.

14. Huang, J.-G., C.-L. Lee, H.-M. Lin, T.-L. Chuang, et al. A miniaturized germanium-doped silicon dioxide-based surface plasmon resonance waveguide sensor for immunoassay detection. *Biosensors and Bioelectronics*, 2006. **22**(4): p. 519-525.

15. Chinowsky, T.M., J.G. Quinn, D.U. Bartholomew, R. Kaiser, et al. Performance of the Spreeta 2000 integrated surface plasmon resonance affinity sensor. *Sensors and Actuators B: Chemical*, 2003. **91**(1-3): p. 266-274.

16. Meyerhoff, M., C. Duan, and M. Meusel. Novel nonseparation sandwich-type electrochemical enzyme immunoassay system for detecting marker proteins in undiluted blood. *Clinical Chemistry*, 1995. **41**(9): p. 1378-1384.

17. Dai, Z., F. Yan, J. Chen, and H. Ju. Reagentless Amperometric Immunosensors Based on Direct Electrochemistry of Horseradish Peroxidase for Determination of Carcinoma Antigen-125. *Analytical Chemistry*, 2003. **75**(20): p. 5429-5434.

18. Cai, H., T.M.-H. Lee, and I.M. Hsing. Label-free protein recognition using an aptamer-based impedance measurement assay. *Sensors and Actuators B: Chemical*, 2006. **114**(1): p. 433-437.

19. Kim, K.S., H.-S. Lee, J.-A. Yang, M.-H. Jo, et al. The fabrication, characterization and application of aptamer-functionalized Si-nanowire FET biosensors. *Nanotechnology*, 2009. **20**(23): p. 235501.

20. Pamme, N. Magnetism and microfluidics. *Lab on a Chip*, 2006. **6**(1): p. 24-38.

21. Gijs, M.A.M., F. Lacharme, and U. Lehmann. Microfluidic Applications of Magnetic Particles for Biological Analysis and Catalysis. *Chemical Reviews*, 2010. **110**(3): p. 1518-1563.

22. Osterfeld, S.J., H. Yu, R.S. Gaster, S. Caramuta, et al. Multiplex protein assays based on real-time magnetic nanotag sensing. *Proceedings of the National Academy of Sciences of the United States of America*, 2008. **105**(52): p. 20637-20640.

23. Edelstein, R.L., C.R. Tamanaha, P.E. Sheehan, M.M. Miller, et al. The BARC biosensor applied to the detection of biological warfare agents. *Biosensors & Bioelectronics*, 2000. **14**(10-11): p. 805-813.

24. Schotter, J., P.B. Kamp, A. Becker, A. Pühler, et al. Comparison of a prototype magnetoresistive biosensor to standard fluorescent DNA detection. *Biosensors and Bioelectronics*, 2004. **19**(10): p. 1149-1156.

25. Besse, P.-A., G. Boero, M. Demierre, V. Pott, et al. Detection of a single magnetic microbead using a miniaturized silicon Hall sensor. *Applied Physics Letters*, 2002. **80**(22): p. 4199-4201.

26. Sandhu, A., H. Handa, and M. Abe. Synthesis and applications of magnetic nanoparticles for biorecognition and point of care medical diagnostics. *Nanotechnology*, 2010. **21**(44): p. 442001.

27. Lee, H., E. Sun, D. Ham, and R. Weissleder. Chip-NMR biosensor for detection and molecular analysis of cells. *Nature Medicine*, 2008. **14**(8): p. 869-874.

28. Chung, S.H., A. Hoffmann, S.D. Bader, C. Liu, et al. Biological sensors based on Brownian relaxation of magnetic nanoparticles. *Applied Physics Letters*, 2004. **85**(14): p. 2971-2973.

29. Choi, J.-W., T.M. Liakopoulos, and C.H. Ahn. An on-chip magnetic bead separator using spiral electromagnets with semi-encapsulated permalloy. *Biosensors and Bioelectronics*, 2001. **16**(6): p. 409-416.

30. Hayes, M.A., N.A. Polson, A.N. Phayre, and A.A. Garcia. Flow-Based Microimmunoassay. *Analytical Chemistry*, 2001. **73**(24): p. 5896-5902.

31. Pamme, N. and A. Manz. On-Chip Free-Flow Magnetophoresis: Continuous Flow Separation of Magnetic Particles and Agglomerates. *Analytical Chemistry*, 2004. **76**(24): p. 7250-7256.

32. Fonnum, G., C. Johansson, A. Molteberg, S. Morup, et al. Characterisation of Dynabeads (R) by magnetization measurements and Mossbauer spectroscopy. *Journal of Magnetism and Magnetic Materials*, 2005. **293**(1): p. 41-47.

33. Fannin, P.C., L. Cohen-Tannoudji, E. Bertrand, A.T. Giannitsis, et al. Investigation of the complex susceptibility of magnetic beads containing maghemite nanoparticles. *Journal of Magnetism and Magnetic Materials*, 2006. **303**(1): p. 147-152.

34. Janssen, X.J.A., A.J. Schellekens, K. van Ommering, L.J. van Ijzendoorn, et al. Controlled torque on superparamagnetic beads for functional biosensors. *Biosensors & Bioelectronics*, 2009. **24**(7): p. 1937-1941.

35. McNaughton, B.H., K.A. Kehbein, J.N. Anker, and R. Kopelman. Sudden breakdown in linear response of a rotationally driven magnetic microparticle and application to physical and chemical microsensing. *Journal of Physical Chemistry B*, 2006. **110**(38): p. 18958-18964.

36. Kinnunen, P., I. Sinn, B.H. McNaughton, D.W. Newton, et al. Monitoring the growth and drug susceptibility of individual bacteria using asynchronous magnetic bead rotation sensors. *Biosensors and Bioelectronics*, 2011. **26**(5): p. 2751-2755.

37. Kinnunen, P., I. Sinn, B.H. McNaughton, and R. Kopelman. High frequency asynchronous magnetic bead rotation for improved biosensors. *Applied Physics Letters*, 2010. **97**(22): p. 223701-223701-3.

38. McNaughton, B.H., R.R. Agayan, R. Clarke, R.G. Smith, et al. Single bacterial cell detection with nonlinear rotational frequency shifts of driven magnetic microspheres. *Applied Physics Letters*, 2007. **91**(22): p. -.

39. McNaughton, B.H., R.R. Agayan, J.X. Wang, and R. Kopelman. Physiochemical microparticle sensors based on nonlinear magnetic oscillations. *Sensors and Actuators B-Chemical*, 2007. **121**(1): p. 330-340.

40. Turek, C. and L. Gold. Systematic evolution of ligands by exponential enrichment: RNA ligands to bacteriophage T4 DNA polymerase. *Science*, 1990. **249**: p. 505-510.

41. Ellington, A.D. and J.W. Szostak. In vitro selection of RNA molecules that bind specific ligands. *Nature*, 1990. **346**: p. 818-822.

42. Bock, L.C., L.C. Griffin, J.A. Latham, E.H. Vermaas, et al. Selection of single-stranded DNA molecules that bind and inhibit human thrombin. *Nature*, 1992. **355**(6360): p. 564-566.

43. Tasset, D.M., M.F. Kubik, and W. Steiner. Oligonucleotide inhibitors of human thrombin that bind distinct epitopes. *Journal of Molecular Biology*, 1997. **272**(5): p. 688-698.

44. Cho, H., B.R. Baker, S. Wachsmann-Hogiu, C.V. Pagba, et al. Aptamer-Based SERRS Sensor for Thrombin Detection. *Nano Letters*, 2008. **8**(12): p. 4386-4390.

45. Xiao, Y., A.A. Lubin, A.J. Heeger, and K.W. Plaxco. Label-Free Electronic Detection of Thrombin in Blood Serum by Using an Aptamer-Based Sensor. *Angewandte Chemie*, 2005. **117**(34): p. 5592-5595.

46. Strehlitz, B., N. Nikolaus, and R. Stoltenburg. Protein Detection with Aptamer Biosensors. *Sensors*, 2008. **8**(7): p. 4296-4307.

47. Centi, S., S. Tombelli, M. Minunni, and M. Mascini. Aptamer-Based Detection of Plasma Proteins by an Electrochemical Assay Coupled to Magnetic Beads. *Analytical Chemistry*, 2007. **79**(4): p. 1466-1473.

48. Huang, C.-C., Z. Cao, H.-T. Chang, and W. Tan. Protein−Protein Interaction Studies Based on Molecular Aptamers by Affinity Capillary Electrophoresis. *Analytical Chemistry*, 2004. **76**(23): p. 6973-6981.

49. Milne, G., *Optical Sorting and Manipulation of Microscopic Particles*. 2007, University of St. Andrews.

50. Connolly, J. and T.G. St Pierre. Proposed biosensors based on time-dependent properties of magnetic fluids. *Journal of Magnetism and Magnetic Materials*, 2001. **225**(1-2): p. 156-160.

51. Bodker, F., S. Morup, and S. Linderoth. Surface Effects in Metallic Iron Nanoparticles. *Physical Review Letters*, 1994. **72**(2): p. 282-285.

52. Baud, M., *Data Analysis, Mathematical Modeling*, in *Methods of Immunological Analysis*, R. Masseyeff, Editor. 1993, VCH Publishers, Inc.: New York, NY. p. 656-671.

53. Hecht, A.H., G.J. Sommer, R.H. Durland, X. Yang, et al. Aptamers as Affinity Reagents in an Integrated Electrophoretic Lab-on-a-Chip Platform. *Analytical Chemistry*, 2010. **82**(21): p. 8813-8820.

54. Radi, A.-E., J.L. Acero Sánchez, E. Baldrich, and C.K. O'Sullivan. Reagentless, Reusable, Ultrasensitive Electrochemical Molecular Beacon Aptasensor. *Journal of the American Chemical Society*, 2005. **128**(1): p. 117-124.

55. Polanski, M. and N.L. Anderson. A list of candidate cancer biomarkers for targeted proteomics. *Biomarker Insights*, 2006. **2**: p. 1-48.

56. Jacobs, J.M., J.N. Adkins, W.-J. Qian, T. Liu, et al. Utilizing Human Blood Plasma for Proteomic Biomarker Discovery†. *Journal of Proteome Research*, 2005. **4**(4): p. 1073-1085.

57. Rodbard, D. and Y. Feldman. Kinetics of two-site immunoradiometric ("sandwich") assays--I: Mathematical models for simulation, optimization, and curve fitting. *Immunochemistry*, 1978. **15**(2): p. 71-76.

58. Muller, J., D. Freitag, G. Mayer, and B. Potzsch. Anticoagulant characteristics of HD1-22, a bivalent aptamer that specifically inhibits thrombin and prothrombinase. *Journal of Thrombosis and Haemostasis*, 2008. **6**(12): p. 2105-2112.

59. McNaughton, B.H., P. Kinnunen, R.G. Smith, S.N. Pei, et al. Compact sensor for measuring nonlinear rotational dynamics of driven magnetic microspheres with biomedical applications. *Journal of Magnetism and Magnetic Materials*, 2009. **321**(10): p. 1648-1652.

Chapter 4

Bead Assembly Magnetorotation as a Signal Transduction Method for Protein Detection

Introduction

Magnetic beads have several advantages that make them attractive candidates for use as biosensor signal transducers, including their biological inertness, physical stability, and the absence of competing magnetic signals in biological materials. [1, 2] A number of magnetism-based protein detection techniques have been developed, including giant magnetoresistance (GMR) [3-5], magnetic relaxation, [6, 7] Hall Probes, [8, 9] and amplification of an optical signal by magnetic rotation. [10, 11] Additionally, there have been reports of using proteins to mediate the formation of one-dimensional magnetic bead chains. [12, 13] However, to the best of our knowledge, there have been no previous reports studying the shape or drag of two-dimensional magnetic microbead assemblies for their use as biomarker signal transducers.

This work builds on previous reports on the use of asynchronous magnetorotation for biological applications. Asynchronous magnetorotation was employed in a sandwich-type biosensor, where the magnetic beads acted as labels attached to nonmagnetic spheres, whose rotational frequency depended on the number of attached magnetic bead

labels. [14, 15] Asynchronous magnetorotation was also used to measure the growth rate of attached bacteria, [16-18] and morphological changes of cancer cells. [19]

The beads used in this study are 1 μm Invitrogen™ Dynabeads. These beads, which exhibit superparamagnetic behavior, are composed of maghemite nanoparticles (γ-Fe_2O_3), with a mean diameter of 8 nm, dispersed in a polystyrene matrix. [20] In the absence of a magnetic field, these beads exhibit no net magnetization, but within a magnetic field, the magnetic moments of the bead align with the field, making the beads magnetic.

It has previously been shown that within a two-dimensional rotating magnetic field, the dominant physical mechanism driving the rotation of the beads is the Neel relaxation of the γ-Fe_2O_3 nanoparticles embedded inside the bead. [14, 15, 21-23] At low driving field frequencies, the beads rotate in-phase with the driving field. At high driving field frequencies, the beads rotate out-of-phase, asynchronously, with the driving field. It is this asynchronous rotation, which depends on the physical properties of the beads, that allows for their rotation to be used to make biological measurements.

The use of surface-attached DNA molecules to control the assembly of micro- and nano-scale materials into highly-ordered crystalline structures has been shown before. [24-26] However, while those projects focused on the creation of single crystalline structures, the present project advances the concept one step further by focusing on the creation of structurally tunable assemblies, i.e. assemblies that can assume a variety of structures, depending on the protein concentration

The protein target used in this project is the blood coagulation factor thrombin, and the affinity molecules used are the well-studied thrombin aptamers. [27, 28]

Thrombin was chosen because of its popularity as an analyte in proof-of-principle studies, which facilitates evaluation of our method in the context of other methods. There are many papers demonstrating proof-of-principle work on signal transduction methods, all using the same thrombin aptamers in buffer, with reported limits of detection (LOD) ranging from 20 nM down to 6 fM. [29-48] To demonstrate the utility of our magnetorotation method, we studied the same biomarker, thrombin, using the same aptamers, and under similar conditions. Thus, while we intend to pursue biomarker detection in serum at a later time, here we limit our focus primarily to work on thrombin in buffer.

Materials and Methods

Materials

The magnetic beads used were 1 μm streptavidin-coated Dynabeads T1 MyOne beads (Invitrogen, Carlsbad, CA). The 1 μm beads used were selected after examining a wide range of beads, from 100 nm to 5 μm, optimizing parameters such as sedimentation rate, available binding sites, and magnetic volume. Human α-thrombin was purchased from Haematologic Technologies (Essex Junction, VT). Two anti-thrombin aptamers were used, the 15-mer (5'-GGT TGG TGT GGT TGG) [27] and 29-mer (5'-AGT CCG TGG TAG GGG CAG GTT GGG TGA CT) [28], with 20-base polyT tails, [34] and were synthesized with a 5'-biotinylation by Integrated DNA Technologies (Coralville, IA). Standard salts and Tween-20 were purchased from Sigma Aldrich (St. Louis, MO). Bovine serum albumin (BSA) 10% blocker solution was purchased from Thermo Scientific (Waltham, MA). Teflon-coated glass slides with 1 mm exposed glass spots

were purchased from Tekdon, Inc. (Myakka City, FL). AS568-016 BN70 nitrile O-rings were purchased from Orings, Inc. (Los Angeles, CA). G661 general purpose lubricant was purchased from Novagard (Cleveland, OH).

A two-dimensional rotating magnetic field was constructed from orthogonal Helmholtz coils. The coils were built by 3D-printing a plastic mold consisting of four orthogonal rings, and wrapping coils of 22 gauge copper wire around the rings. Two sinusoidal waves, 90 degrees out-of-phase, were used to power the field and were generated within a LabVIEW program (National Instruments, Austin, TX), passed through a LabVIEW DAQ Board (NI USB-6211or NI SCB-68 connected to NI PCIe-6321), amplified by a TX-PA40D two-channel amplifier (Radio Design Labs, Prescott, AZ), and then passed to the coils. The field had a frequency of 50 Hz and an amplitude of 4 mT. The field rotated in a two-dimensional plane, which drove the rotation of the bead assemblies. The magnetic beads have a susceptibility (χ) of 8.1 x 10^{-4} m^3/kg. [20]

Videos for magnetorotation analysis were captured on an Olympus IX71 inverted microscope (Olympus, Melville, NY) through a Basler piA640-210gm camera (Basler, Highland, IL). Videos were analyzed using the StAT Tracker [49] program written in LabVIEW and a MATLAB program, which is included in Appendix C-1. Higher resolution images for fractal analysis were captured on an Olympus BX50WI upright microscope through a Mightex BCE-B050-U camera (Mightex Systems, Toronto, Ontario, Canada). Images were analyzed using the FracLac plugin [50] for ImageJ (National Institutes of Health, Bethesda, MD).

For the laser-photodiode detection setup, a 650 nm, 20 mW laser module was purchased from Information Unlimited (Amherst, NH). FDS100 photodiodes were

purchased from ThorLabs (Newton, NJ). The components were secured using standard optic table equipment. Conditioning circuitry was built using standard electronics components. The conditioned signal was passed through the NI SCB-68 DAQ board and processed and analyzed in LabVIEW.

Preparation of Bead Assemblies

Wash buffer (1 M NaCl, 20 mM Tris, 1 mM EDTA, pH = 7.5), aptamer binding buffer (1 M NaCl, 5 mM Tris, 1 mM EDTA, pH = 7.5) and thrombin binding buffer (140 nM NaCl, 50 mM Tris, 1 mM $MgCl_2$, 10 mM KCl, 0.1% Tween-20, 0.1% BSA, pH = 7.4) were prepared. [30, 34] A 10 μL aliquot of the magnetic beads (10 mg/mL) was washed three times with the wash buffer, and then resuspended in 100 μL of aptamer binding buffer, and split into two portions. To each of the portions was added 3 μL of 50 μM aptamer solution (either the 15-mer or the 29-mer), which represented a ten-fold molar excess, ensuring that the beads would be well functionalized with the aptamer, and they were incubated with gentle mixing for one hour. The biotinylated aptamers were attached to the streptavidin-coated beads via the biotin-streptavidin bond. The beads were washed three times with thrombin binding buffer, and resuspended at various concentrations (7 μg/mL, 22 μg/mL, 70 μg/mL, 220 μg/mL). Solutions of thrombin protein were diluted to various concentrations (ranging from 10 fM to 1 nM) with thrombin binding buffer. 100 μL of thrombin solution was mixed with 5 μL of a solution of 29-mer beads, incubated with gentle mixing for 10 minutes, followed by the addition of 5 μL of a solution of 15-mer beads at the same bead concentration. For control solutions, 100 μL of thrombin binding buffer, with no thrombin added, was used.

Hanging droplets were prepared on a Teflon-coated slide, with an O-ring greased with lubricating grease in the middle (for sealing). Sixteen 1 μL droplets of thrombin-bead solution were placed on the 1-mm exposed glass spots on the slide in a 4-by-4 array. The other side of the O-ring was greased, and a clear glass slide was placed on top, creating a seal around the droplets (this was to prevent evaporation as well as to minimize air currents disrupting the droplets). The slides were then inverted, so that the droplets hung down from the Teflon-coated slide. The slides were allowed to sit for 30 minutes, during which the beads fell through the solution, under the influence of gravity (bead density = 1.9 g/cm^3). As the beads fell towards the tip of the droplet, if they encountered a thrombin molecule, the beads could bind to each other. In the absence of thrombin molecules, the beads collected in a tight cluster in the center of the droplet. The slides were then placed in the rotating magnetic field for magnetorotation and further analysis.

Results and Discussion

A schematic showing the formation of the bead assemblies is shown in Figure 4.1 After the beads are mixed in a microcentrifuge tube, and transferred to the hanging droplet, the beads fall to the bottom of the droplet, and form an assembly. In the absence of thrombin, there is nothing to bind the beads together, and they form a tight hexagonally-packed assembly, as shown in Figure 4.1d and in the image in Figure 4.1f. As the concentration of thrombin increases, the likelihood increases that an aptamer on the surface of one of the beads will bind to a thrombin molecule, and that it will encounter a second bead that has a free complementary aptamer on its surface, and that the thrombin molecule will bind to the second aptamer, linking the beads together. As the

concentration of thrombin increases, the number of beads that bind to each other increases. This results in a less-densely packed assembly of beads, one that has increased lacunarity ("gapiness"), and a decreased fractal dimension. At high thrombin concentrations, where each bead has many thrombin molecules bound to its surface, the conditions approach those of diffusion-limited aggregation: the bead density is relatively low, the primary means of transport is diffusion, and the beads bind instantly and irreversibly upon contact. [51] This results in the highly-branched bead assembly shown in Figure 4.1e, and in the image in Figure 4.1g.

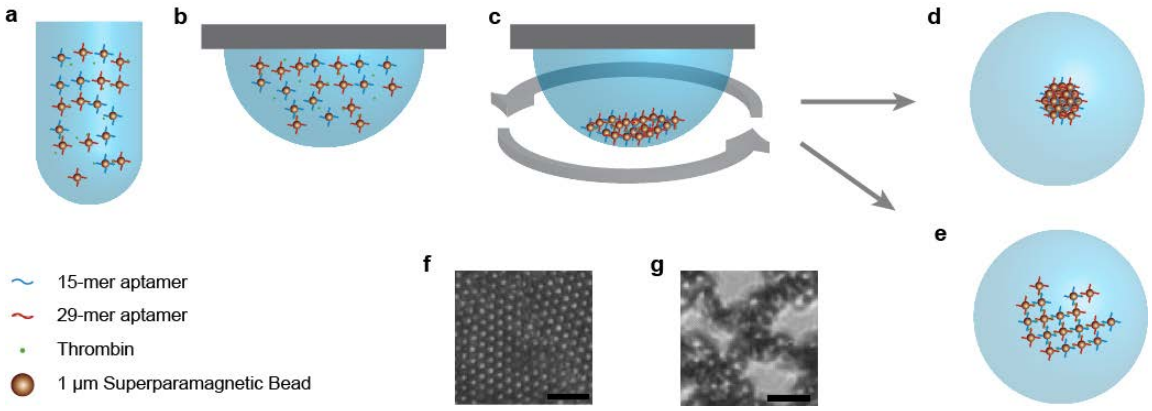

Figure 4.1—Schematic illustration of the bead assembly magnetorotation. (a), Beads coated with 29-mer thrombin aptamer are mixed with thrombin in a microcentrifuge tube, followed by addition of the 15-mer aptamer coated beads. (b) A 1 µL droplet of the bead solution is transferred to an inverted droplet. (c) The beads fall to the bottom of the droplet. A rotating magnetic field is then applied, to pull together beads which are not bound to thrombin. (d) In the case of no or low protein concentration, the beads assume a tightly-packed hexagonal arrangement. (e) In the case of high protein levels, the beads assume a highly branched structure. (f) A brightfield microscope image of hexagonally packed beads in the absence of protein. Imaged through a 40x water-immersion objective. Scale bar = 5 µm. (g) A brightfield microscope image of a loosely-packed bead assembly in the presence of high protein concentration. Imaged through a 40x water-immersion objective. Scale bar = 5 µm.

Magnetorotation Theory

The theory behind the rotation of microbeads composed of superparamagnetic nanoparticles has been discussed in depth elsewhere, [14, 15, 21-23] and will be summarized here. Briefly, we start with the equation for magnetic torque, $\boldsymbol{\tau} = \mathbf{m} \times \mathbf{B}$, where **m** is the magnetic moment of the bead, and **B** is the strength of the external magnetic field. Assuming steady state rotation, the rotational driving forces are equal in magnitude and opposite in direction to the viscous drag forces. Setting up a torque balance, the drag term can be expanded, $\tau = \kappa \eta V_H / T$, where κ is the shape factor, η is the fluid viscosity, V_H is the hydrodynamic volume, and T is the rotational period. The rotational driving forces can be expanded with the following substitutions, $\mathbf{B} = \mu_0 \mathbf{H}$, where μ_0 is the permeability of free space, **H** is the magnetizing field; $\mathbf{m} = V_m \mathbf{M}$, where V_m is the volume of magnetic material, and **M** is the volumetric magnetic moment; $\mathbf{M} = \chi \mathbf{H}$, where χ is the magnetic susceptibility of the bead; and $\chi = \chi' - i\chi''$, where χ' is the real component of the bead susceptibility, and χ'' is the imaginary component of the bead susceptibility. We can combine all of these expressions to create an equation for the rotational period of the bead:

$$T = \frac{\kappa \eta V_H}{\mu_0 V_m \chi'' H^2} \tag{4.1}$$

This equation can be expressed in terms of experimentally measurable parameters by making further substitutions: $\chi'' = \chi_0 (\Omega \tau_N) / (1 + \Omega^2 \tau_N^2)$, where χ_0 is the DC bead susceptibility, Ω is the frequency of the driving field, and τ_N is the Neel relaxation time; $\tau_N = \exp\{(KV_p) / (k_B T_K)\}$, where K is the magnetic anisotropy constant, V_p is the volume

of the magnetic nanoparticles, k_B is Boltzmann's constant and T_K is the ambient temperature.

With our experimental setup, it's possible to hold most of the terms in equation (4.1) constant. Assuming that all of the bead aggregates have a circular shape, κ is held constant. Assuming that all aggregates are formed with the same number of beads, V_m is constant, and assuming that all the beads have similar material properties, χ'' is constant. Holding H and η constant across all experiments is simple. That leaves only V_H as a variable that can change among experiments, so equation (4.1) can be simplified to:

$$T \propto V_H \tag{4.2}$$

Therefore, the rotational period of the self-assembled aggregate varies only with its hydrodynamic volume.

Bead assemblies were prepared using four different bead concentrations: 7 μg/mL, 22 μg/mL, 70 μg/mL and 220 μg/mL, which enabled an increased overall dynamic range. Figure 4.2 shows a series of images of bead assemblies produced with a bead concentration of 220 μg/mL, illustrating the effects of thrombin concentration on the size, shape, fractal dimension and lacunarity of the bead assemblies. Additional images, with bead concentrations of 22 and 70 μg/mL, are shown in the Figure 4.3.

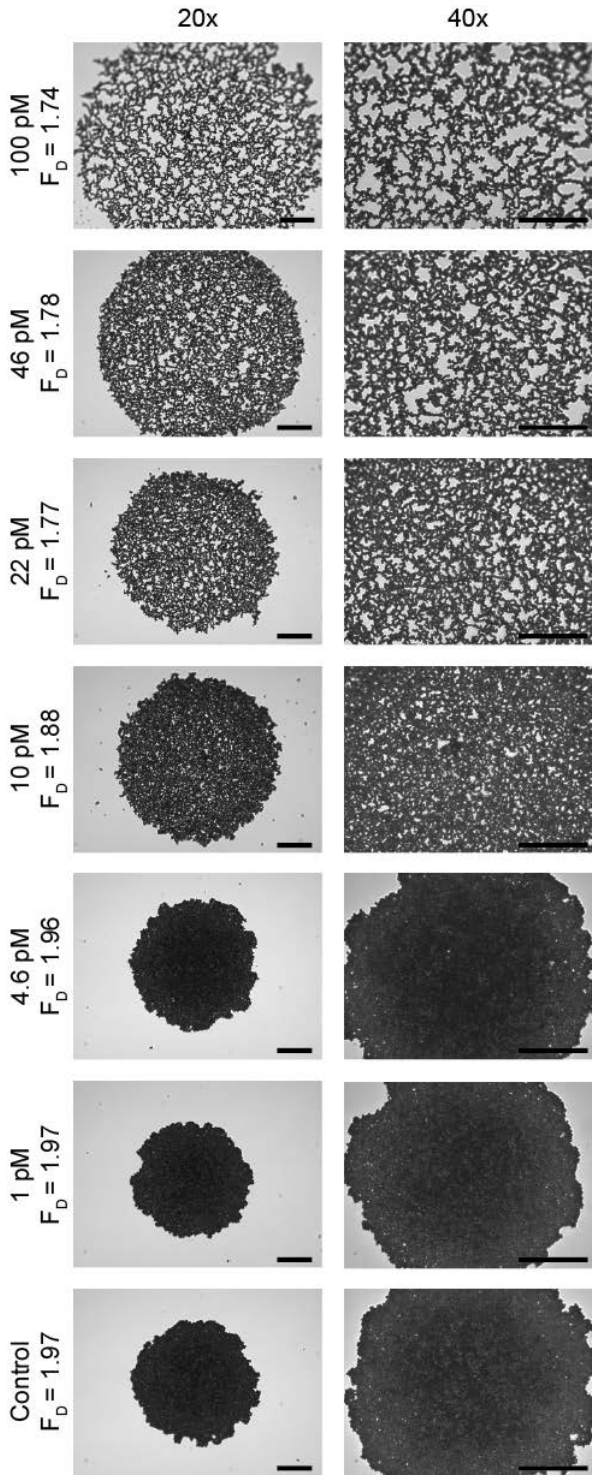

Figure 4.2—A series of brightfield microscope images illustrating the effects of protein concentration on the shape, lacunarity and fractal dimension of the bead assemblies. Initial bead concentration was 220 μg/mL. The fractal dimension for each bead assembly is provided. Left column was taken using a 20x water-immersion objective, right column was taken using a 40x- water-immersion objective. Scale bar = 20 μm.

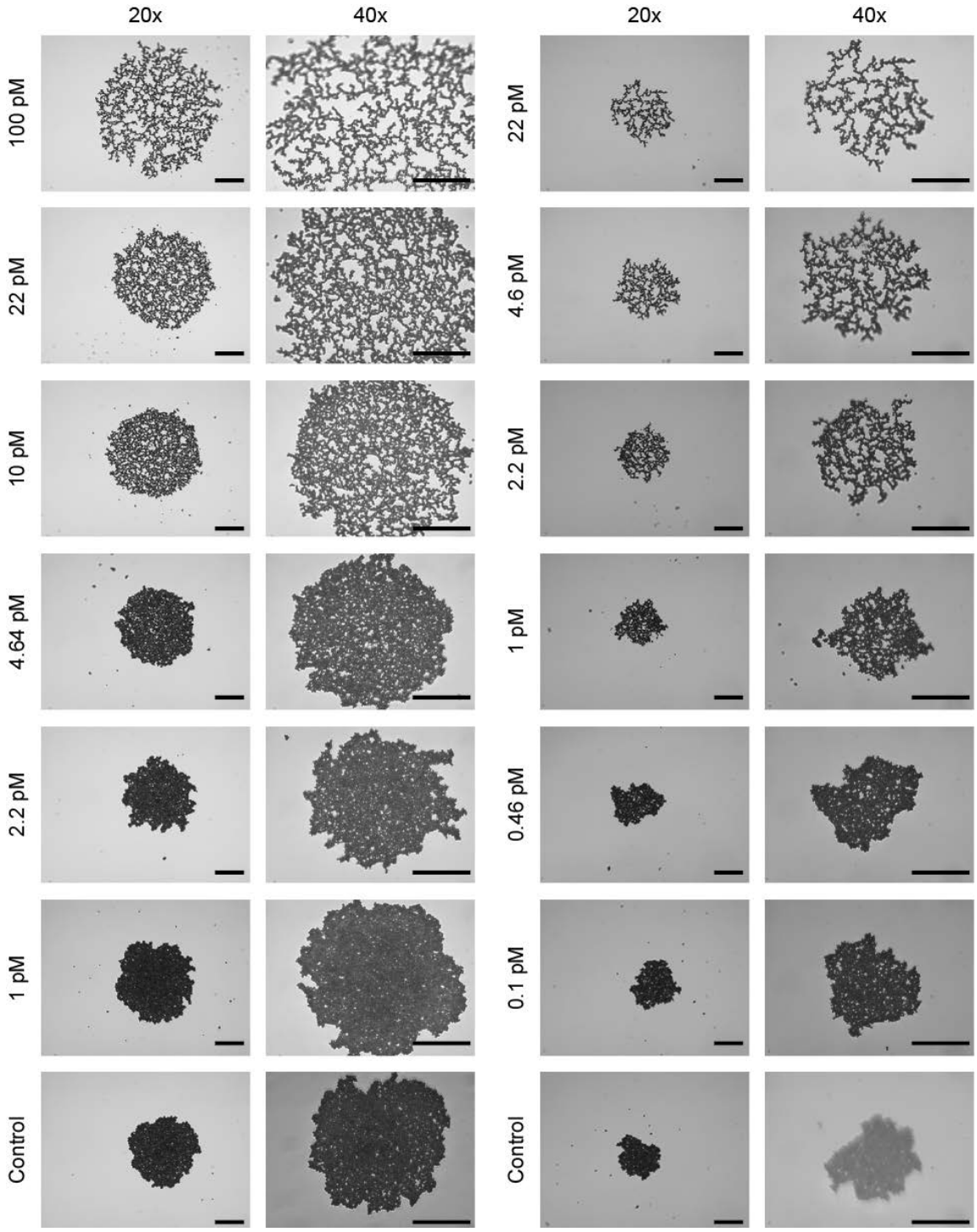

Figure 4.3—A series of brightfield microscope images illustrating the effects of protein concentration on the shape, lacunarity and fractal dimension of the resulting bead clusters. Initial bead concentration was 70 μg/mL (left 2 columns) and 22 μg/mL (right 2 columns). Scale bar = 20 μm.

Rotational Period Dose Response Curves

Figure 4.4 shows a series of dose-response curves for the magnetorotation of the bead assemblies at the four different bead concentrations. The data is normalized over the range of 1-10 seconds to facilitate comparison between the different bead concentrations (the non-normalized data, shown in Figure 4.5, ranges from 1-15 seconds). The data was normalized through the logistic Hill equation that fit the data. After the original data was fit with the Hill equation, for the parameters of the Hill equation, the data was normalized by setting the rotational period at zero concentration to 1 s/s, and the rotational period at infinite concentration to 10 s/s, and creating a linear relationship to scale the original logistic fit to the normalized logistic fit. This relationship was then applied to the data. The dynamic range shifts to the right and limit of detection (LOD) increases as the concentration of beads increases. This is because the dynamic range and LOD depend on the ratio of thrombin molecules per bead (this is discussed in further detail below and in Table 4.1). Based on the average number of thrombin molecules and beads in solution at the LOD, and the energy of the thrombin-aptamer bond, it seems possible that only a single thrombin molecule is needed to bind any two beads together, as a step in the formation of a bead assembly, in the hanging droplet. Each data point on the graph represents the average of ten bead assemblies (± SD). The coefficient of variation decreases with increasing bead concentration, because a larger number of beads increases the uniformity of the assemblies.

The LOD for each bead concentration, as shown in Figure 4.4b, is calculated based on the average rotational period of the control plus three standard deviations, and then determining the concentration that corresponds with that period along the logistic

curve that fits the data. [52] The data is fit with the logistic Hill equation. [53] The LOD of the lowest bead concentration, 7 µg/mL, is 80 fM, which is among the lowest LODs reported for a thrombin-based diagnostic system in buffer [29-48, 54]. Of these papers, only three [34, 39, 40] report quantitative results measured in whole or diluted serum, all of which show much higher limits of detection than in buffer. We believe that these observations reflect the challenges associated with using the specific thrombin aptamers in a complex matrix, such as serum. This issue is discussed in greater detail in Chapter 5.

a

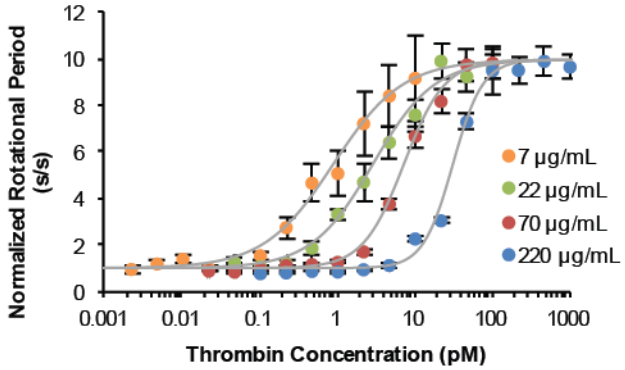

b

Bead Concentration (µg/mL)	Limit of Detection (pM)	Control ± SD (s/s)
7	0.080	0.622 ± 0.053
22	0.195	0.887 ± 0.056
70	1.06	0.932 ± 0.034
220	5.30	0.995 ± 0.036

Figure 4.4—(a) Dose-response curves for the normalized rotational period of bead assemblies from 4 bead concentrations, 7 µg/mL, 22 µg/mL, 70 µg/mL and 220 µg/mL. The curves are fit with the logistic Hill equation. The rotational periods of the bead assemblies were normalized, based on the Hill equation fit through each point, such that the curve had a minimum value of 1 s/s and a maximum value of 10 s/s. This was done to make it easier to compare the behaviors of the different curves. Each point represents the average of the rotational period of ten bead assemblies, and the error bars are ± SD. (b) A table showing the limit of detection (LOD) for each bead concentration, as well as the normalized rotational periods of the control bead assemblies (no thrombin) for each bead concentration. The limit of detection was calculated as the mean control value ± 3 SD.

a

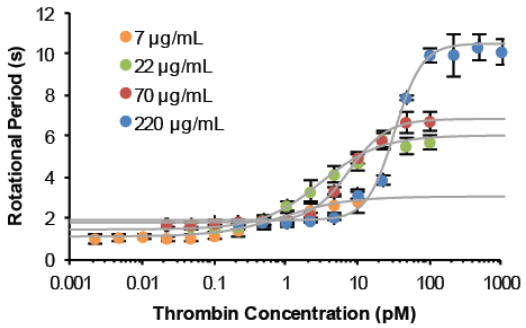

b

Bead Concentration (µg/mL)	Limit of Detection (pM)	Control ± SD (s/s)
7	0.080	0.972 ± 0.083
22	0.195	1.43 ± 0.090
70	1.06	1.77 ± 0.060
220	5.30	1.86 ± 0.068

Figure 4.5— (a) Rotational period of self-assembled microbead aggregates with different microbead concentrations and different thrombin concentrations. Each point represents the mean ± SD of 10 aggregates. Each data set was fit with the logistic Hill equation. (b) Limit of detection and control values corresponding to the data shown in (a). The limit of detection was calculated as the mean control value ± 3 SD.

Calculation of Binding Site Occupation on the Beads

The following calculations will show how we've calculated the number of thrombin molecules that are bound to each bead. The 29-mer beads are first mixed with the thrombin. These beads have a reported binding capacity of 400 pmol biotin/mg beads, [55] which is enough to bind all the thrombin present in our solutions (see Table 4.1). Based on the reported bead density of 1.9 g/mL, [55] each bead has a mass of approximately 10^{-9} mg, which means that each bead can bind approximately 240,000 biotinylated molecules. Solutions are prepared by mixing 4.8 µL of the 29-mer beads (it is the concentration of this solution on which we base on determination of bead concentration, e.g., 220 µg/mL) with 100 µL of thrombin solution, followed by the subsequent addition of 4.8 µL of the 15-mer beads. This produces a solution with final volume of 109.6 µL, from which the 1 µL droplets are produced. Based on these numbers, we calculated the average number of thrombin molecules per bead, assuming that all thrombin molecules were bound, and that they were uniformly distributed across

all the beads. The calculations of the number of thrombin molecules per bead, and the percentage of the available binding sites that are occupied per bead, for the bead concentrations used in Figures 4.4-4.6, are shown in Table 4.1 below.

Initial Bead Conc. (μg/mL)	LOD (pM)	Top of Dynamic Range (est) (pM)	29-mer Beads per Droplet	Thrombin Molecules per Bead at LOD	Percent of Binding Sites per Bead Occupied at LOD	Thrombin Molecules per Bead at Top of Dynamic Range (est)	Percent of Binding Sites per Bead Occupied at Top of Dynamic Range (est)
7	0.08	10	306	143	0.060%	17900	7.44%
22	0.195	30	962	111	0.046%	17000	7.10%
70	1.06	100	3060	189	0.079%	17900	7.44%
220	5.3	300	9620	301	0.125%	17000	7.10%

Table 4.1—The average number of thrombin molecules and percentage of binding sites occupied per bead at the limit of detection (LOD), the point at which the effects of the thrombin molecules on the shape of the bead aggregate are first detectable by magnetorotation, and at the top of the dynamic range, the point at which the dose-response curve plateaus, and any additional thrombin molecules will not have a significant effect on the shape of the bead aggregate. The LOD values correspond with those shown in Figure 4.4b. The top of the dynamic range is estimated from the curve. The initial bead concentration refers to the initial concentration of both the 15-mer and 29-mer beads before they are added to the thrombin solution. The beads per droplet, thrombin molecules per bead and percent binding sites occupied represent average expected values based on the parameters provided above.

Additionally, assuming that the streptavidin-aptamer-thrombin-aptamer-streptavidin binding complex has a total length of around 20 nm, steric hindrances would only allow a fairly small amount of the surface area of each bead to participate in binding. Assuming that two beads bind “pole-to-pole” only the surface of the bead within a 10 nm of the pole height would be capable of participating in the binding event. By using the equation for calculating the partial surface area of a sphere, $A = \iint r^2 \sin\theta d\theta d\phi$,

only about 1% of the bead's surface area can participate in binding to another bead. Given that, at the LOD, each bead likely has between 100-300 thrombin molecules on its surface, and only 1% of the bead's surface participates in the binding event, it is likely that only a few thrombin molecules are needed for binding two beads together.

Calculation of Energies of Bond Strengths and Rupture Forces

The energy of the bond between thrombin and the 15-mer aptamer, which is the weaker of the two aptamers, has been reported as 44.5 k_BT. [56] For the effects of gravity on two beads bound together, it was assumed that one bead would be held stationary while the second would be free to rotate around it due to gravity. Using the equation for work due to rotational torque, $W = \mathbf{r} \times \mathbf{F}\phi$, where **r** is the vector of the lever arm (in this case with the magnitude of one bead diameter, 1 μm), **F** is the force of gravity on the bead, and φ is the angle through which the work occurs (assuming a full 180 degree rotation), the work performed comes out to about 7.6 k_BT, which is less than the bond energy of 20 k_BT. For the case of an elastic collision, a falling bead has a maximum velocity of $v = \frac{mg}{6\pi\eta r}$, where *m* is the bead mass, *g* is the gravitational acceleration, η is the solution viscosity and *r* is the bead radius. With a kinetic energy of $E = \frac{mv^2}{2}$, one bead has a kinetic energy << 1 k_BT.

Fractal Dimension and Lacunarity Dose Response Curves

Figure 4.6 shows the fractal dimension and lacunarity (the measure of gappiness of a structure) of the bead assemblies for three different bead concentrations, 22 μg/mL,

70 μg/mL and 220 μg/mL, (7 μg/mL assemblies were too small to accurately quantify using this method) as measured by the ImageJ plugin FracLac. [50] The fractal dimension of a solid two-dimensional object is 2, and the fractal dimension of a diffusion-limited aggregate is approximately 1.71. [51] Figure 4.6a suggests that at high thrombin concentrations, the bead assemblies might have a structure similar to that of diffusion limited aggregates. Figure 4.6c shows the relationship between fractal dimension, lacunarity, and the normalized rotational period, for the 22 μg/mL bead assemblies.

There are two primary advantages that the rotational period analysis has over image analysis (fractal dimension and lacunarity) as a method for measuring the protein concentration. The first is that assemblies from the lowest bead concentration (7 μg/mL) could not be accurately measured by image analysis, because the relatively small number of beads in the assembly results in an unacceptably high level of fluctuations/noise in the measured values, which is not the case with the rotational period measurements. Therefore, analysis by the rotational period method allows for greater sensitivity and dynamic range. The second advantage is that the rotational period can be measured using just a portable laser-and-photodiode setup (discussed below), in contrast to the microscope required for image analysis, which would allow for a portable, rugged and inexpensive instrument for decentralized ("in the field") measurement locations. Additionally, it should be noted that magnetorotation is still required for performing image analysis. The rotating magnetic field is needed to pack the beads into the dense hexagonal configuration, without which the fractal dimension and lacunarity cannot be accurately measured at low protein concentration (without the field, the beads will diffuse

away from the center of the assembly via Brownian motion, creating the appearance of higher lacunarity and lower fractal dimension).

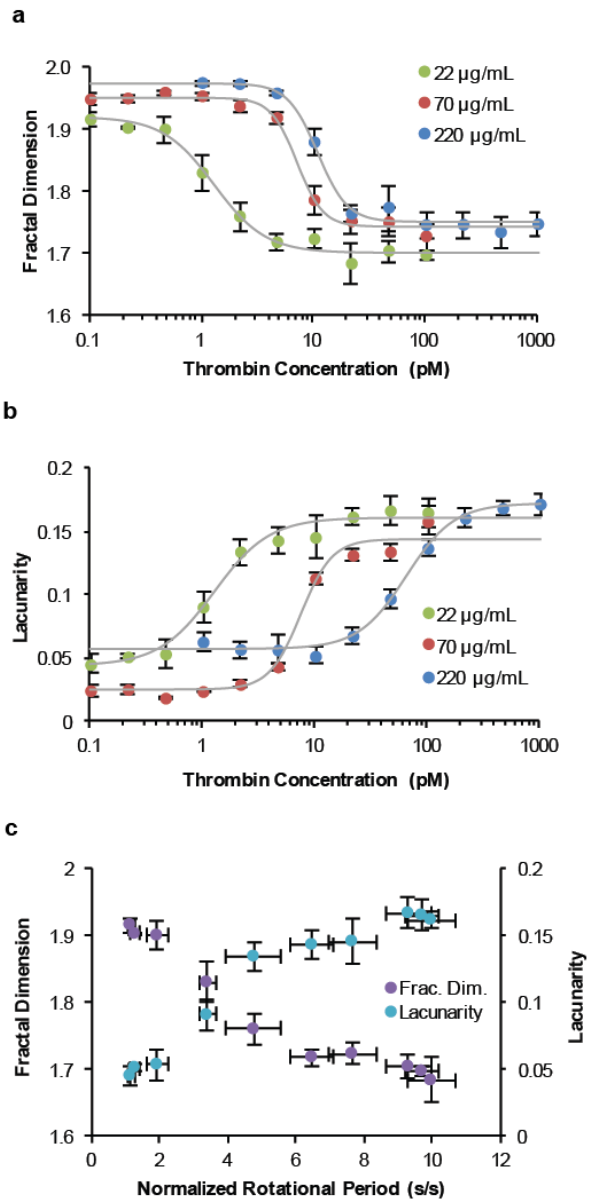

Figure 4.6—(a) Fractal dimension, and (b) Lacunarity of bead assemblies. Three bead concentrations are shown, 22 µg/mL, 70 µg/mL and 220 µg/mL. For both plots, each point represents an average over ten bead assemblies; error bars are ±SD. Curve is the logistic Hill equation [57] fit to the data. (c) The relationship between rotational period, fractal dimension and lacunarity. The data shown are for the 22 µg/mL bead concentration.

The data in Figure 4.6b suggest that among image analysis methods, for the data presented here, the fractal dimension appears to provide more useful information than the lacunarity. We included the lacunarity to show that it could also be used as a method for measuring protein concentration through bead assembly. We examined additional image analysis methods; including measuring the physical size of the assembly via the radius of gyration of the assembly and measuring the angles between adjacent nearest-neighbor beads, (see Appendix B) but those methods did not provide as much information as fractal dimension and lacunarity.

Laser and Photodiode Setup

In order to facilitate the performance of BAM without the use of a microscope, it would be necessary to develop a simple, inexpensive and portable detection apparatus. To this effect, we designed a laser-and-photodiode detection apparatus from inexpensive, readily available laboratory components, as shown in Figure 4.7a. When a low power (20 mW, 650 nm) laser diode is shined on a droplet containing a bead assembly, the droplet acts as a lens, focusing the beam through its center, where the assembly lies. This creates a projection of the bead assembly that is magnified by beam spreading caused by the droplet focusing (in practice, a bead assembly that is approximately 100 μm in diameter is magnified to approximately 4-5 cm over a distance of approximately 20 cm). This rotation of the projection of the bead assembly is captured by a 3-by-3 array of photodiodes located underneath the droplet. The signals from each of the photodiodes are recorded in LabVIEW, and analyzed with a Fourier transform to determine the rotational period of the assembly (a screenshot of this program is shown in Figure 4.8 below).

Having multiple redundant signals (each of the nine diodes calculates the rotational period independently, creating a set of redundant signals) helps to increase confidence in the output.

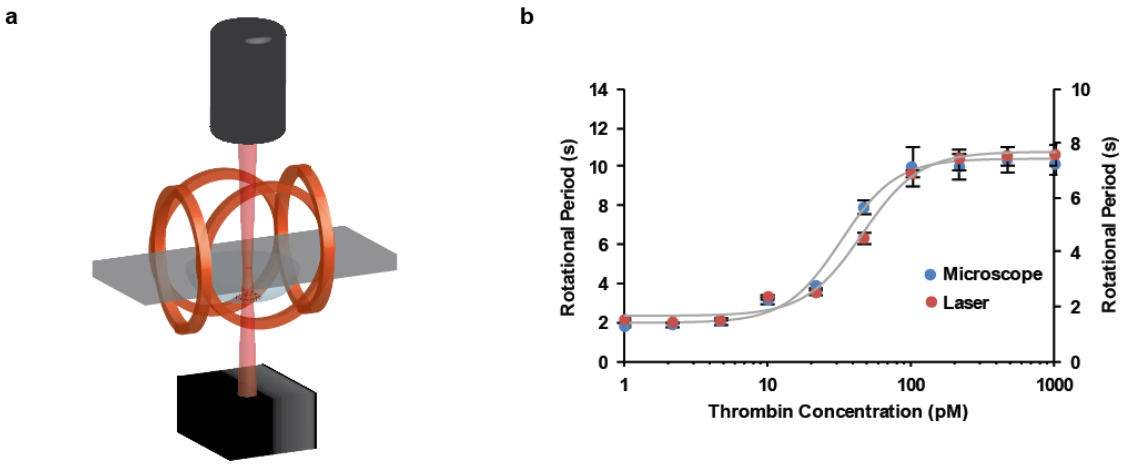

Figure 4.7—(a) A schematic of the laser-and-photodiode setup. A low-power red laser is aimed at the center of the droplet holding the self-assembled aggregate. The droplet optically focuses the beam through the aggregate, creating a projection of the rotating aggregate onto an array of photodiodes. The periodic signal captured by the photodiodes is analyzed by a computer program, from which it calculates the rotational period using a Fourier transform. (b) Rotational period of bead assemblies as captured by the microscope (blue, left axis) and the laser-photodiode setup (red, right axis). Each point represents the mean ± SD of 10 assemblies. Both data sets were fit with the logistic Hill equation.

The performance of the laser-and-photodiode apparatus was validated by measuring the magnetorotation of a series of 220 μg/mL bead assemblies on the microscope and then on the laser-and-photodiode apparatus, as shown in Figure 4.7b. The difference in the relative values of the rotational periods between the two systems is due to differences in the strengths of the magnetic field (4 mT on the microscope, 4.7 mT on the laser-photodiode setup) on the two setups. However, the shapes of the two curves

closely follow each other, suggesting that a simple, inexpensive laser-and-photodiode system is capable of measuring the magnetorotation, and therefore the thrombin concentration, of magnetic bead assemblies without the use of a microscope.

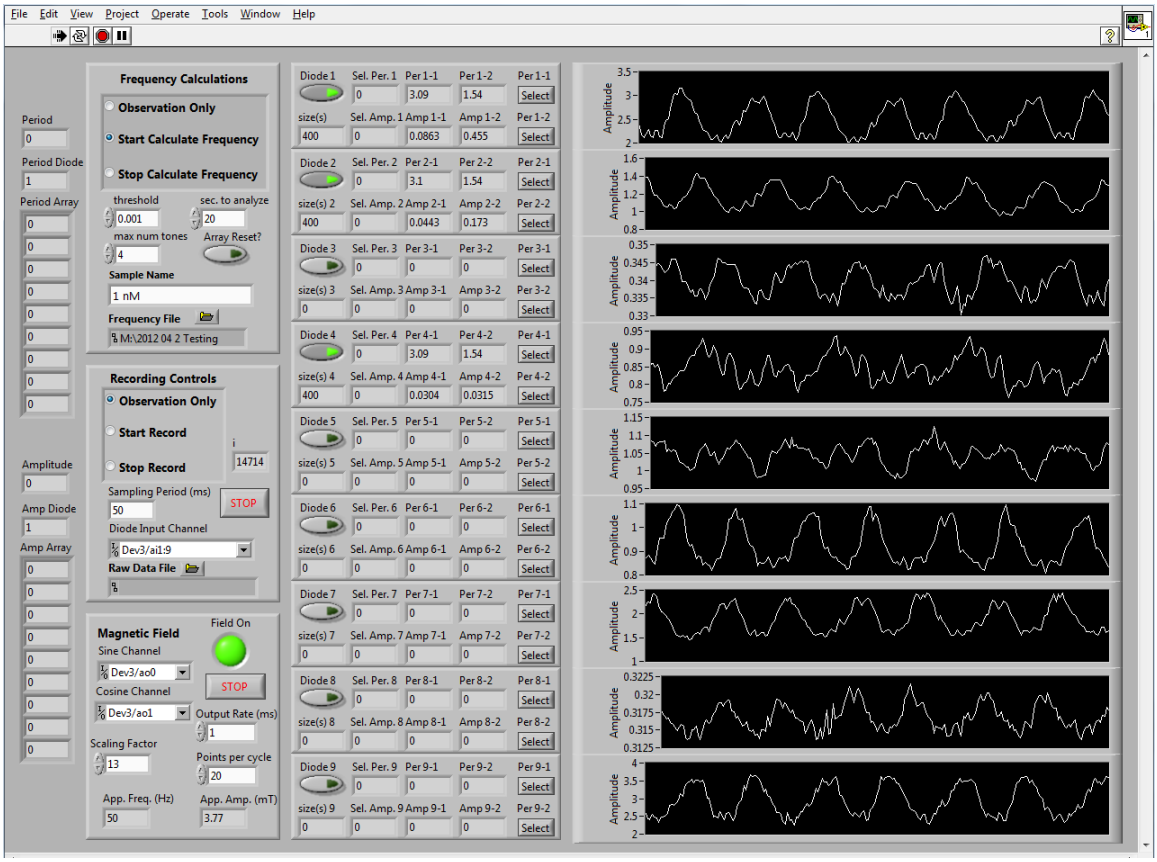

Figure 4.8—Above is a screenshot of the LabVIEW program to collect and analyze the data captured by the photodiodes of the rotating projecting of the bead assembly. Traces from all nine diodes are shown (each trace is 10 seconds of data). Due to limitations of the computer that was used to perform the experiment, only three Fourier transforms could be performed simultaneously in real-time without slowing down the data collection process. In this screenshot, diodes 1, 2 and 4 are selected, each outputting a rotational period of 3.1 seconds (the second harmonic of the signal is 1.54 seconds).

Conclusion

This chapter introduces Bead Assembly Magnetorotation as a viable signal transduction method for measuring the concentration of a protein in solution through two different methods, magnetorotation and fractal analysis. The 80 fM LOD of this system for the protein thrombin is very competitive with existing detection methods. The simple laser-and-photodiode portable detection setup represents a potential for the development of BAM into a point-of-care detection system. In future work, we intend to demonstrate the performance of BAM in serum with more clinically relevant protein targets.

Acknowledgments

I would like to thank Patrick Commiskey and Nicholas Shah for their tremendous assistance in conducting this research. This research was partially supported by the Department of Homeland Security (DHS) Scholarship and Fellowship program, administered by the Oak Ridge Institute for Science and Education (ORISE) through an interagency agreement between the U.S. Department of Energy and DHS, under DOE Contract Number DE-AC05-06OR23100 (A.H.). Additional support came from NIH Grant R21 CA160157 (R.K.).

References

1. Pamme, N. Magnetism and microfluidics. *Lab on a Chip*, 2006. **6**(1): p. 24-38.
2. Gijs, M.A.M., F. Lacharme, and U. Lehmann. Microfluidic Applications of Magnetic Particles for Biological Analysis and Catalysis. *Chemical Reviews*, 2010. **110**(3): p. 1518-1563.
3. Osterfeld, S.J., H. Yu, R.S. Gaster, S. Caramuta, et al. Multiplex protein assays based on real-time magnetic nanotag sensing. *Proceedings of the National Academy of Sciences of the United States of America*, 2008. **105**(52): p. 20637-20640.
4. Wang, S.X. and L. Guanxiong. Advances in Giant Magnetoresistance Biosensors With Magnetic Nanoparticle Tags: Review and Outlook. *Magnetics, IEEE Transactions on*, 2008. **44**(7): p. 1687-1702.
5. Tamanaha, C.R., S.P. Mulvaney, J.C. Rife, and L.J. Whitman. Magnetic labeling, detection, and system integration. *Biosensors & Bioelectronics*, 2008. **24**(1): p. 1-13.
6. Lee, H., E. Sun, D. Ham, and R. Weissleder. Chip-NMR biosensor for detection and molecular analysis of cells. *Nature Medicine*, 2008. **14**(8): p. 869-874.
7. Chung, S.H., A. Hoffmann, S.D. Bader, C. Liu, et al. Biological sensors based on Brownian relaxation of magnetic nanoparticles. *Applied Physics Letters*, 2004. **85**(14): p. 2971-2973.
8. Besse, P.-A., G. Boero, M. Demierre, V. Pott, et al. Detection of a single magnetic microbead using a miniaturized silicon Hall sensor. *Applied Physics Letters*, 2002. **80**(22): p. 4199-4201.
9. Sandhu, A., H. Handa, and M. Abe. Synthesis and applications of magnetic nanoparticles for biorecognition and point of care medical diagnostics. *Nanotechnology*, 2010. **21**(44): p. 442001.
10. Patolsky, F., Y. Weizmann, E. Katz, and I. Willner. Magnetically Amplified DNA Assays (MADA): Sensing of Viral DNA and Single-Base Mismatches by Using Nucleic Acid Modified Magnetic Particles. *Angewandte Chemie International Edition*, 2003. **42**(21): p. 2372-2376.
11. Willner, I. and E. Katz. Magnetic Control of Electrocatalytic and Bioelectrocatalytic Processes. *Angewandte Chemie International Edition*, 2003. **42**(38): p. 4576-4588.
12. Ranzoni, A., J.J.H.B. Schleipen, L.J. van Ijzendoorn, and M.W.J. Prins. Frequency-Selective Rotation of Two-Particle Nanoactuators for Rapid and Sensitive Detection of Biomolecules. *Nano Letters*, 2011. **11**(5): p. 2017-2022.
13. Petkus, M.M., M. McLauchlin, A.K. Vuppu, L. Rios, et al. Detection of FITC-cortisol via modulated supraparticle lighthouses. *Analytical Chemistry*, 2006. **78**(5): p. 1405-1411.

14. Hecht, A., P. Kinnunen, B. McNaughton, and R. Kopelman. Label-acquired magnetorotation for biosensing: An asynchronous rotation assay. *Journal of Magnetism and Magnetic Materials*, 2011. **323**(3-4): p. 272-278.

15. Hecht, A., A.A. Kumar, and R. Kopelman. Label-Acquired Magnetorotation As a Signal Transduction Method for Protein Detection: Aptamer-Based Detection of Thrombin. *Analytical Chemistry*, 2011. **83**(18): p. 7123-7128.

16. Kinnunen, P., I. Sinn, B.H. McNaughton, D.W. Newton, et al. Monitoring the growth and drug susceptibility of individual bacteria using asynchronous magnetic bead rotation sensors. *Biosensors and Bioelectronics*, 2011. **26**(5): p. 2751-2755.

17. McNaughton, B.H., R.R. Agayan, R. Clarke, R.G. Smith, et al. Single bacterial cell detection with nonlinear rotational frequency shifts of driven magnetic microspheres. *Applied Physics Letters*, 2007. **91**(22): p. 224105.

18. Sinn, I., T. Albertson, P. Kinnunen, D.N. Breslauer, et al. Asynchronous Magnetic Bead Rotation Microviscometer for Rapid, Sensitive, and Label-Free Studies of Bacterial Growth and Drug Sensitivity. *Analytical Chemistry*, 2012. **84**(12): p. 5250-5256.

19. Elbez, R., B.H. McNaughton, L. Patel, K.J. Pienta, et al. Nanoparticle Induced Cell Magneto-Rotation: Monitoring Morphology, Stress and Drug Sensitivity of a Suspended Single Cancer Cell. *Plos One*, 2011. **6**(12): p. e28475.

20. Fonnum, G., C. Johansson, A. Molteberg, S. Morup, et al. Characterisation of Dynabeads (R) by magnetization measurements and Mossbauer spectroscopy. *Journal of Magnetism and Magnetic Materials*, 2005. **293**(1): p. 41-47.

21. Connolly, J. and T.G. St Pierre. Proposed biosensors based on time-dependent properties of magnetic fluids. *Journal of Magnetism and Magnetic Materials*, 2001. **225**(1-2): p. 156-160.

22. Fannin, P.C., L. Cohen-Tannoudji, E. Bertrand, A.T. Giannitsis, et al. Investigation of the complex susceptibility of magnetic beads containing maghemite nanoparticles. *Journal of Magnetism and Magnetic Materials*, 2006. **303**(1): p. 147-152.

23. Janssen, X.J.A., A.J. Schellekens, K. van Ommering, L.J. van Ijzendoorn, et al. Controlled torque on superparamagnetic beads for functional biosensors. *Biosensors & Bioelectronics*, 2009. **24**(7): p. 1937-1941.

24. Biancaniello, P.L., A.J. Kim, and J.C. Crocker. Colloidal Interactions and Self-Assembly Using DNA Hybridization. *Physical Review Letters*, 2005. **94**(5): p. 058302.

25. Park, S.Y., A.K.R. Lytton-Jean, B. Lee, S. Weigand, et al. DNA-programmable nanoparticle crystallization. *Nature*, 2008. **451**(7178): p. 553-556.

26. Nykypanchuk, D., M.M. Maye, D. van der Lelie, and O. Gang. DNA-guided crystallization of colloidal nanoparticles. *Nature*, 2008. **451**(7178): p. 549-552.

27. Bock, L.C., L.C. Griffin, J.A. Latham, E.H. Vermaas, et al. Selection of single-stranded DNA molecules that bind and inhibit human thrombin. *Nature*, 1992. **355**(6360): p. 564-566.

28. Tasset, D.M., M.F. Kubik, and W. Steiner. Oligonucleotide inhibitors of human thrombin that bind distinct epitopes. *Journal of Molecular Biology*, 1997. **272**(5): p. 688-698.

29. Pavlov, V., Y. Xiao, B. Shlyahovsky, and I. Willner. Aptamer-Functionalized Au Nanoparticles for the Amplified Optical Detection of Thrombin. *Journal of the American Chemical Society*, 2004. **126**(38): p. 11768-11769.

30. Huang, C.-C., Z. Cao, H.-T. Chang, and W. Tan. Protein−Protein Interaction Studies Based on Molecular Aptamers by Affinity Capillary Electrophoresis. *Analytical Chemistry*, 2004. **76**(23): p. 6973-6981.

31. Hianik, T., V. Ostatná, Z. Zajacová, E. Stoikova, et al. Detection of aptamer-protein interactions using QCM and electrochemical indicator methods. *Bioorganic & Medicinal Chemistry Letters*, 2005. **15**(2): p. 291-295.

32. Liu, X., R. Aizen, R. Freeman, O. Yehezkeli, et al. Multiplexed aptasensors and amplified DNA sensors using functionalized graphene oxide: application for logic gate operations. *ACS Nano*, 2012. **6**(4): p. 3553-63.

33. Radi, A.-E., J.L. Acero Sánchez, E. Baldrich, and C.K. O'Sullivan. Reagentless, Reusable, Ultrasensitive Electrochemical Molecular Beacon Aptasensor. *Journal of the American Chemical Society*, 2005. **128**(1): p. 117-124.

34. Centi, S., S. Tombelli, M. Minunni, and M. Mascini. Aptamer-Based Detection of Plasma Proteins by an Electrochemical Assay Coupled to Magnetic Beads. *Analytical Chemistry*, 2007. **79**(4): p. 1466-1473.

35. Kim, K.S., H.-S. Lee, J.-A. Yang, M.-H. Jo, et al. The fabrication, characterization and application of aptamer-functionalized Si-nanowire FET biosensors. *Nanotechnology*, 2009. **20**(23): p. 235501.

36. Tennico, Y.H., D. Hutanu, M.T. Koesdjojo, C.M. Bartel, et al. On-Chip Aptamer-Based Sandwich Assay for Thrombin Detection Employing Magnetic Beads and Quantum Dots. *Analytical Chemistry*, 2010. **82**(13): p. 5591-5597.

37. Cai, H., T.M.-H. Lee, and I.M. Hsing. Label-free protein recognition using an aptamer-based impedance measurement assay. *Sensors and Actuators B: Chemical*, 2006. **114**(1): p. 433-437.

38. Zhou, W.J., A.R. Halpern, T.H. Seefeld, and R.M. Corn. Near infrared surface plasmon resonance phase imaging and nanoparticle-enhanced surface plasmon resonance phase imaging for ultrasensitive protein and DNA biosensing with oligonucleotide and aptamer microarrays. *Analytical Chemistry*, 2012. **84**(1): p. 440-5.

39. Cho, H., B.R. Baker, S. Wachsmann-Hogiu, C.V. Pagba, et al. Aptamer-Based SERRS Sensor for Thrombin Detection. *Nano Letters*, 2008. **8**(12): p. 4386-4390.

40. Song, M., Y. Zhang, T. Li, Z. Wang, et al. Highly sensitive detection of human thrombin in serum by affinity capillary electrophoresis/laser-induced fluorescence polarization using aptamers as probes. *Journal of Chromatography A*, 2009. **1216**(5): p. 873-878.

41. Hu, J., T. Wang, J. Kim, C. Shannon, et al. Quantitation of Femtomolar Protein Levels via Direct Readout with the Electrochemical Proximity Assay. *Journal of the American Chemical Society*, 2012. **134**(16): p. 7066-7072.

42. An, T., K.S. Kim, S.K. Hahn, and G. Lim. Real-time, step-wise, electrical detection of protein molecules using dielectrophoretically aligned SWNT-film FET aptasensors. *Lab on a Chip*, 2010. **10**(16): p. 2052-2056.

43. Bai, L., R. Yuan, Y. Chai, Y. Zhuo, et al. Simultaneous electrochemical detection of multiple analytes based on dual signal amplification of single-walled carbon nanotubes and multi-labeled graphene sheets. *Biomaterials*, 2012. **33**(4): p. 1090-1096.

44. Ho, H.-A. and M. Leclerc. Optical Sensors Based on Hybrid Aptamer/Conjugated Polymer Complexes. *Journal of the American Chemical Society*, 2004. **126**(5): p. 1384-1387.

45. Li, Y., H.J. Lee, and R.M. Corn. Detection of Protein Biomarkers Using RNA Aptamer Microarrays and Enzymatically Amplified Surface Plasmon Resonance Imaging. *Analytical Chemistry*, 2007. **79**(3): p. 1082-1088.

46. Hansen, J.A., J. Wang, A.-N. Kawde, Y. Xiang, et al. Quantum-Dot/Aptamer-Based Ultrasensitive Multi-Analyte Electrochemical Biosensor. *Journal of the American Chemical Society*, 2006. **128**(7): p. 2228-2229.

47. Rahman, M.A., J.I. Son, M.S. Won, and Y.B. Shim. Gold nanoparticles doped conducting polymer nanorod electrodes: ferrocene catalyzed aptamer-based thrombin immunosensor. *Analytical Chemistry*, 2009. **81**(16): p. 6604-11.

48. Zhang, X., B. Qi, Y. Li, and S. Zhang. Amplified electrochemical aptasensor for thrombin based on bio-barcode method. *Biosensors & Bioelectronics*, 2009. **25**(1): p. 259-62.

49. Milne, G., *Optical Sorting and Manipulation of Microscopic Particles*. 2007, University of St. Andrews.

50. Karperien, A., *FracLac for Image J, version 2.5*. 1999-2012.

51. Witten, T.A., Jr. and L.M. Sander. Diffusion-Limited Aggregation, a Kinetic Critical Phenomenon. *Physical Review Letters*, 1981. **47**(19): p. 1400-1403.

52. Long, G.L. and J.D. Winefordner. Limit of detection. A closer look at the IUPAC definition. *Analytical Chemistry*, 1983. **55**(7): p. 712A-724A.

53. Baud, M., *Data Analysis, Mathematical Modeling*, in *Methods of Immunological Analysis*, R. Masseyeff, Editor. 1993, VCH Publishers, Inc.: New York, NY. p. 656-671.

54. Li, Y., L. Guo, F. Zhang, J. Tang, et al. High-sensitive determination of human a-thrombin by its 29-mer aptamer in affinity probe capillary electrophoresis. *Electrophoresis*, 2008. **29**: p. 2570-2577.

55. Invitrogen. 2012 7/10/12]; Available from: http://products.invitrogen.com/ivgn/product/65601.

56. Pagano, B., L. Martino, A. Randazzo, and C. Giancola. Stability and Binding Properties of a Modified Thrombin Binding Aptamer. *Biophysical Journal*, 2008. **94**(2): p. 562-569.

57. Hecht, A.H., G.J. Sommer, R.H. Durland, X. Yang, et al. Aptamers as Affinity Reagents in an Integrated Electrophoretic Lab-on-a-Chip Platform. *Analytical Chemistry*, 2010. **82**(21): p. 8813-8820.

Chapter 5

The Performance of BAM in Serum with the Thrombin Aptamers

Introduction

As detailed in the previous chapter, in buffer, BAM showed a very low limit of detection (LOD) (80 fM), a short analysis time, and the ability to be performed on a microscope-free laser-and-photodiode setup. However, in order for BAM to become a clinically relevant technology, there is one final step that must be attained, the performance of BAM in serum. The performance of a diagnostic assay in serum is challenging because of nonspecific binding between the serum proteins and the affinity molecules and the surfaces of the diagnostic assay. [1] Given the much greater concentration of serum proteins (on the order of millimolar) relative to the target protein (on the order of picomolar or lower), nonspecific interference from serum proteins can result in substantially degraded system performance.

One of the most popular molecules used to mitigate nonspecific binding from serum proteins is poly(ethylene glycol) (PEG). [1, 2] PEG is a fairly simple molecule:

$$HO—(CH_2CH_2O)_n—CH_2CH_2OH$$

with *n* representing the number of repeats of the ethylene glycol subunit. PEG is an incredibly hygroscopic molecule, capable of adsorbing several times its own weight in water molecules via hydrogen bonding. [3] For these reasons, PEG has been a very

popular molecule for use in preventing biofouling on the surfaces of biological devices. [4-6] In the absence of any molecule used to mitigate nonspecific serum interactions with the beads, large amounts of these nonspecific interactions will significantly diminish the system. This chapter will discuss attempts to use PEG to mitigate the nonspecific serum interactions, to allow BAM to be performed in serum.

Materials and Methods

The experiments in this chapter used heterobifunctional PEG, with one end of the molecule functionalized with biotin, and the other end functionalized with maleimide, as shown in Figure 5.1 below. (The use of homobiofunctional PEG results in crosslinking of the beads.) This will allow for one end of the molecule to be attached to the beads via biotin-streptavidin conjugation, and the other end of the molecule to be attached to the aptamer via maleimide-thiol conjugation. Two different molecular weight PEG sizes were used: 2000 Da (2K) and 10,000 Da (10K), purchased from Creative PEG Works (Winston-Salem, NC).

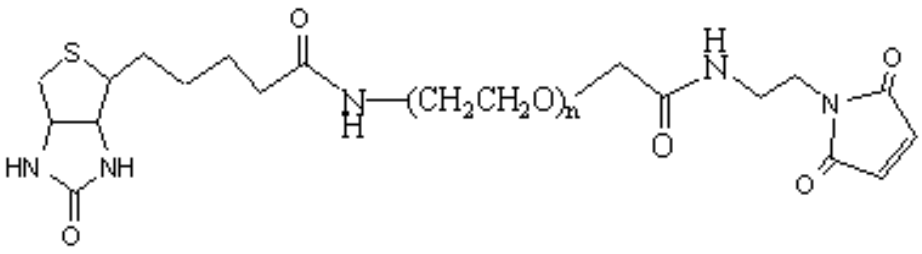

Figure 5.1—Schematic illustration of the biotin-PEG-maleimide heterobifunctional PEG used in this experiment. [7]

The following procedure was adapted from *Bioconjugate Techniques*. [8] A 10 μL aliquot of Invitrogen Dynal MyOne Streptavidin T1 beads (10 mg/mL) was taken and

washed three times and resuspended in 100 μL of a 20 mM Na_2HPO_4, 150 mM NaCl, pH=7.4 buffer. The binding capacity of this aliquot of beads is 40 pmol. A ten-fold excess of PEG (4 μg for the 10K PEG, 0.8 μg for the 2K PEG) was dissolved in buffer at 5 mg/mL, and 1 μL of solution was added to the beads solution. The solution was then placed on the end-over-end rotator for 30 minutes.

Dithiolated aptamers (the 15-mer and 29-mer) both with and without a 20-base 5' polyT tail were purchased from IDT (Coralville, IA). The dithiol groups were reduced to thiol groups using tris(2-carboxyethyl)phosphine (TCEP) by the following procedure. A boiling water bath was prepared. The TCEP was diluted from the 0.5 M stock to 200 μM with buffer. A 2 μL aliquot of each thiolated aptamer (50 nmol/mL) was mixed with 5 μL of 200 μM TCEP, covered with parafilm, and then submerged in the boiling water bath for 5 minutes. In the meantime, the beads which had been incubated with the PEG were washed with buffer, resuspended in 100 μL of buffer and split into two 50 μL aliquots (one for each aptamer). The aptamer solution was then quickly transferred to the beads, because the thiol and maleimide groups are highly reactive. The solutions were then incubated with end-over-end rotation for 2 hours, after which they were washed again and resuspended at their final desired concentration.

Off-the-clot human serum was purchased from PAA Laboratories (Dartmouth, MA). Human α-thrombin was purchased from Haematologic Technologies (Essex Junction, VT). Various concentrations of beads, thrombin, and serum were prepared, and then transferred to hanging droplets. Hanging droplets were prepared on a Teflon-coated slide, with a greased O-ring in the middle (for sealing). Sixteen 1 μL droplets of thrombin-bead solution were placed on the 1.5-mm exposed glass spots on the slide in a

4-by-4 array. The other side of the O-ring was greased, and a clear glass slide was placed on top, creating a seal around the droplets (this was to prevent evaporation as well as to minimize air currents disrupting the droplets). The slides were then flipped over, so that the droplets hung down from the Teflon-coated slide. The slides were allowed to sit for 30 minutes, during which the beads fell through the solution, under the influence of gravity (bead density = 1.9 g/cm^3). As the beads collected in the tip of the droplet, if they encountered a thrombin molecule, the beads could bind to each other. In the absence of thrombin molecules, the beads collected in a tight cluster in the center of the droplet. The slides were then placed in the rotating magnetic field for magnetorotation and further analysis.

Results and Discussion

Experiments were performed to examine the effects of the PEG coating on the formation of bead clusters without the presence of thrombin. Three groups of beads were prepared: beads coated with 10K PEG, but without aptamers; beads coated with aptamers, but without PEG (effectively the control group); and beads coated with both 10K PEG and aptamers. No thrombin was included. Five different dilutions of serum were prepared: 10% serum, 1% serum, 0.1% serum, 0.01% serum, and a buffer control. Bead solutions with a concentration of 70 μg/mL were prepared with each of the serum solutions. A series of images from these samples are shown in Figure 5.2 below.

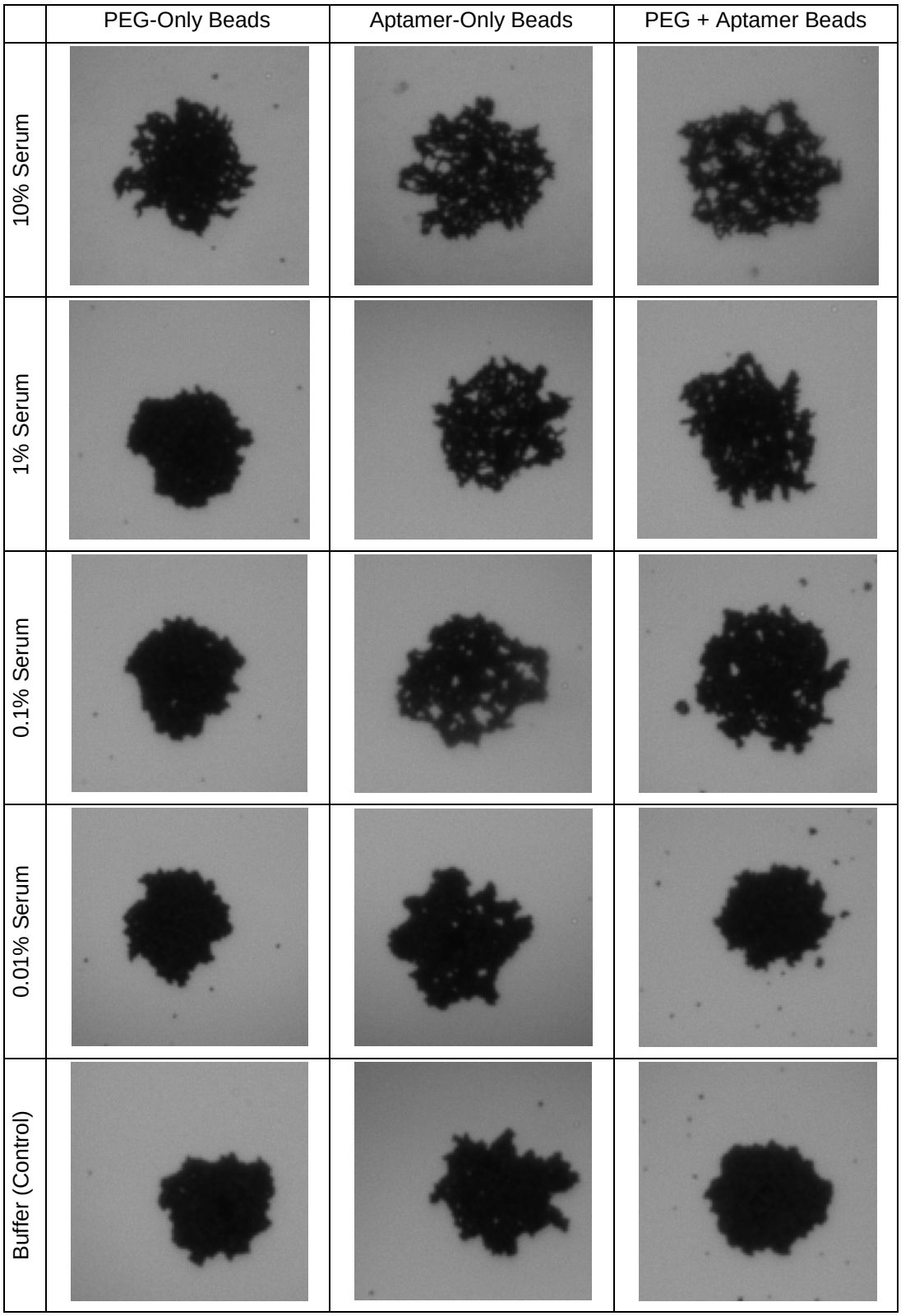

Figure 5.2—A series of images showing magnetic bead assemblies prepared with 10K PEG-coated, aptamer-coated, and 10K PEG+aptamer-coated beads, in 10%, 1%, 0.1%, 0.01% serum and a buffer control.

Since there was no thrombin present in these samples, the expectation was to see a tight hexagonally-packed cluster in each image; any deviation from this would indicate the presence of nonspecific binding. In the first column, the PEG-only beads, tightly-packed clusters can be found in the 1%, 0.1%, 0.01% serum and control (0%) samples. In the 10% serum sample, however, there does appear to be some nonspecific binding. As an additional test to confirm these observations, which were produced under a rotating magnetic field, the field was turned off, and then the cluster was monitored for the presence of Brownian motion of the beads diffusing away from the center of cluster. In the absence of a molecule to bind the beads together, the beads begin to slowly diffuse away from the center of the cluster due to Brownian forces. In the case of the 10% serum, no such diffusion was observed, confirming the fact that the serum was nonspecifically binding to the surface of the bead.

In the case of the aptamer-only beads, nonspecific binding was observed in all serum samples. The buffer control showed no nonspecific binding. In the case of the beads coated with both PEG and aptamer, nonspecific binding was observed in all of the serum solutions except for the 0.01% serum solution, as well as for the control. This was confirmed by checking each sample for the presence of Brownian diffusion of the beads after turning off the magnetic field.

This experiment revealed several interesting facts about the nonspecific binding of serum proteins. The serum proteins appear to bind to both the bead as well as to the aptamer itself. The binding of serum proteins to the bead can be mitigated by PEG, but the binding to the aptamer is much harder to mitigate. In the case of the PEG-only beads, the PEG effectively mitigated serum nonspecific binding at only a 100-fold dilution of

the serum (100% to 1%). With the addition of the aptamer to the PEG, another 100-fold dilution of the serum (1% to 0.01%) was needed again to mitigate the nonspecific binding effects of the serum. These results would suggest that in order to use these beads in serum, a 10,000-fold dilution of the sample would be necessary. The primary conclusions that can be drawn from this experiment are that, while PEG can mitigate nonspecific interactions, it does not provide a perfect solution, and that the nonspecific binding of the serum proteins to the aptamer is a significant factor that must be taken into consideration.

We next attempted to see if washing the beads could assist in mitigating the nonspecific binding of the serum proteins. Solutions of beads were prepared with four different concentrations of serum, 10%, 1%, 0.1% and 0.01%, as in the previous experiment, but before transferring the solution to inverted droplets, the solution of beads was washed two times by using a magnetic separator to pull the beads to the side of the tube, removing the remaining solution, and resuspending the beads in fresh buffer. The results from this experiment are shown in Figure 5.3 below. These results show that with 2 washing steps, there was no nonspecific binding in the 0.1% or 0.01% serum solutions, but that there was nonspecific binding in the 10% and 1% serum solutions. This represents a ten-fold improvement over the case with no washes, in which nonspecific binding was detected in all but the 0.01% serum solution. These results suggest that washing the beads two times by magnetic separation can remove some of the serum that binds nonspecifically to the beads.

The second step of this experiment, however, was to examine the effects of washing on the binding of thrombin to the beads. Solutions of bead assemblies were prepared with four different thrombin concentrations, 1 nM, 100 pM, 10 pM, and 1 pM ,

and a thrombin-free buffer control. One set of solutions was prepared in 0.01% serum, and the other was prepared in 0.1% serum. The samples prepared in 0.01% serum were not washed, and the samples prepared in the 0.1% serum were washed twice. Images are shown in Figure 5.4 below.

In the left-hand column of Figure 5.4, with the bead assemblies prepared with thrombin in 0.1% serum with two washes, there was no binding detected in any of the bead assemblies. This indicates that the magnetic washing step likely removes all of the bound thrombin. In the control sample, the 0.01% serum with no washing, binding can be detected in the 10 pM, 100pM and 1 nM samples. The results of this experiment show that in addition to removing nonspecifically bound serum proteins, washing of the beads before the formation of droplets likely removes any bound thrombin from the bead. Based on the data shown in Figures 5.2, 5.3 and 5.4, the conclusion was reached that, due to the effects of serum proteins binding to both the beads and the aptamer, a 10,000-fold dilution must be performed in order to perform BAM in serum with this aptamer/bead combination, and that washing the samples by magnetic separation would not be a useful step.

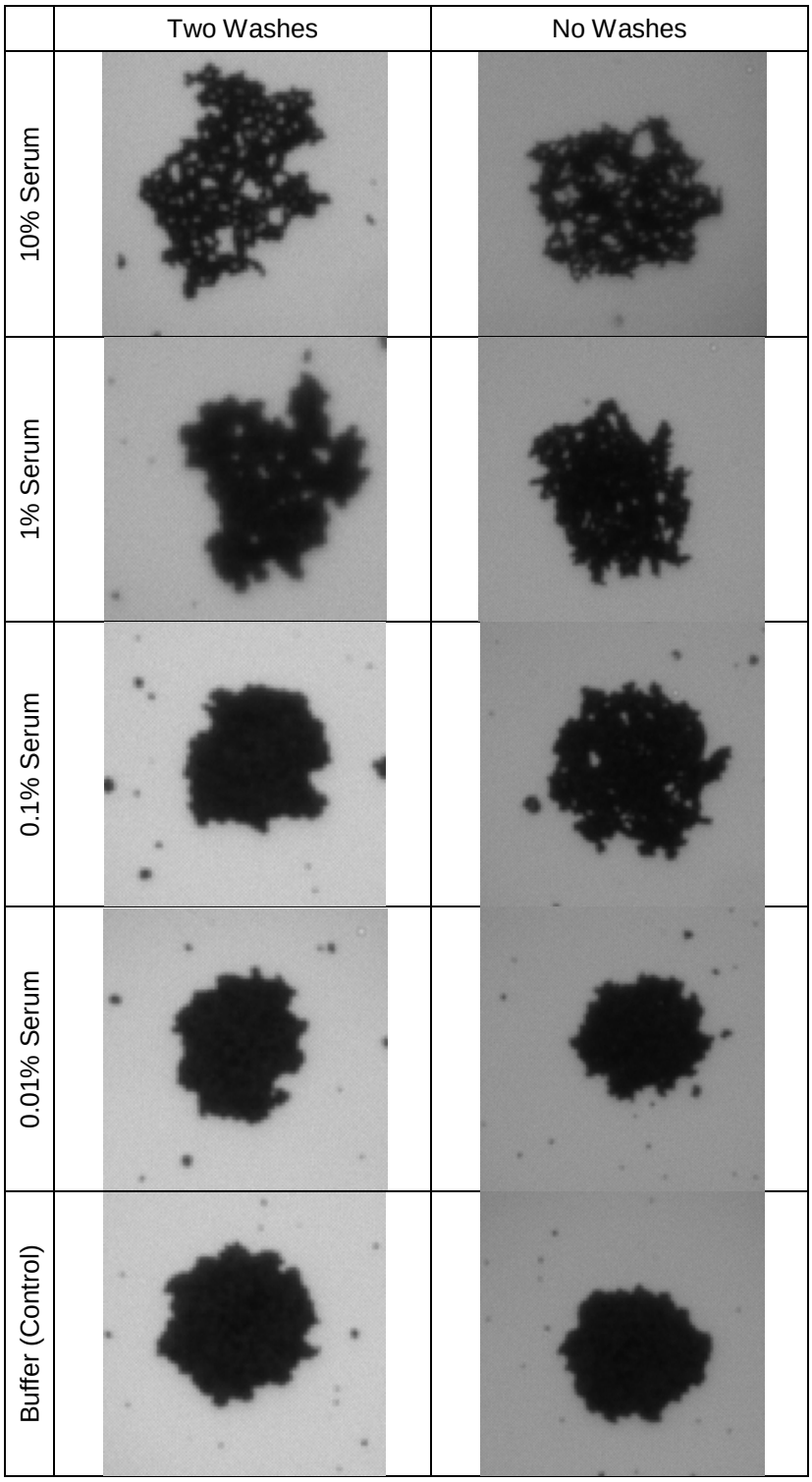

Figure 5.3—Beads coated with 10K PEG and the aptamers in different serum concentrations. The beads in the column on the left were washed twice by magnetic separation, and the beads in the column on the right were not washed.

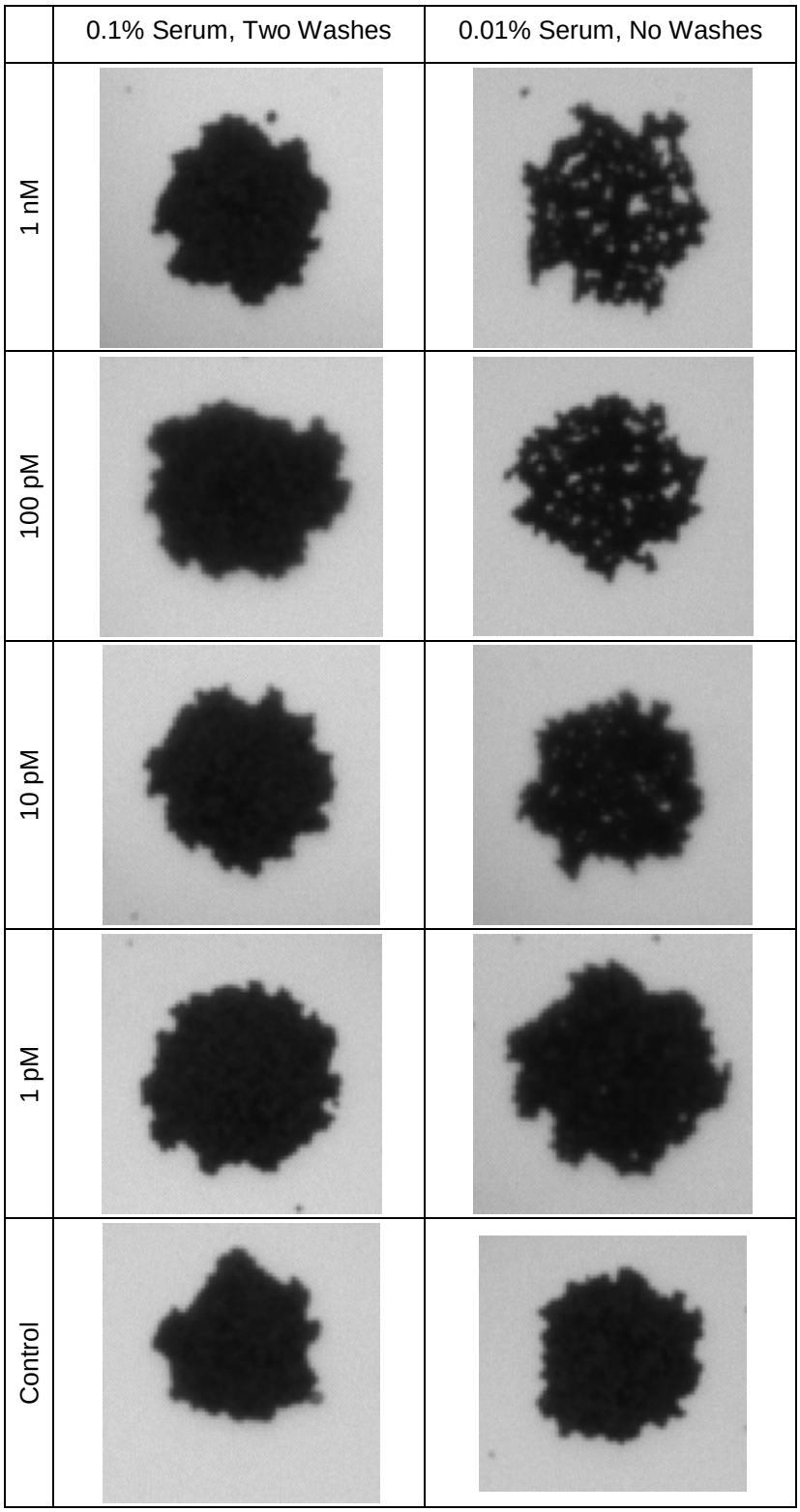

Figure 5.4—Examination of the effect of washing on formation of bead assemblies with thrombin. Thrombin concentration is listed on the left hand side. The left column is in 0.1% serum with 2 washes, the right column in 0.01% serum with no washes.

Dose-Response Curves in Serum

With these results in mind, we attempted to produce dose-response curves for BAM in serum, similar to those shown in the previous chapter. Two different bead concentrations were used, 22 μg/mL, and 70 μg/mL, corresponding with the two middle concentrations shown in Figure 4.3. In order to simulate a real clinical sample, various concentrations of thrombin were spiked into whole human serum, which was then diluted 10,000 times with buffer, as discussed earlier in this chapter. The inverted droplets were prepared as detailed in the Materials and Methods section of this chapter. For each sample, videos of ten bead assemblies were recorded and analyzed. The dose response curves for these two bead concentrations are shown in Figure 5.5 below. The thrombin concentrations shown in Figure 5.5 are based on the concentration of thrombin that was spiked into whole serum, which was then diluted 10,000 times with buffer (e.g., 1 nM in whole serum is equivalent to 100 fM in 0.01% serum). The magnetic driving field had an amplitude of 4 mT and a frequency of 50 Hz. The video capture program recorded videos at 40 frames per second.

These dose response curves demonstrate that, while BAM does produce a result in diluted serum, the quality of the data is not very good. The coefficient of variation of each data point is higher than in the buffer case, and the vertical resolution is significantly poorer. The LOD for the 22 μg/mL bead concentration is 16 nM, and the LOD for the 70 μg/mL bead concentration is 7.5 nM. Based on the results shown in Chapter 4, the LOD for the 22 μg/mL bead concentration would have been expected to be lower than that of the 70 μg/mL bead concentration. This discrepancy is likely due to the increased noise generated by the serum. Comparing the LODs to those reported for the same bead

concentrations in buffer in Chapter 4, for the 22 μg/mL bead concentration (0.195 pM LOD in buffer), the serum LOD is 82,000 times higher, and for the 70 μg/mL bead concentration (1.05 pM LOD in buffer), the serum LOD is 7,100 times higher. Based on the dilution required to mitigate the interference of serum on the beads, we would have expected the LOD to increase by a factor of 10,000.

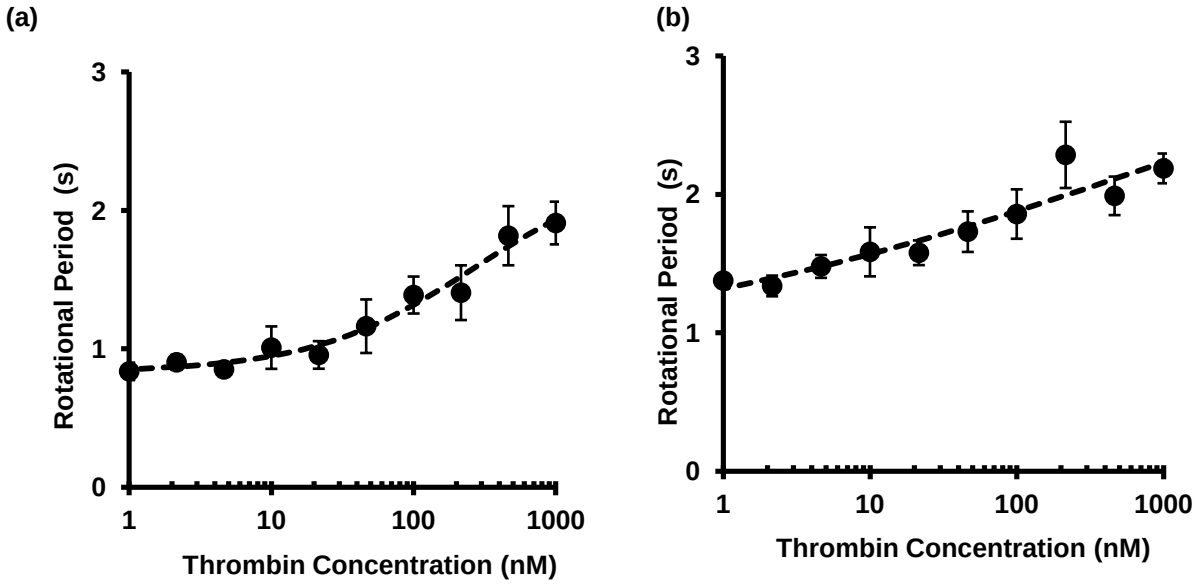

Figure 5.5—Dose response curves with (a) 22 μg/mL bead concentrations and (b) 70 μg/mL bead concentrations for bead assembly magnetorotation in whole serum spiked with human thrombin. Each point on the graph represents the average (± standard deviation) rotational period of ten bead assemblies, as calculated from videos of their rotation. The points were fit with the logistic Hill equation. The LOD for the curves, based on the mean ± 3 SD of the control, are (a) 16 nM, and (b) 7.5 nM. Note: The given concentrations of thrombin are *before* dilution; the actual concentrations after the dilution are 10,000x lower.

Partial Collapse of the Assemblies

In addition to serum nonspecific binding, one of the primary causes for the significantly poorer performance of BAM in serum was the partial inward collapse of the assemblies upon the initiation of magnetorotation, which was an unexpected occurrence.

The formation of the bead assembly, before the magnetic field was turned on, occurred as expected, with the beads collecting at the bottom of the droplet binding to each other, and then forming an assembly. However, once the magnetic field was turned on, the assemblies began to partially collapse inwards, i.e. collapse on themselves. This effect never occurred when BAM was performed with the beads coated only with the aptamers (and not PEG). When the beads were not PEGylated, as soon as the field was turned on, the assemblies locked into place, and began rotating, without any detectable collapse or change in the shape of the assembly.

The collapse of the assemblies with PEGylated beads occurred in both buffer and serum. It occurred with both 10K PEG and 2K PEG, as well as with aptamers both with and without the 20-base polyT tail. I believe that this is due to the lack of rigidity of the PEG molecule relative to the aptamer. The aptamer is a fairly bulky and rigid molecule, with plenty of intramolecular binding (e.g. GC-rich regions, complementary strands), double bonds, and intramolecular repulsions to stabilize it. The PEG molecule, however, is very flexible, being very hygroscopic, and containing no double bonds. I believe that the inclusion of the PEG molecule, even one as small as 2K (the smallest commercially available heterobifunctional PEG molecule), into the bead-bead linker significantly reduces its rigidity. When the field is turned on, the beads become magnetized, and attracted to each other, which creates a net force pulling towards the center of the assembly. Without the PEG molecule, the bead-bead linker is rigid enough to resist this inward pull. However, with the inclusion of the PEG molecule, the linker is no longer rigid enough to resist the inward force, leading to the assembly's partial inward collapse. A series of images showing this effect are given below in Figure 5.6.

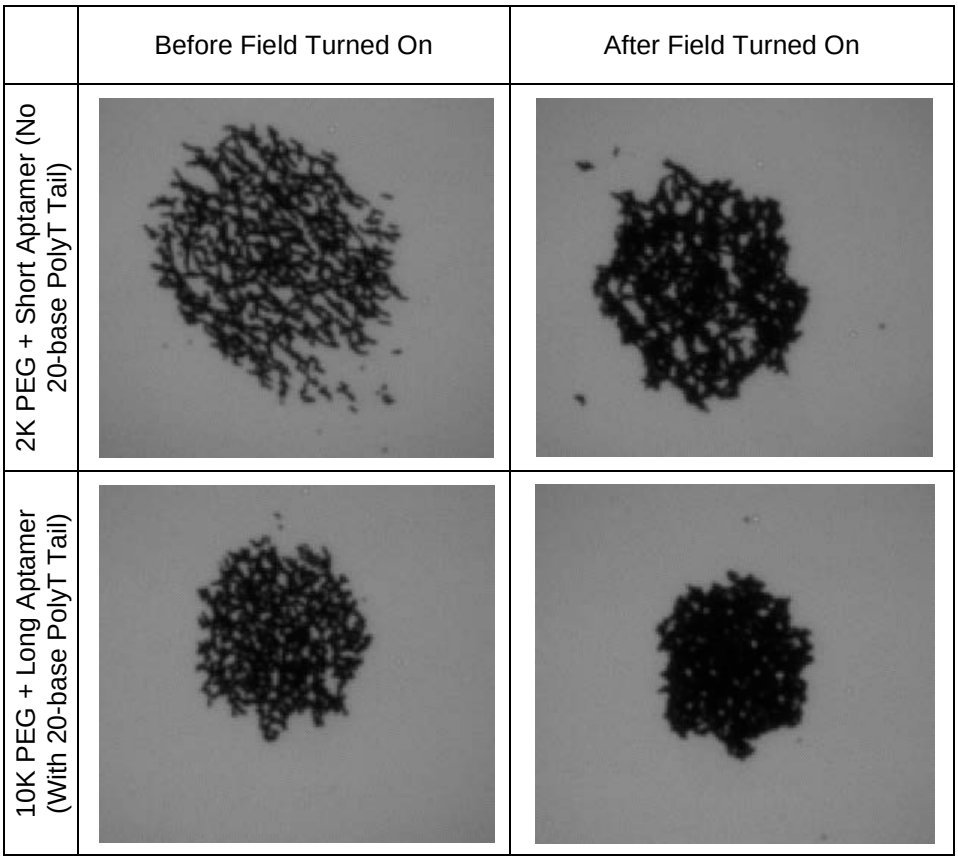

Figure 5.6—A series of figures illustrating the collapse of bead assemblies after turning on the rotating magnetic field. The top row of images shows beads functionalized with 2K PEG and short aptamers (with no 20-base polyT tail). The bottom row of images shows bead functionalized with 10K PEG and aptamers with a 20-base polyT tail.

Based on the results shown in Figures 5.5 and 5.6, it appears that BAM has the potential to work in serum; however, a much more rigid molecule that repels the nonspecific interactions of serum molecules with the bead would need to be found.

An additional method that was explored to potentially mitigate serum interactions was the use of nonspecific aptamer competitors, a concept that was used successfully in the work described in Chapter 6. The idea is that since the serum proteins stick to many biomolecules, they would just as likely bind to a random oligonucleotide sequence as to

our aptamer. Therefore, if a large excess of a random oligonucleotide sequence, on the order of the concentration of serum proteins in solution, was introduced into the serum, the serum proteins would bind to this nonspecific sequence, and not to our aptamer or our bead. The problem with this approach is that the thrombin aptamers are so sticky, that they bound to all of the nonspecific aptamer sequences that we tried to use. The aptamer used in Chapter 6 was designed for diagnostic applications, and therefore was less sticky, making the nonspecific aptamer strategy successful.

Evaluation of our Results in Context

One of the advantages of working with the thrombin aptamers is that their popularity makes it easy to compare the sensitivity of various diagnostic methods. Table 5.1 shows the results of a survey of the literature for proof-of-principle work for novel signal transduction mechanisms using the (same) thrombin aptamers, with results both in buffer as well as in serum.

In light of the results shown in Table 5.1, BAM compares pretty favorably to existing methods. In buffer, BAM has an LOD lower than all but one of the methods, and that one involved a multi-step amplified procedure that takes over 24 hours. I think it is particularly interesting that only three papers show quantitative results in serum. Additionally, those three reported LODs in serum are very close to each other, and very close to the results that I obtained during my experiments (Figure 5.5). I believe that this reflects the challenges associated with using the thrombin aptamers in serum. Based on these data, it seems like these aptamers have a relatively high affinity for serum proteins, which is an inherent limitation of the aptamers, and would be extremely difficult to

counteract without changing their structure. It seems like during the development of aptamers for application in diagnostic devices, it would be beneficial to test for their affinity towards nonspecific competitors such as serum proteins. It also seems like the thrombin aptamers are not well suited for use in proof of principle demonstrations of signal transduction methods in serum.

Paper	Signal Transduction Method	LOD Buffer	LOD Serum
Pavlov, JACS, 2004 [9]	Aggregation of Nanoparticles	20 nM	
Huang, Anal Chem, 2004 [10]	Capillary electrophoresis	9.8 nM	
Hianik, BMCL, 2005 [11]	Quartz crystal microbalance	1 nM	*
Liu, ACS Nano, 2012 [12]	Fluorescence	1 nM	
Radi, JACS, 2006 [13]	Fluorescent molecule beacons	500 pM	
Tennico, Anal Chem, 2010 [14]	Quantum Dots	500 pM	
Centi, Anal Chem, 2007 [15]	Electrochemical	450 pM	5 nM
Kim, Nanotechnology, 2009 [16]	Si-nanowire FET	330 pM	*
Cai, Sensors and Actuators, 2006 [17]	Electrochemical	100 pM	
Zhou, Anal Chem, 2012 [18]	SPR-phase imaging	100 pM	
Cho, Nano Letters, 2008 [19]	Raman scattering	100 pM	10 nM
Song, Chromatography, 2009 [20]	Capillary electrophoresis	83 pM	3 nM
Hu, JACS, 2012 [21]	Electrochemical	50 pM	
Bai, Biomaterials, 2012 [22]	Electrochemical (graphene-enhanced)	11 pM	
Ho, JACS, 2004 [23]	Label-free fluorescence	10 pM	
An, Lab Chip, 2010 [24]	SWNT Cantilevers	7 pM	
Li, Anal Chem, 2007 [25]	Enzymatically Amplified SPR	500 fM	
Hansen, JACS, 2006 [26]	Electrochemical breakdown of QD	500 fM	
Rahman, Anal Chem, 2009 [27]	Au-NP-Ferrocene Electrochemical	140 fM	*
Zhang, Biosensors Bioelec, 2009 [28]	NP-Amplified electrochemical (24 hr+)	6 fM	

Table 5.1—A survey of the literature showing the LODs in buffer and serum of 20 different systems using the thrombin aptamers as signal transduction molecules for the proof-of-principle demonstration of a new signal transduction method. Entries marked with an asterisk (*) indicate that the authors discussed that the method was performed in serum, but do not show any detailed data or report an LOD in serum. For paper [19], the LOD was reported as 1 nM in 10% diluted serum. For paper [20], the LOD was reported as 55 nM in 2% serum. Those values were adjusted to represent the LOD in whole serum, to enable a fair comparison.

In addition to comparing our system against other signal transduction methods that use the thrombin aptamers, we wanted to compare the performance specifications of our BAM system against those of what are generally considered to be the two leading research groups in the field of magnetic particle-based diagnostics, the Shan Wang group from Stanford University, and the Ralph Weissleder group from Harvard University. The Wang group uses giant magnetoresistance (GMR) as their signal transduction method, and the Weissleder group uses magnetic relaxation (MR) as their signal transduction method. As described in greater detail in Chapter 1, GMR operates by measuring the change in potential across a sensor surface due to the proximity of sandwich-label magnetic particles. MR operates by measuring the change in the relaxation time of magnetic nanoparticles due to their target-induced clustering. Both groups are far more advanced in the development of their system then we are, with working prototypes that, as of this writing, are undergoing commercial development and testing. Our system is still in the initial prototype stage, where I believe there is much room for improvement in many areas of the device. A summary of the comparison between the three systems is shown in Table 5.2 below.

All three systems are small enough to be portable, approximately what can be termed "hand-held." The smallest system is the Wang GMR, which measures approximately 8 x 16 x 3 cm. [29] The Weissleder MR system is slightly bigger, at 20 x 12 x 5 cm, [32] while our system is a little bigger still at approximately 15 x 15 x 50 cm. In terms of analysis time, the systems are all fairly similar; the Wang GMR has an analysis time of 20 minutes, [29] the Weissleder MR 30 minutes, [32] and our system 40 minutes. The sample volume required for analysis is also all fairly similar, in that the

volumes are on the order of a drop of blood; the Wang GMR has a sample volume of 50 μL, [29] the Weissleder MR 5 μL, [34] and our system 100 μL.

	Wang (GMR)	**Weissleder (MR)**	**Kopelman (BAM)**
Device Size	8 x 16 x 3 cm	20 x 12 x 5 cm	15 x 15 x 50 cm
Analysis Time	20 min	30 min	40 min
Sample Volume	50 μL	5 μL	100 μL
Magnetic Field Type	Electromagnet	Permanent (NdFeB)	Electromagnet
Magnetic Field Strength	8 mT	500 mT	5 mT
Magnetic Field Frequency	208 Hz	21.3 MHz	50 Hz
Magnetic Particle Size	50 nm	38 nm 1 μm	1 μm
LOD Buffer	13 fM (Lactoferrin) 57 fM (TNF-α)	1 pM (Tag peptide)	80 fM (Thrombin)
LOD Serum	4.8 pM (hCG) 5.7 pM (TNF-α)	4.7 pM (VEGF)	7.5 nM (Thrombin)
Device Material Costs	$194	$100	$250

Table 5.2—Comparison of various performance metrics of the Wang GMR system, the Weissleder MR system, and our BAM system. Sources of the information are [29, 30] for the Wang system and [31-34] for the Weissleder system.

In terms of magnetic properties, there are some differences between the systems. Both the Wang GMR and our system use an electromagnet, while the Weissleder MR system uses a NdFeB permanent magnet. The Wang GMR uses a magnetic field of amplitude 8 mT driven at 208 Hz, [30] while our system uses a field amplitude of 5 mT driven at 50 Hz. The Weissleder MR field is much stronger, with a field strength of 500 mT driven at 21.3 MHz, [32] however, since it uses a pulsed permanent magnet rather

than an electromagnet, its overall size is not much bigger. The Wang GMR system uses 50 nm iron oxide nanoparticles, [29, 30] while the Weissleder MR field uses both similar 38 nm iron oxide nanoparticles, as well as larger 1 μm particles. [34] Our system uses the same Dynal 1 μm particles that the Weissleder MR system uses.

Comparing LODs reported on different analytes is a little bit difficult, because the LOD depends on the quality of the affinity molecules used, but for each of the methods I've included the lowest limits of detection reported. For the Wang GMR, the lowest LOD reported in buffer was 13 fM for the antibacterial molecule lactoferrin, and the lowest LOD reported in serum was 4.8 pM for the pregnancy hormone human chorionic gonadotropin (hCG). [30] The only marker reported in both buffer and serum was the inflammatory cytokine TNF-α, which had a buffer LOD of 57 fM and a serum LOD of 5.7 pM, [30] suggesting that the system loses about two orders of magnitude transitioning from buffer to serum. In the Weissleder MR, the lowest reported LOD in buffer was 1 pM for tag peptide, [33] and the lowest reported LOD in serum was 4.7 pM for the angiogenesis factor VEGF. [31] As discussed earlier in this dissertation, the lowest LOD found for BAM in buffer is 80 fM for thrombin, and in serum the lowest LOD is 7.5 nM, also for thrombin.

The final metric to consider is the cost of the device. For the purposes of this discussion, I will focus only on the material costs of the device, because the final cost of the device will likely have to include substantial research and development and marketing outlays, which would significantly increase the total cost. Wang et. al estimate the material cost of their device at $194, which includes $105 for the electronic components, $40 for the battery, $18 for the metal enclosure, and $31 for the rest of the device

assembly. [29] Weissleder et. al provide a rough estimate of $100 for the total cost of their device, but do not provide any details on how they arrived at that number. [32] For our device, we estimate a total cost of around $250, with $40 for the electromagnetic coils, $50 for the amplifier, $100 for the photodiodes, $20 for the laser, and $40 for remaining components like electronics and filtering circuits.

Ultimately, the three devices have a good number of similarities. They are similar in size, price, analysis time, and sample volume. The Wang GMR and our system use similar magnetic fields and have similar buffer LODs. The Wang GMR and the Weissleder MR have similar serum performance, and the use of 40-50 nm particles. BAM and the Weissleder MR share the use of the 1 μm magnetic beads. The primary difference exists in the Weissleder MR's use of the much more powerful NdFeB permanent magnets and higher buffer LOD (perhaps mitigated by the fact that the device was optimized for cell detection rather than protein detection).

Future Work

For future work on this project, it seems that it might be worthwhile to move towards incorporating antibodies that are known to have relatively low affinity for serum proteins into BAM, in order to get a better sense of how this method could perform in a clinically relevant environment. For example, Chikkaveeraiah et. al have shown two pairs of sandwich antibodies, against prostate specific antigen (PSA), a prostate cancer biomarker, and interleukin-6 (IL-6), an inflammatory cytokine, that have femtomolar level sensitivity in human serum in a magnetic nanoparticle-based electrochemical assay. [35] Gnedenko et. al have shown a pair of sandwich antibodies against cardiac myoglobin

(cMb), a biomarker for heart attacks, that yield an LOD of 10 pM in human serum when used as part of a gold nanoparticle-amplified surface plasmon resonance detection system. [36] Jokerst et. al have shown a pair of sandwich antibodies against carcinoembryonic antigen (CEA), a cancer biomarker, which yield an LOD of 110 fM in human serum when used as part of a quantum-dot sandwich assay detection system. [37] Any of these pairs of sandwich antibodies seem like they would be good candidates for incorporation into BAM with the goal of showing improved, clinically relevant assay performance. The potential future of BAM rests in the ability to perform it in serum with clinically relevant antibodies.

Conclusion

Unfortunately, attempting to perform BAM in serum with the thrombin aptamers ran into a few unexpected complications, including the high affinity of the thrombin aptamers for serum proteins and the partial collapse of the PEGylated bead assemblies during magnetorotation due to the increased flexibility of the bead linkers. However, when comparing BAM to existing thrombin-based diagnostic systems, BAM compares quite favorably, both in buffer as well as in serum. BAM also has performance metrics similar to the two leading magnetic bead-based diagnostic systems. For future work, clinically relevant antibodies should be incorporated into BAM, and a more rigid anti-biofouling molecule should be found for surface functionalization of the beads.

Acknowledgments

I would like to thank Patrick Commiskey and Nicholas Shah for their assistance in performing experiments and analyzing data for these experiments. I would like to thank the Rackham Predoctoral Fellowship for providing financial support for this project.

References

1. Ladd, J., Z. Zhang, S. Chen, J.C. Hower, et al. Zwitterionic Polymers Exhibiting High Resistance to Nonspecific Protein Adsorption from Human Serum and Plasma. *Biomacromolecules*, 2008. **9**(5): p. 1357-1361.
2. Harris, J.M., Poly (ethylene glycol) chemistry: biotechnical and biomedical applications. 1992: Springer.
3. Oesterhelt, F., M. Rief, and H.E. Gaub. Single molecule force spectroscopy by AFM indicates helical structure of poly(ethylene-glycol) in water. *New Journal of Physics*, 1999. **1**(1): p. 6.
4. Yager, P., T. Edwards, E. Fu, K. Helton, et al. Microfluidic diagnostic technologies for global public health. *Nature*, 2006. **442**(7101): p. 412-418.
5. Daniel, K.D., G.Y. Kim, C.C. Vassiliou, M. Galindo, et al. Implantable diagnostic device for cancer monitoring. *Biosensors and Bioelectronics*, 2009. **24**(11): p. 3252-3257.
6. Khademhosseini, A., K.Y. Suh, S. Jon, G. Eng, et al. A Soft Lithographic Approach To Fabricate Patterned Microfluidic Channels. *Analytical Chemistry*, 2004. **76**(13): p. 3675-3681.
7. CreativePEGWorks. 2013; Available from: http://www.creativepegworks.com/heterobifunctional%20PEG.html.
8. Hermanson, G.T., Bioconjuagte Techniques. 2nd ed. 2008, Amsterdam, The Netherlands: Elsevier Inc.
9. Pavlov, V., Y. Xiao, B. Shlyahovsky, and I. Willner. Aptamer-Functionalized Au Nanoparticles for the Amplified Optical Detection of Thrombin. *Journal of the American Chemical Society*, 2004. **126**(38): p. 11768-11769.
10. Huang, C.-C., Z. Cao, H.-T. Chang, and W. Tan. Protein−Protein Interaction Studies Based on Molecular Aptamers by Affinity Capillary Electrophoresis. *Analytical Chemistry*, 2004. **76**(23): p. 6973-6981.
11. Hianik, T., V. Ostatná, Z. Zajacová, E. Stoikova, et al. Detection of aptamer-protein interactions using QCM and electrochemical indicator methods. *Bioorganic & Medicinal Chemistry Letters*, 2005. **15**(2): p. 291-295.
12. Liu, X., R. Aizen, R. Freeman, O. Yehezkeli, et al. Multiplexed aptasensors and amplified DNA sensors using functionalized graphene oxide: application for logic gate operations. *ACS Nano*, 2012. **6**(4): p. 3553-63.
13. Radi, A.-E., J.L. Acero Sánchez, E. Baldrich, and C.K. O'Sullivan. Reagentless, Reusable, Ultrasensitive Electrochemical Molecular Beacon Aptasensor. *Journal of the American Chemical Society*, 2005. **128**(1): p. 117-124.
14. Tennico, Y.H., D. Hutanu, M.T. Koesdjojo, C.M. Bartel, et al. On-Chip Aptamer-Based Sandwich Assay for Thrombin Detection Employing Magnetic Beads and Quantum Dots. *Analytical Chemistry*, 2010. **82**(13): p. 5591-5597.

15. Centi, S., S. Tombelli, M. Minunni, and M. Mascini. Aptamer-Based Detection of Plasma Proteins by an Electrochemical Assay Coupled to Magnetic Beads. *Analytical Chemistry*, 2007. **79**(4): p. 1466-1473.

16. Kim, K.S., H.-S. Lee, J.-A. Yang, M.-H. Jo, et al. The fabrication, characterization and application of aptamer-functionalized Si-nanowire FET biosensors. *Nanotechnology*, 2009. **20**(23): p. 235501.

17. Cai, H., T.M.-H. Lee, and I.M. Hsing. Label-free protein recognition using an aptamer-based impedance measurement assay. *Sensors and Actuators B: Chemical*, 2006. **114**(1): p. 433-437.

18. Zhou, W.J., A.R. Halpern, T.H. Seefeld, and R.M. Corn. Near infrared surface plasmon resonance phase imaging and nanoparticle-enhanced surface plasmon resonance phase imaging for ultrasensitive protein and DNA biosensing with oligonucleotide and aptamer microarrays. *Analytical Chemistry*, 2012. **84**(1): p. 440-5.

19. Cho, H., B.R. Baker, S. Wachsmann-Hogiu, C.V. Pagba, et al. Aptamer-Based SERRS Sensor for Thrombin Detection. *Nano Letters*, 2008. **8**(12): p. 4386-4390.

20. Song, M., Y. Zhang, T. Li, Z. Wang, et al. Highly sensitive detection of human thrombin in serum by affinity capillary electrophoresis/laser-induced fluorescence polarization using aptamers as probes. *Journal of Chromatography A*, 2009. **1216**(5): p. 873-878.

21. Hu, J., T. Wang, J. Kim, C. Shannon, et al. Quantitation of Femtomolar Protein Levels via Direct Readout with the Electrochemical Proximity Assay. *Journal of the American Chemical Society*, 2012.

22. Bai, L., R. Yuan, Y. Chai, Y. Zhuo, et al. Simultaneous electrochemical detection of multiple analytes based on dual signal amplification of single-walled carbon nanotubes and multi-labeled graphene sheets. *Biomaterials*, 2012. **33**(4): p. 1090-1096.

23. Ho, H.-A. and M. Leclerc. Optical Sensors Based on Hybrid Aptamer/Conjugated Polymer Complexes. *Journal of the American Chemical Society*, 2004. **126**(5): p. 1384-1387.

24. An, T., K.S. Kim, S.K. Hahn, and G. Lim. Real-time, step-wise, electrical detection of protein molecules using dielectrophoretically aligned SWNT-film FET aptasensors. *Lab on a Chip*, 2010. **10**(16): p. 2052-2056.

25. Li, Y., H.J. Lee, and R.M. Corn. Detection of Protein Biomarkers Using RNA Aptamer Microarrays and Enzymatically Amplified Surface Plasmon Resonance Imaging. *Analytical Chemistry*, 2007. **79**(3): p. 1082-1088.

26. Hansen, J.A., J. Wang, A.-N. Kawde, Y. Xiang, et al. Quantum-Dot/Aptamer-Based Ultrasensitive Multi-Analyte Electrochemical Biosensor. *Journal of the American Chemical Society*, 2006. **128**(7): p. 2228-2229.

27. Rahman, M.A., J.I. Son, M.S. Won, and Y.B. Shim. Gold nanoparticles doped conducting polymer nanorod electrodes: ferrocene catalyzed aptamer-based thrombin immunosensor. *Analytical Chemistry*, 2009. **81**(16): p. 6604-11.

28. Zhang, X., B. Qi, Y. Li, and S. Zhang. Amplified electrochemical aptasensor for thrombin based on bio-barcode method. *Biosensors & Bioelectronics*, 2009. **25**(1): p. 259-62.

29. Gaster, R.S., D.A. Hall, and S.X. Wang. nanoLAB: An ultraportable, handheld diagnostic laboratory for global health. *Lab on a Chip*, 2011. **11**(5): p. 950-956.

30. Osterfeld, S.J., H. Yu, R.S. Gaster, S. Caramuta, et al. Multiplex protein assays based on real-time magnetic nanotag sensing. *Proceedings of the National Academy of Sciences of the United States of America*, 2008. **105**(52): p. 20637-20640.

31. Haun, J.B., C.M. Castro, R. Wang, V.M. Peterson, et al. Micro-NMR for Rapid Molecular Analysis of Human Tumor Samples. *Science Translational Medicine*, 2011. **3**(71): p. 71ra16.

32. Issadore, D., C. Min, M. Liong, J. Chung, et al. Miniature magnetic resonance system for point-of-care diagnostics. *Lab on a Chip*, 2011. **11**(13): p. 2282-2287.

33. Koh, I., R. Hong, R. Weissleder, and L. Josephson. Sensitive NMR Sensors Detect Antibodies to Influenza. *Angewandte Chemie*, 2008. **120**(22): p. 4187-4189.

34. Lee, H., E. Sun, D. Ham, and R. Weissleder. Chip-NMR biosensor for detection and molecular analysis of cells. *Nature Medicine*, 2008. **14**(8): p. 869-874.

35. Chikkaveeraiah, B.V., V. Mani, V. Patel, J.S. Gutkind, et al. Microfluidic electrochemical immunoarray for ultrasensitive detection of two cancer biomarker proteins in serum. *Biosensors and Bioelectronics*, 2011. **26**(11): p. 4477-4483.

36. Gnedenko, O.V., Y.V. Mezentsev, A.A. Molnar, A.V. Lisitsa, et al. Highly sensitive detection of human cardiac myoglobin using a reverse sandwich immunoassay with a gold nanoparticle-enhanced surface plasmon resonance biosensor. *Analytica Chimica Acta*, 2013. **759**(0): p. 105-109.

37. Jokerst, J.V., A. Raamanathan, N. Christodoulides, P.N. Floriano, et al. Nano-bio-chips for high performance multiplexed protein detection: Determinations of cancer biomarkers in serum and saliva using quantum dot bioconjugate labels. *Biosensors and Bioelectronics*, 2009. **24**(12): p. 3622-3629.

Chapter 6

Aptamers as Affinity Reagents in an Integrated Electrophoretic Lab-on-a-Chip Platform

Introduction

Over the past few decades, microfluidic devices have garnered much attention as potential medical diagnostic tools. Such devices are particularly attractive for satisfying diagnostic needs at the point-of-care or first responder settings without phlebotomy, through a high level of automation in a compact device that requires only a droplet of sample. [1-4] Advantages of scale and integration with these devices also tend to shorten analysis times from hours to minutes, while still achieving quantitative detection of trace analytes. The group with which I worked at Sandia has developed an integrated microfluidic platform that addresses several requirements for point-of-care diagnostics of disease and toxin exposure. [5-10] To date we have reported on diagnostic assays that utilize antibodies as specific recognition elements, as is typical for the majority of commercial diagnostics targeting proteins and several other classes of biomarkers. However for certain point-of-care settings and first responder scenarios, cost and logistical concerns related to stability and shelf-life of antibodies warrant consideration of alternative affinity reagents. Several promising antibody alternatives have been developed for therapeutic and diagnostic purposes over the last couple of decades with an

emphasis on engineered polypeptide and polynucleotide affinity reagents. [11-13] These reagents can be engineered with high affinity, specificity and thermostability, and are manufacturable in high purity and reproducibility at low cost once identified.

Aptamers are selected from randomized nucleotide sequence pools to bind to a molecular target (e.g. proteins or peptides) with high affinity and specificity, similar to antibodies. [14] Aptamers have been used for a wide range of diagnostic [15-19] and therapeutic [20] applications. Most aptamers to date have been derived through the SELEX process (systematic evolution of ligands by exponential enrichment), whereby a randomly generated pool of oligonucleotides is mixed with the target of interest, and oligonucleotides that display affinity for the target are separated and amplified repeatedly until the highest affinity oligonucleotides are isolated. [15] Recently, an alternative process in which the pool of oligonucleotides is synthesized on beads has emerged which reduces the need for multiple enrichment cycles and better accommodates nucleotide modifications. The target is mixed with the beads, beads displaying affinity for the target are isolated and the corresponding sequences are identified. One or a few rounds of this process can yield a sequence with high affinity for the target. [21-26] Incorporating modified nucleotides can improve nuclease resistance and enrich chemical complexity of the library to enhance affinity and specificity. A prominent example is the thioaptamer, incorporating phosphorothioate-modifications in which one (monothio) or both (dithio) of the nonbridging oxygen atoms on the phosphate backbone of the nucleic acid strand are replaced with sulfur atoms. [24, 26]

Aptamers exhibit several benefits over antibodies for diagnostic applications. Aptamers can be synthesized to target diverse classes of molecules, precisely controlled

for desired physicochemical properties, easily modified for purposes such as labeling, and produced at low cost with high uniformity from batch to batch. Aptamers are also significantly more robust than antibodies [27], making them better suited for ambient reagent storage and point-of-care operation, eliminating cold-chain transportation needs. This property is especially advantageous for devices designed for operation in resource-deficient areas, such as third-world regions and outer space.

Here, we demonstrate the suitability of nucleic acid affinity reagents in an integrated electrophoretic gel-shift detection platform. A model aptamer [28] targeting immunoglobulin E (IgE) and a model thioaptamer [29, 30] targeting nuclear factor-kappa B (NF-κB) were evaluated. IgE is one of five classes of antibodies produced by humans, and functions primarily in generating allergic reactions [31] and in defending the body against parasites. [32] NF-κB is a protein that controls the transcription of DNA, and mediates a wide range of physiological responses, specifically immune responses to cytokines and antigens. [33, 34] Improper regulation of NF-κB can lead to a variety of diseases, including cancer. [35, 36]

We investigated assay performance with spiked serum samples where potential interference from the serum matrix and high abundance proteins on affinity shift assays has been explored to a limited extent with conflicting results. Some previous experiments have reported significant nonspecific interactions between DNA aptamers and serum proteins in 10% serum, [37] and in cell culture media, [38] as well as the benefits of using an excess of nonspecific aptamers to minimize interactions between serum proteins and aptamers in capillary electrophoresis [39] and fluorescence detection. [40] Others have reported serum-based aptamer assays without notable interference in

capillary electrophoresis [41] and fluorescence polarization anisotropy. [18] Here, a competitive inhibition strategy using excess nonspecific oligonucleotides was required to suppress serum interference.

Finally, a distinguishing feature of the integrated platform is the incorporation of a size-exclusion membrane to mix and incubate affinity reagents with sample proteins as well as to preconcentrate sample proteins and perform sample buffer exchange prior to electrophoretic separations analysis. [5, 6, 9] This mode of mixing reagents automates key assay steps on-chip in rapid fashion. Enhancing the assay sensitivity by several orders of magnitude through preconcentration is critical for achieving required detection limits for a number of trace analytes. However, the membrane formulations previously reported for this platform [6, 42] were optimized for concentrating SDS denatured proteins prior to SDS PAGE sizing and for trapping antibody reagents and target proteins prior to gel-shift affinity assays. We report on system performance with aptamer reagents of smaller size and higher charge density. A key benefit of employing aptamers is their superior gel shift properties compared to antibodies. Modification and optimization of the exclusion membrane were required to improve the performance of integrated aptamer-based affinity assays. Best results were achieved through incorporation of a mild charge into the nanoporous size exclusion membrane. We demonstrate that on-chip preconcentration, mixing, buffer exchange, and detection of target analytes in serum samples are readily achieved within the integrated platform.

Materials and Methods

Reagents

Human IgE protein (MW 190,000) was obtained from Scripps Laboratories (San Diego, CA). Human Recombinant NF-κB (p50, 50 gsu) was obtained from the Promega Corporation (Madison, WI). AlexaFluor 488- and 647-labeled anti-IgE aptamer [28] (MW 13,218) was obtained from Integrated DNA Technologies (Coralville, IA). The sequences for these aptamers are shown below:

5′- AF488-TTTGGGGCACGTTTATCCGTCCCTAGTGGCGTGCCCC – 3′

5′- AF647-TTTGGGGCACGTTTATCCGTCCCTAGTGGCGTGCCCC – 3′

AlexaFluor 647-labeled anti-NF-κB p50 mouse monoclonal antibody was purchased from Santa Cruz Biotechnology (Santa Cruz, CA). AlexaFluor 647-labeled anti-NF-κB thioaptamer (MW ~10,188) was obtained from AM Biotechnologies (Houston, TX). Bold and underlined bases represent phosphorodithioate modifications.

5′– AF647-CCAGGAGA**TT**CCAC – 3′

3′- G**G**TC**C**T**C**TAAG**G**AC - 5′

Masking aptamers, (AB77A (MW 17,197) and AB77B (MW 17,268)), synthetic oligonucleotides with 5' biotin, were also obtained from AM Biotechnologies (Houston, TX).

AB77A: 5′-biotin-

CATCCCTCTGTC**A**ATACCG**A**ACACAAA**A**GGG**A**AA**A**GCCC**A**CCCATCGCCTTGAA-3′

AB77B: 5′-biotin-

CAACCATGGATTAGC**A**CTCC**A**GG**A**TGG**A**GCGCCCCG**A**CTG**A**TCTTGCCGCCCAA-3′

3-(trimethoxysilyl)propyl methacrylate (98%), 40% acrylamide, 30% (37.5:1) acrylamide/bisacrylamide, bovine serum albumin (BSA), sodium azide, and methyl

cellulose powder were purchased from Sigma (St. Louis, MO). A fraction of BSA was labeled with AlexaFluor 647 per the manufacturer's instructions to be used as an internal standard for antibody-based immunoassays. N,N'-methylenebisacrylamide and 0.2 M pK 4.6 and pK 6.2 Immobiline solutions were obtained from Fluka (Buchs, Switzerland). Water-soluble photoinitiator 2,2'-Azobis[2-methyl-*N*-(2-hydroxyethyl)propionamide] (VA-086) was purchased from Wako Chemicals (Richmond, VA). 10x Tris-Glycine (25 mM Tris, 192 mM Glycine, pH 8.3) electrophoresis buffer was purchased from BioRad (Hercules, CA). Deionized water (18.2 MΩ) was obtained using an Ultrapure water system from Millipore (Milford, MA). Off the clot mouse serum was purchased from Innovative Research (Novi, MI). Upon receipt, serum was thawed at 37°C, mixed with 0.05% (w/v) sodium azide, filtered with 0.2µm syringe filters (Whatman, UK), aliquotted and stored at -20°C until use.

Microchip Fabrication

Glass (fused silica) microchips were designed in-house and fabricated by Caliper Life Sciences (Hopkinton, MA) using standard photolithography, wet etching, bonding and dicing methods. Two previously-described microchip designs [5, 7] were used in this work: a standard offset T design (Figure 6.1a) and a more complex integrated preconcentration device (Figure 6.1b). Note that, unlike previous publications from our group, devices in this work used noncrosslinked 1% methyl cellulose (MC) solutions as the sieving media versus the *in situ* photopolymerized polyacrylamide used previously. [6, 42] 1% MC was found to be advantageous for the present application in terms of device yield and reusability, while providing sufficient sieving power for the analytes.

For both devices, the channel walls were first coated with acrylate-terminated self-assembled monolayers as previously described. [6, 8, 42] Briefly, the channels were conditioned with 1M NaOH, rinsed with deionized water, and dried thoroughly using a vacuum. A 2:3:5 (v/v/v) mixture of 3-(trimethoxysilyl) propyl methacrylate, glacial acetic acid, and deionized water was loaded into the channels. Devices were incubated with the solution for 30 minutes, rinsed with a 3:7 mixture of acetic acid and water, rinsed with deionized water, and thoroughly dried with a vacuum. Next, the channels of the offset T-chips were coated with a 5% linear acrylamide coating by loading in a solution of 5% acrylamide, 0.2% (w/v) VA-086 photoinitiator and exposing to a 100W flood UV lamp for 6 minutes. Following exposure, excess solution was removed via vacuum and the channels were flushed twice with MeOH and stored dry until use.

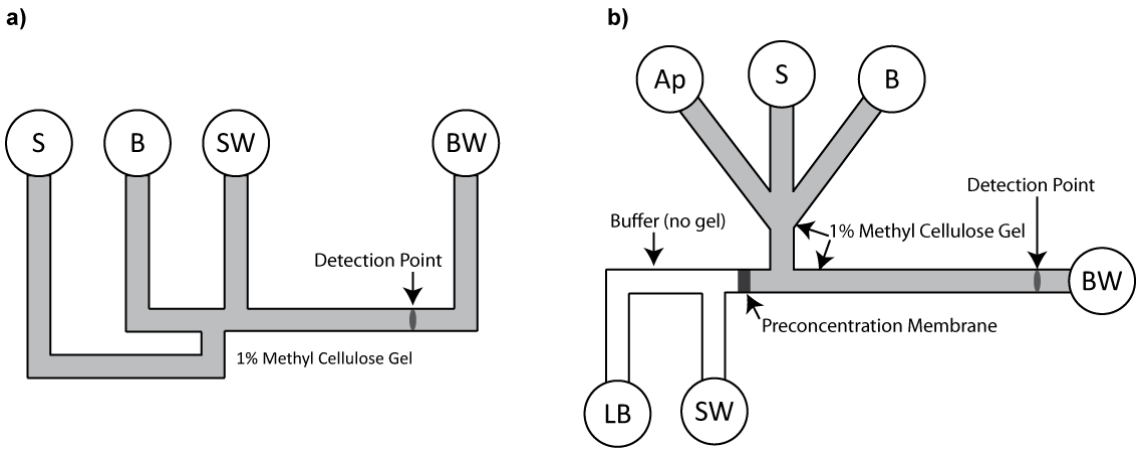

Figure 6.1—Schematics of offset T-chip and preconcentration chip designs. (a) Offset T-chip: S = Sample Inlet, B = Buffer Inlet, SW = Sample Waste Outlet and BW = Buffer Waste Outlet. Approximate length from junction to BW is 2.9 cm. Detector is positioned approximately 15 mm from junction. (b) Preconcentration chip: Ap = Aptamer Inlet, S = Sample Inlet, B = Buffer Inlet, LB = Loading Buffer, SW = Sample Waste, BW = Buffer Waste Outlet. Detector is positioned approximately 15mm from membrane. All channels are 100µm wide × 35µm deep. Voltage schemes for conducting assays included in the Materials and Methods section.

For the integrated preconcentration devices, the nanoporous polyacrylamide membranes were fabricated prior to coating the devices with the 5% linear acrylamide coating. Membrane fabrication was accomplished using in situ photopolymerization techniques previously described. [5, 6, 9] Briefly, the devices were loaded with a solution of acrylamide monomer, bisacrylamide crosslinker, and VA-086 photoinitiator. For neutral size-exclusion membranes, this solution composed 45%T, 12%C (where %T represents the total monomer mass concentration, and %C represents the mass percentage of crosslinker to total monomer). For charged membranes, this solution composed 40%T, 12%C, 18.4 mM pK 4.6 Immobiline, and 1.6 mM pK 6.2 Immobiline (solution pH = 4.4). ~ 50-µm-wide membranes were defined in the channel by exposure to a shaped UV laser beam (355nm frequency-tripled Nd:YAG). Following membrane polymerization, excess monomer solution was removed via vacuum, channels were rinsed twice with MeOH and filled with 5% linear acrylamide solution for coating, as was done with the offset T chips. Following the photopolymerized coating, the chips were rinsed with MeOH, dried via vacuum, and stored dry until use.

Microchip Operation

1% MC solution was prepared by slowly dissolving 1.5 g of methyl cellulose in 100 mL 1X Tris-Glycine buffer over a hot plate. The solution was then immediately chilled and stirred in an ice bath until all MC was dissolved. Prior to use, the chips were filled with the 1% MC gel solution via capillary wicking. Previous work has demonstrated excellent resolution between free aptamer and complex peaks through capillary electrophoresis or capillary zone electrophoresis modes without the use of a

sieving matrix. [16, 43] However, we employ the 1% MC liquid gel here because (a) our assays are being developed for a multiplexed chip using a single matrix that must resolve some species that require sieving, and (b) we have found sieving gels more compatible with integrated preconcentration using nanoporous size-exclusion membrane. Chips were loaded into custom manifolds, as previously described. [10]. Buffer solution (no MC) is continually flowed by gravity through the channels composing the backside of the nanoporous membrane in the integrated preconcentration chips to help negate any ion depletion effects on either side of the membrane. Samples (fluorescently-labeled aptamer + target analyte) were mixed in 1% MC gel solutions and added to the sample reservoir on the manifold following a 10 minute incubation at room temperature. For the preconcentration experiments, the aptamer and target analyte were diluted in separate solutions and loaded into corresponding reservoirs on the manifold. During all experiments, the total sample volume was held constant at 80 μL. In each sample, the concentration of aptamer was fixed at 10 nM, and the concentration of spiked target varied from 0.250-80 nM for IgE and 2-80 nM for NF-κB. Soaking the manifold in a 5 mg/mL solution of BSA between runs reduced sample adsorption to the sides of the manifold, and improved signal quality.

Platinum electrodes were inserted into each fluid reservoir on the chip and connected to a programmable high-voltage power supply developed and fabricated in-house. For the offset T-chips, separation and detection was accomplished using voltage schemes consistent with earlier operation. [7] To load the sample into the main separation channel, a 300 V/cm electric field potential was applied between the S and SW reservoirs for 60 seconds. The voltage was then switched to electrophoretically separate the sample

in the main channel by applying 300 V/cm between the B and BW reservoirs for 120 seconds. For the integrated preconcentration chips, samples were first loaded into the aptamer or sample (target) reservoir, then electrophoretically driven to the preconcentration membrane by applying 10 V/cm between the respective reservoir and the SW reservoir for varying time intervals. Following preconcentration, samples were eluted from the membrane into the separation channel by applying 30 V/cm between the LB and BW reservoirs for 10 seconds, then separated by applying 300 V/cm between the B and BW reservoirs for 120 seconds.

Sample migration was observed 15 mm down the separation channel using laser-induced fluorescence (LIF). Excitation light (argon ion laser, 488 nm and 647 nm) was frequency modulated using a mechanical chopper (220-Hz modulation) and reflected off a dichroic mirror (XF2010) through a 40x microscope objective (New Focus, Inc., San Jose, CA) that defined the detection point on the microchip. Fluorescence was detected by a Hamamatsu H5784 photomultiplier tube (PMT). The signal from the PMT was demodulated using a lock-in amplifier (Stanford Research Systems, Sunnyvale, CA), and the signal was collected using a computer via a data acquisition interface (6020E DAQPad, National Instruments, Austin, TX). Data were collected using an in-house program written in LabVIEW (National Instruments).

Quantifying Performance

Electropherogram peak areas were calculated using a program written in-house. Complex (aptamer + target) peak areas are reported as normalized complex peak area (complex peak area / [complex peak area + free aptamer peak area]). Dose-response

curves were generated by measuring the respective peak areas for varying concentrations of target analyte, then fit using the four-parameter logistic model [44] in equation 6.1 below

$$y = d + \frac{a - d}{\left[1 + \left(\frac{x}{c}\right)^{b}\right]} \tag{6.1}$$

where *a* is the estimated response at zero concentration of the target, *b* is the Hill coefficient, which refers to the steepness of the sigmoidal dose-response curve and is related to the binding constant, *c* is the mid-range concentration (C_{50}), *d* is the estimated response at infinite concentration, *x* is the target concentration and *y* is the normalized complex peak area. Although a reference standard is preferred for peak normalization, several chosen reference compounds overlapped with either the free aptamer peak or the complex peak. Instead, total fluorescence of the sample was used to normalize electropherograms which was deemed adequate for the goals of this study.

Results and Discussion

Aptamer Performance in Buffer Conditions

Representative aptamer affinity gel-shift assay results for the anti-NF-κB thioaptamer and the anti-IgE aptamer are presented in Figures 6.2 and 6.3, respectively, for a range of target analyte concentrations. The free aptamer peaks are readily baseline resolved from the aptamer-target complex peaks using 1% MC gel solution. The peak at 20 seconds corresponds to the free aptamer, while the peak at 60-80 seconds corresponds to the aptamer bound to its target. A typical dose-dependent response was observed, with

the free aptamer peak decreasing and the complex peak increasing with higher target analyte concentrations.

The dose responses plotted in Figure 6.2b and Figure 6.3b were fit using the four-parameter logistic model in equation 6.1. For Figure 6.2b, a = 0.00, b = 1.44, c = 13.11, and d = 1.00. For Figure 6.3b, a = 0.00, b = 1.37, c = 3.02, and d = 1.00. The anti-IgE aptamer demonstrated dynamic sensitivity over the IgE concentration range of ~0.5-20 nM, while the anti-NF-κB thioaptamer demonstrated dynamic sensitivity over the NF-κB range of ~5-80 nM. These results are consistent with high affinity interactions expected for these previously characterized reagents.

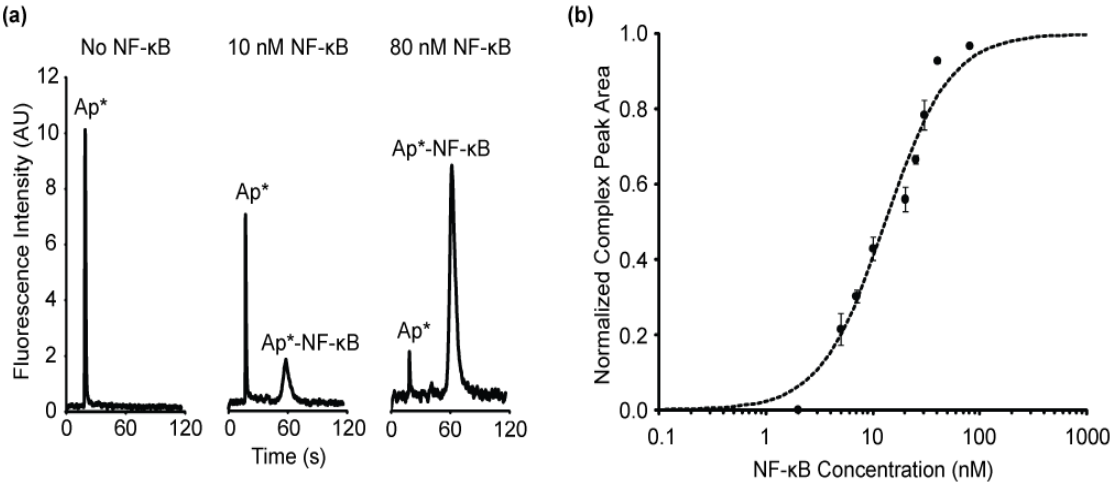

Figure 6.21—(a) Electropherogram of 10 nM AF647-anti-NF-κB thioaptamer with NF-κB spiked in buffer conditions. The peak at 20 seconds is the free aptamer peak (Ap*), and the peak around 60 seconds is the aptamer-target complex peak (Ap*-NF-κB). As the concentration of target is increased (with constant aptamer concentration), the free aptamer peak decreases while the complex peak increases. (b) Dose-response curve of AF647-anti-NF-κB thioaptamer with NF-κB spiked in buffer. Curve was fit using the four-parameter logistic model in equation 6.1; r2 = 0.981.

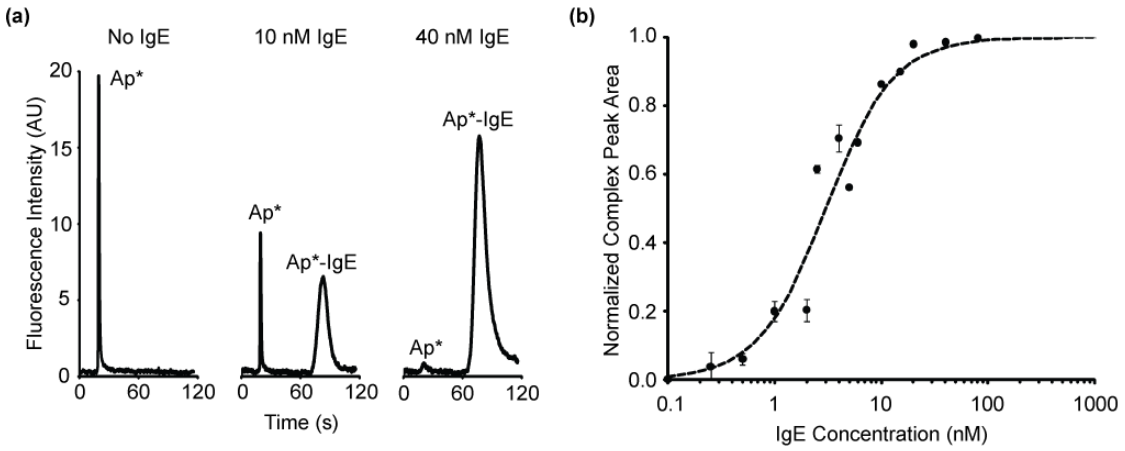

Figure 6.3—(a) Electropherogram of 10 nM AF488-anti-IgE aptamer with IgE spiked in buffer conditions. The peak at 20 seconds is the free aptamer peak, and the peak around 60 seconds is the aptamer-target complex peak. As the concentration of target is increased (with constant aptamer concentration), the free aptamer peak decreases while the complex peak increases. Peak areas were normalized here by dividing by the total fluorescent intensity. (b) Dose-response curve of AF488-anti-IgE aptamer with IgE spiked in buffer. Curve was fit using the four-parameter logistic model in equation 6.1; r2 = 0.955.

To demonstrate potential advantages of aptamers over antibodies for on-chip electrophoretic gel-shift detection, we compared the performance of the anti-NF-κB thioaptamer with that of an AlexaFluor 647-labeled anti-NF-κB monoclonal antibody. Free probes are separated from target-bound affinity probes based on differing electrophoretic mobilities, which are a function of the mass to charge ratio of the two species. When considering the molecular weight (MW) range of typical assay targets, MW_{target} ~ 1-200 kDa, the shift in MW upon binding in a direct assay format for aptamers ($MW_{aptamer}$ ~ 10 kDa + MW_{target}) is much greater than for standard IgG antibodies (MW_{Ab} ~ 150 kDa + MW_{target}) due to the smaller size of aptamers. Furthermore, the modest net charge density of most biochemical targets compared to the high charge density of aptamers favors enhanced mobility shifts upon binding. Gel shifts are more likely to be

resolved with aptamer reagents, particularly for lower molecular weight targets including typical cytokines. The immunoassay format was first attempted using the same 1% MC gel solution used for aptamer assays, however the sieving power of the liquid gel was not sufficient to resolve the free antibody and complex peaks. A crosslinked polyacrylamide gel 8%T, 2.6%C was therefore used to increase sieving power and achieve an immunoassay gel-shift. Electropherograms obtained with an offset T-chip are included in Figure 6.4. The free antibody peak requires much longer elution time at 132 seconds compared to the 20 seconds resolution of free aptamer peaks. More importantly, the free antibody peak and the immunocomplex peak overlap significantly, preventing quantitative analysis of the electropherograms, whereas the aptamer complex is easily baseline resolved.

Although the resolution advantage of aptamers over antibodies is clearly apparent for this case by visual inspection of the electropherograms, we can also quantify the separation resolution for each case using equation 6.2 below

$$R_s = \frac{T_2 - T_1}{2\left(\tau_1 + \tau_2\right)} \tag{6.2}$$

where T_1 and T_2 represent the elution time of the free probe and probe-target complex, respectively, and τ_1 and τ_2 represent the standard deviation due to dispersion of the respective peaks. In general, $R_s > 1$ is desired, while $R_s = 1.5$ is considered baseline resolution.

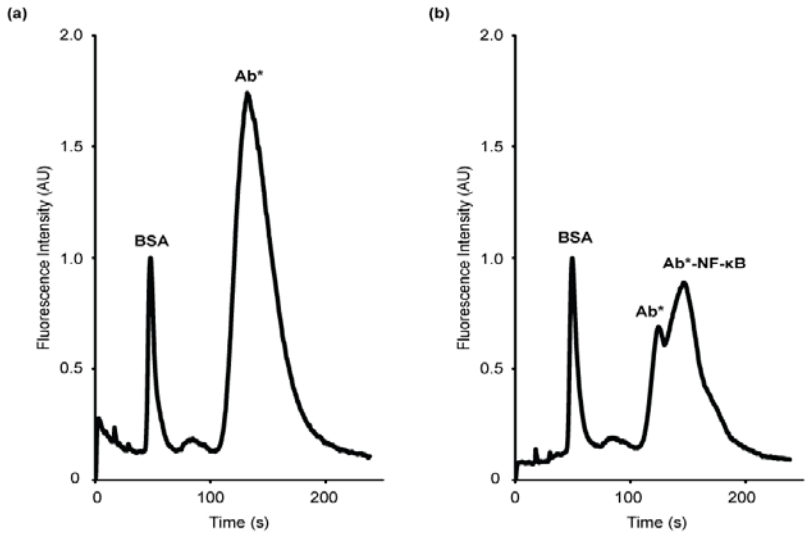

Figure 6.4—On-chip detection of NF-κB using a fluorescently-labeled antibody. Peaks are normalized to the AF647-labeled BSA (10 nM) standard peak. (a) 10 nM AF647-labeled anti-NF-κB antibody and (b) 10 nM AF647-labeled anti-NF-κB antibody with 10 nM NF-κB. BSA reference standard eluted at ~50 seconds. The second peak represents (a) free antibody and (b) free antibody plus antibody-NF-κB complex. In the latter case, the antibody-NF-κB complex peak overlaps with free antibody, preventing quantification. This example illustrates potential challenges and limitations in separation resolution with gel-shift immunoassays. Targets in this MW range are generally resolved by immunoelectrophoresis, but separation conditions may require more extensive optimization than aptamers and/or screening of antibody reagents for suitable electrophoretic gel-shift properties.

For the antibody-based electropherogram in Figure 6.4, R_s = 0.385 (well below desired resolution). For the corresponding electropherogram of 10nM anti-NF-κB thioaptamer and 10nM NF-κB in Figure 6.2a, R_s = 4.86 (well above baseline resolution). The resolution of a gel-shift assay is dependent on several factors including the affinity probe properties and buffer characteristics and further development would likely yield an acceptable immunoassay for a target in this size range. However, this example highlights a clear general advantage in using aptamers to achieve separation resolution in this system.

Aptamer Performance in Serum

Running the aptamer-based affinity assays in serum presents a series of additional challenges due to sample complexity. Serum contains highly abundant proteins, most prominently immunoglobulin and albumin, in addition to high salt concentrations compared to optimal electrophoretic separation buffers. Consistent with some, but not all, earlier reported work with aptamer assays in serum, initial electrophoretic evaluations here showed significant nonspecific interactions of serum components with the aptamer. Figure 6.5a illustrates challenges imposed by non-specific interference, where serum concentrations as low as 5% still caused significant loss of the free aptamer peak and introduction of multiple non-specific complex peaks. In attempts to identify interfering serum components, the AF647-anti-NF-κB thioaptamer was incubated with an isolated mixture of the two most abundant serum proteins, mouse IgG and albumin at approximate serum concentrations. However, no evidence of aptamer interactions with these proteins was observed (data not shown). To address non-specific serum interference with aptamers, we evaluated a panel of additives spiked in the sample and running gel buffer, including 5 mg/mL of Tween-20, 0.1% (w/v) SDS, 10 mM Triton X-100, a high-salt buffer, [43] and excesses of a 10-bp ssDNA ladder and a 100 kDa *E. coli* plasmid. However, none of these initial treatments succeeded in preventing nonspecific serum-aptamer interactions without also interfering with aptamer-target binding (not shown).

We therefore evaluated closer analogues of the anti-NF-κB thioaptamer in a competitive suppression strategy. Best success was realized using a 20-fold excess (1.2 μM) of two thioaptamer candidates similar in size and chemical properties to the anti-NF-κB thioaptamer but enriched in selection for other targets. The mixture of these masking

aptamers eliminated losses of AF647-anti-NF-κB thioaptamer and the formation of non-specific complex peaks in 10% serum (Figure 6.5b). Success using a similar strategy with a 40-fold excess of a nonspecific oligonucleotide was previously reported. [39, 40] In our experiments, the closer analogues of the anti-NF-κB thioaptamer competed more effectively for non-specific binding sites than small ssDNA ladder and larger plasmid DNA. Furthermore, this particular masking aptamer mixture was more effective than other masking aptamers evaluated and either masking aptamer alone (not shown). Importantly, the masking aptamers did not interfere with high affinity binding interactions of the AF647-anti-NF-κB thioaptamer with NF-κB. These results expand upon previously-described suppression strategies to mitigate matrix interference and emphasize the value in screening close analogues to aptamers under evaluation.

In contrast to the results observed in simple buffer (Figure 6.2), binding of AF647-anti-NF-κB thioaptamer to NF-κB in the presence of 10% serum (including the masking aptamers) resulted in two prominent complex peaks. The first complex peak decreased with increasing NF-κB concentration, while the second peak increased. Formation of higher order complexes, possibly involving one or more serum components, may explain shifts to later elution times at higher NF-κB concentrations. Further investigation is needed to elucidate this finding. A dose-response curve was approximated based on the assumption that the second and third peaks both represent aptamer-NF-κB complex (Figure 6.6). Although masking aptamers significantly reduced serum matrix interference, the dose-response was shifted by a factor of ~10 limiting detection sensitivity in comparison to buffer conditions.

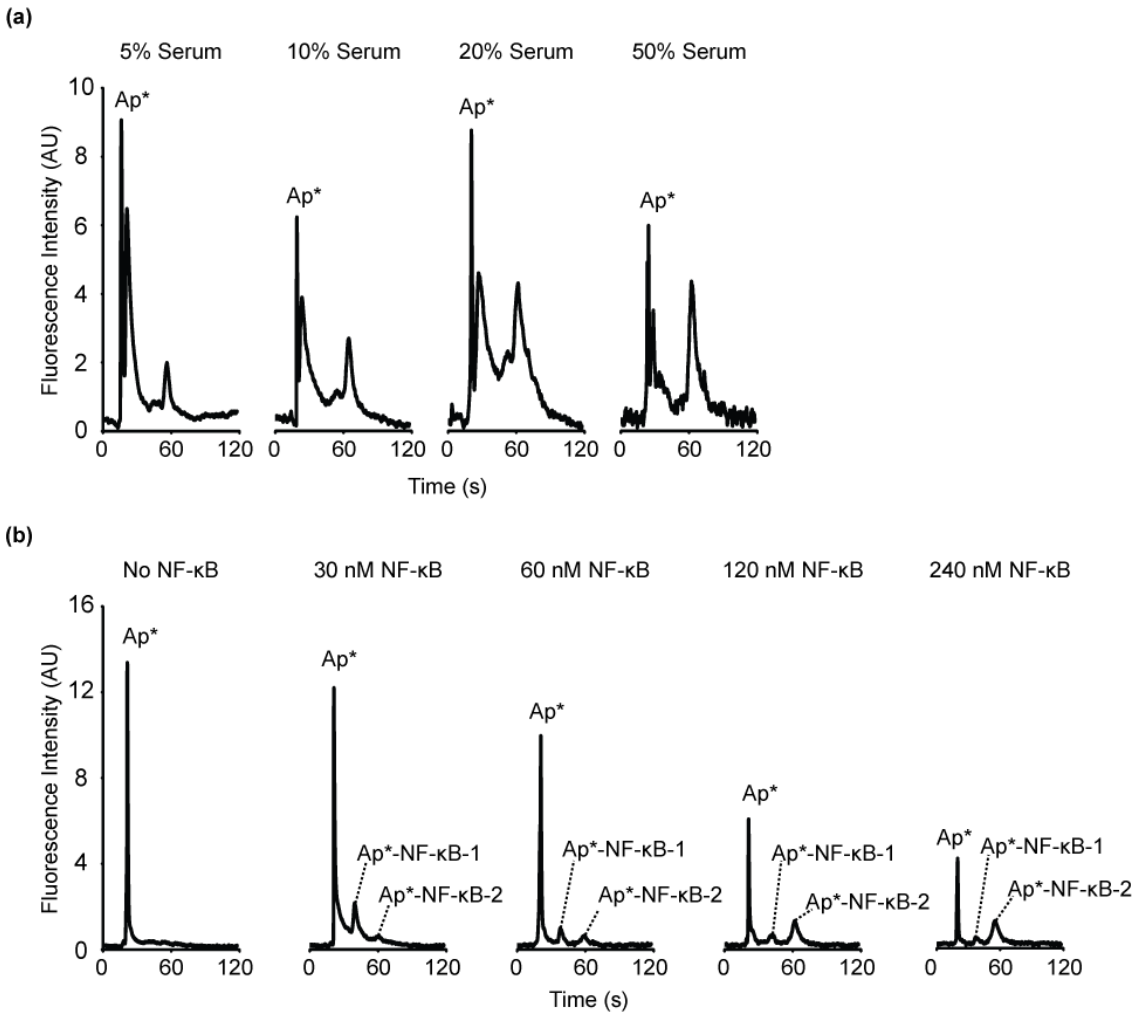

Figure 6.5—Comparison of assay response in serum with and without addition of a competitive suppressing agent. (a) Electropherograms of 60 nM AF647-anti-NF-κB thioaptamer incubated in 5%, 10%, 20% and 50% serum. No NF-κB was added. The peak at 20 seconds represents free aptamer. Significant nonspecific serum protein interference was observed for all serum percentages in the form of multiple peaks at later timepoints. (b) Electropherograms of 60 nM AF647-anti-NF-κB thioaptamer with 1.2 μM of the masking aptamers suppressing non-specific interactions in 10% serum spiked with 0, 30, 60, 120 and 240 nM NF-κB. The free aptamer peak at 20 seconds decreases with increasing serum concentration, as expected. Total area of complex peaks at 40 and 60 seconds increased with higher NF-κB concentration. The ratio of complex at 40 vs. 60 seconds decreased with increasing analyte concentration, possibly associated with NF-κB dimerization or interaction with one or more serum components. The dose-response curve calculated from this data can be found in Figure 6.6.

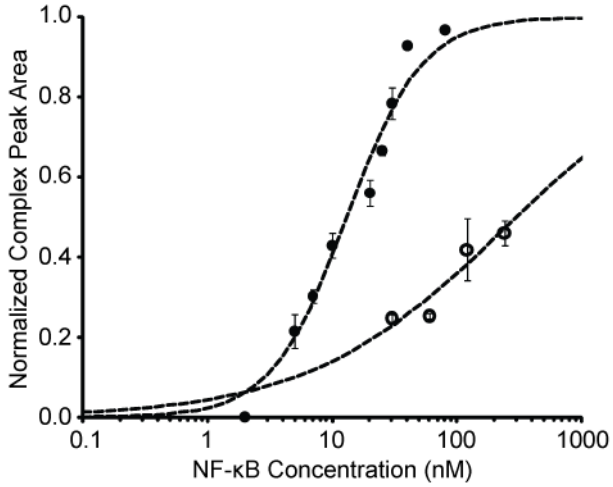

Figure 6.6—Dose response curve for the AF647-anti-NF-κB thioaptamer with NF-κB spiked in buffer (from Figure 6.2b, closed circles, $r^2 = 0.981$) and in 10% serum (open circles, $r^2 = 0.891$).

Preconcentration of Aptamers using a Charged Nanoporous Membrane

In previous work [5, 6], the Sandia group has demonstrated the use of nanoporous polyacrylamide preconcentration membranes to improve the dynamic range and limit of detection of on-chip immunoassays by several orders of magnitude. [9] However, the small size of the aptamers used in this study is comparable to the MW cutoff (~ 10 kDa) of membranes utilized for protein preconcentration. We observed that the aptamer could be concentrated at neutral polyacrylamide membranes, but a measurable fraction of the aptamer tends to penetrate the membrane under even very mild electric field strengths (< 10 V/cm). This results in poor aptamer elution during injection to the separation channel. Aptamer penetration into a neutral membrane and losses during injection are shown in fluorescence micrographs (Figure 6.7a). Instead of a clean injection into the separation channel, a fraction of the concentrated aptamer plug is retained and slowly leaches from the membrane, leading to a smearing of the peak that limits separation resolution and quantitative analysis.

Hlushkou et al [45] developed a thorough theoretical model of electrokinetic enrichment across a charged membrane. They show that the ion-permselectivity of a charged membrane leads to enhanced concentration polarization of ions across the membrane, thereby disrupting the analyte transport near the membrane. Immobilizing negatively charged constituents within preconcentration membranes has previously been shown to impact exclusion of small analytes and we have also found this to be true in earlier evaluations of membrane recipes for integrated electrophoretic applications involving both DNA and proteins. However, recipes have not previously been optimized to facilitate efficient transfer of electrophoretically concentrated analyte into the separation channel without peak distortion. In fact, surface immobilized charge within such membranes is known to induce concentration polarization that interferes with several aspects of preconcentration [6, 45] and also subsequent transfer to a separation channel. [6] Our optimization strategy was based on formulating a high percentage polymer with a modest degree of immobilized charge to exclude DNA while minimizing the polarization expected with a highly acidic membrane. Another concern was whether low solution pH in the immediate vicinity of the membrane may interfere with aptamer/protein binding.

To control membrane acidity, dilute concentrations of acrylamido buffering compounds (Immobilines) were added to the membrane monomer formulation (18.4 mM pK 4.6 Immobiline, 1.6 mM pK 6.2 Immobiline, total solution pH = 4.4). Experimental observation under an epi-fluorescent microscope (Figure 6.7b) revealed that the aptamer stacked against the negatively- charged membrane without translocating across the membrane boundary and cleanly released into the separation channel with no smearing.

To quantify the improvement in preconcentration efficiency with the pH 4.4 membrane in an integrated format, 10 nM AF647-anti-NF-κB thioaptamer in 1% MC was preconcentrated in chips containing both a charged and a neutral membrane. The efficiency of the pH 4.4 membrane was close to optimal based on linear increases of AF647-anti-NF-κB thioaptamer peak areas with respect to preconcentration time (Figure 6.7c) in contrast to an apparent plateau in preconcentration levels at higher preconcentration times with the neutral membrane. (Note that the peak areas in this figure are normalized by the peak area following 30 seconds of preconcentration, whereas complex peak areas in the other figures in this chapter were normalized by the total fluorescence in the electropherogram.) Also critical for integrated preconcentration and separations based analysis is that the mildly charged membrane did not adversely impact reproducibility, peak shapes, elution times or the linearity of enrichment with respect to preconcentration time. No concentration polarization effects were noted with the pH 4.4 membrane under the electric fields used in this work, perhaps due to the continually-flowing buffer solution on the backside of the membrane. However, concentration polarization may be of issue under higher fields or longer preconcentration times. At further extremes of pH, a highly acidic membrane incorporating acrylic acid groups exhibited several symptoms associated with concentration polarization including i) significant drops in current with similar applied electric fields, ii) diffuse collection of labeled aptamer near the membrane during loading or preconcentration, iii) significant smearing of aptamer during injection into the separation channel, and iv) high run to run variability (not shown).

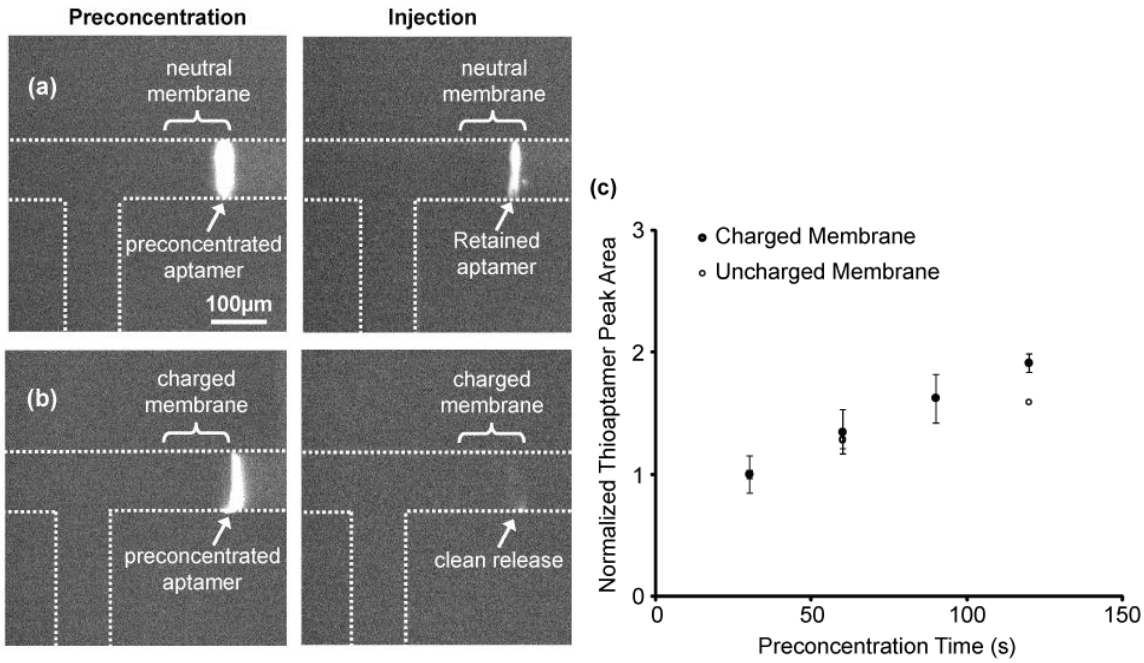

Figure 6.7—Comparison of neutral vs. charged (pH 4.4) preconcentration membrane performance. AF647-anti-NF-κB thioaptamer aptamer loaded to membrane under 10 V/cm for varying preconcentration times. (a) Micrographs of loading and injection of aptamer at neutral membrane. A portion of the preconcentrated aptamer plug penetrates the neutral membrane and slowly elutes during injection, causing smearing of the injected plug. (b) Micrographs of loading and injection of aptamer at charged membrane. Compare clean release in (b) with that in (a). (c) Plot of aptamer peak area following preconcentration at charged (filled circles) vs. neutral (open circles) membranes. Data is normalized by the 30 second preconcentration peak area. The charged membrane produces a linear concentration rate ($r^2 = 0.995$), while the neutral membrane results in a plateau in peak area with increasing preconcentration time ($r^2 = 0.862$). Error bars indicate standard deviations calculated from 3 separate runs.

Integrated Mixing, Preconcentration, Incubation, and Separation

A fully-integrated affinity assay combining on-chip preconcentration, mixing, incubation, and separation was demonstrated using this device incorporating membranes optimized for aptamer exclusion (Figure 6.8). Aptamers proved to be viable as affinity reagents for all steps of the integrated workflow. Fluorescent aptamer was rapidly and efficiently mixed with target sample loaded electrophoretically from separate reservoirs;

representative electropherograms are shown in Figure 6.8a. Although sample concentration of NF-κB was fixed at 20 nM, decreases in free AF647-anti-NF-κB thioaptamer peak area and corresponding increases complex peak areas were achieved by increasing preconcentration times. Normalized complex peak areas increased sigmoidally with preconcentration times as shown in Figure 6.8b, indicating efficient preconcentration, mixing and binding. Incubating reagents at the pH 4.4 membrane did not inhibit complexation of aptamer and target protein. This may occur with more acidic membranes and/or preconcentration conditions inducing significant concentration polarization, but this possibility was not further explored.

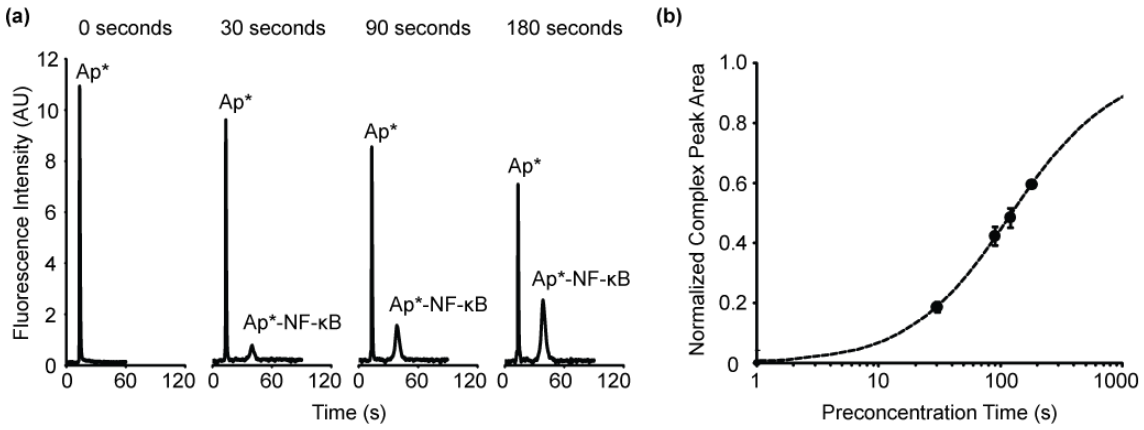

Figure 6.8—Integrated preconcentration and mixing of NF-κB with AF647-anti NF-κB thioaptamer at a charged nanoporous membrane. (a) Electropherograms obtained following 30 second preconcentration of 10nM AF647-anti-NF-κB thioaptamer, followed by 0 to 180 second preconcentration of 20nM NF-κB, and a 60 second buffer incubation/wash. (b) The data from part (a) plotted as normalized complex peak area vs. NF-κB preconcentration time. The normalized complex peak area increases sigmoidally with increasing preconcentration time, illustrating the utility of membrane preconcentration in improving the sensitivity of the detector. Error bars indicate standard deviations calculated from 3 separate runs; $r^2 = 0.999$.

Conclusion

Aptamers are advantageous for gel shift-based lab-on-a-chip applications in point-of-care settings due to their robustness, engineered specificity, stability at a wide temperature range, and superior gel shift properties. This chapter demonstrates successful use of aptamers in an integrated on-chip platform where sample can be preconcentrated, mixed with aptamer and injected into a separation channel for quantitative gel-shift analysis. To achieve quantitative assay results in serum, we also demonstrated significant mitigation of nonspecific interference effects between the thioaptamer and serum components by adding an excess of nonspecific oligonucleotides to the sample and running gel solutions.

This work also presents a basis for optimizing preconcentration membranes to effectively exclude and preconcentrate aptamers without inducing concentration polarization and without localized pH extremes that might interfere with integrated separations analysis. Adding modest amounts of acrylamido buffering components into the polymer matrix to impart a slight negative charge in the membrane enabled successful binding assays following highly efficient preconcentration of aptamer via both size and charge.

Aptamers were first synthesized twenty years ago, and are still developing as diagnostic agents. We anticipate continued progress in aptamer design and synthesis and further incorporation of aptamers into commercial systems due to the inherent benefits of aptamers over conventional antibodies. Combined with the high sensitivity, small analyte consumption, low power requirements, and ease of use of our device, this technology can rapidly provide clinically relevant results in challenging resource-limited

environments — a vast improvement over many current models. The use of aptamers in integrated on-chip electrophoretic molecular recognition assays provides a powerful new avenue for on-chip diagnostics.

Acknowledgments

I would like to thank Greg Sommer, Anson Hatch and Anup Singh of Sandia National Labs for their incredible mentorship, for providing me with the opportunity to participate in this project, and for their tremendous assistance in preparing this chapter. I would like to thank Ross Durland and Xianbin Yang of AM Biotechnologies for providing us with the aptamers and technical support for this project. Aptamer evaluations were supported by NASA SBIR Contract #NNX10CA98C. Microfluidic platform development and integrated diagnostic system was partially supported by the National Institute of Allergies and Infectious Disease Grant U01A1075441 and by Sandia Lab Directed Research and Development Award 09-0856. This research was partially performed under an appointment to the Department of Homeland Security (DHS) Scholarship and Fellowship Program, administered by the Oak Ridge Institute for Science and Education (ORISE) through an interagency agreement between the U.S. Department of Energy (DOE) and DHS. ORISE is managed by Oak Ridge Associated Universities (ORAU) under DOE contract number DE-AC05-06OR23100. All opinions expressed in this chapter are the authors' and do not necessarily reflect the policies and views of DHS, DOE, or ORAU/ORISE. Sandia is a multiprogram laboratory operated by Sandia Corp., a Lockheed Martin Co., for the United States Department of Energy under Contract DE-AC0494AL85000.

References

1. Jokerst, J.V., P.N. Floriano, N. Christodoulides, G.W. Simmons, et al. Integration of semiconductor quantum dots into nano-bio-chip systems for enumeration of CD4+T cell counts at the point-of-need. *Lab On A Chip*, 2008. **8**(12): p. 2079-2090.
2. Kamholz, A.E., B.H. Weigl, B.A. Finlayson, and P. Yager. Quantitative analysis of molecular interaction in a microfluidic channel: The T-sensor. *Analytical Chemistry*, 1999. **71**(23): p. 5340-5347.
3. Lee, H., E. Sun, D. Ham, and R. Weissleder. Chip-NMR biosensor for detection and molecular analysis of cells. *Nature Medicine*, 2006. **14**(8): p. 869-874.
4. Sia, S. and L. Kricka. Microfluidics and point-of-care testing. *Lab Chip*, 2008. **8**: p. 1982-1983.
5. Herr, A.E., A.V. Hatch, D.J. Throckmorton, H.M. Tran, et al. Microfluidic Immunoassays as Rapid Saliva-Based Clinical Diagnostics. *Proc. Natl. Acad. Sci.*, 2007. **104**(13): p. 5268-5273.
6. Hatch, A.V., A.E. Herr, D.J. Throckmorton, J.S. Brennan, et al. Integrated Preconcentration SDS-PAGE of Proteins in Microchips Using Photopatterned Cross-Linked Polyacrylamide Gels. *Anal. Chem.*, 2006. **78**: p. 4976-4984.
7. Herr, A.E. and A.K. Singh. Photopolymerized Cross-Linked Polyacrylamide Gels for On-Chip Protein Sizing. *Anal. Chem.*, 2004. **76**: p. 4727-4733.
8. Herr, A.E., D.J. Throckmorton, A.A. Davenport, and A.K. Singh. On-Chip Native Gel Electrophoresis-Based Immunoassays for Tetanus Antibody and Toxin. *Anal. Chem.*, 2005. **77**: p. 585-590.
9. Meagher, R.J., A.V. Hatch, R.F. Renzi, and A.K. Singh. An Integrated Microfluidic Platform for Sensitive and Rapid Detection of Biological Toxins. *Lab Chip*, 2008. **8**: p. 2046-2053.
10. Renzi, R.F., J. Stamps, B.A. Horn, S. Ferko, et al. Hand-held microanalytical instrument for chip-based electrophoretic separations of proteins. *Analytical chemistry*, 2005. **77**(2): p. 435.
11. Boschek, C.B., D.O. Apiyo, T.A. Soares, H.E. Engelmann, et al. Engineering an ultra-stable affinity reagent based on Top7. *Protein Engineering, Design and Selection*, 2009. **22**(5): p. 325-332.
12. Ligler, F.S. and C.R. Taitt, eds. *Optical biosensors: today and tomorrow*. 2nd ed. 2008, Elsevier: Amsterdam, The Netherlands.
13. Brody, E.N. and L. Gold. Aptamers as therapeutic and diagnostic agents. *Reviews in Molecular Biotechnology*, 2000. **74**(1): p. 5-13.
14. Klussmann, S., ed. *The aptamer handbook: functional oligonucleotides and their applications*. 2006, Wiley-VCH: Weinheim, Germany. 490.

15. Ellington, A.D. and J.W. Szostak. In vitro selection of RNA molecules that bind specific ligands. *Nature*, 1990. **346**: p. 818-822.

16. Li, Y., L. Guo, F. Zhang, J. Tang, et al. High-sensitive determination of human α-thrombin by its 29-mer aptamer in affinity probe capillary electrophoresis. *Electrophoresis*, 2008. **29**: p. 2570-2577.

17. Ferapontova, E.E., E.M. Olsen, and K.V. Gothelf. An RNA aptamer-based electrochemical biosensor for detection of theophylline in serum. *J. Am. Chem. Soc.*, 2008. **130**: p. 4256-4258.

18. McCauley, T.G., N. Hamaguchi, and M. Stanton. Aptamer-based biosensor arrays for detection and quantification of biological amcromolecules. *Anal. Biochem.*, 2003. **319**: p. 244-250.

19. Lai, R.Y., K.M. Plaxco, and A.J. Heeger. Aptamer-based electrochemical detection of picomolar platelet-derived growth factor directly in blood-serum. *Anal. Chem.*, 2007. **79**: p. 229-233.

20. Fine, S.L., D.F. Martin, and P. Kirkpatrick. Pegaptanib sodium. *Nature Reviews Drug Discovery*, 2005. **4**: p. 187-188.

21. Leary, J.F., L.M. Reece, X. Yang, and D.G. Gorenstein. *Proc. Soc. Photo-Opt. Instr. Eng*, 2005(5692): p. 216-223.

22. Yang, X. and D.G. Gorenstein. Progress in thioaptamer development. *Curr Drug Targets*, 2004. **5**(8): p. 705-15.

23. Yang, X., X. Li, T.W. Prow, L.M. Reece, et al. Immunofluorescence assay and flow-cytometry selection of bead-bound aptamers. *Nucleic Acids Res*, 2003. **31**(10): p. e54.

24. Bassett, S.E., S.M. Fennewald, D.J. King, X. Li, et al. Combinatorial selection and edited combinatorial selection of phosphorothioate aptamers targeting human nuclear Factor-kappa B RelA/p50 and RelA/RelA. *Biochemistry*, 2004. **43**(28): p. 9105-9115.

25. Yang, X., S.E. Bassett, X. Li, B.A. Luxon, et al. Construction and selection of bead-bound combinatorial oligonucleoside phosphorothioate and phosphorodithioate aptamer libraries designed for rapid PCR-based sequencing. *Nucl. Acids Res.*, 2002. **30**(23): p. e132-.

26. King, D.J., S.E. Bassett, X. Li, S.A. Fennewald, et al. Combinatorial selection and binding of phosphorothioate aptamers targeting human NF-κB RelA(p65) and p50. *Biochemistry*, 2002. **41**: p. 9696-9706.

27. Jayasena, S.D. Aptamers: An emerging class of molecules that rival antibodies in diagnostics. *Clinical Chemistry*, 1999. **45**(9): p. 1628-1650.

28. Wiegand, T.W., P.B. Williams, S.C. Dreskin, M.-H. Jouvin, et al. High-affinity oligonucleotide ligands to human IgE inhibit binding to Fcε receptor I. *J. Immunology*, 1996. **157**: p. 221-230.

29. Volk, D.E., X. Yang, S.M. Fennewald, D.J. King, et al. Solution structure and design of dithiophosphate backbone aptamers targeting transcription factor NF-kappaB. *Bioorg Chem*, 2002. **30**(6): p. 396-419.

30. Yang, X.B., S. Fennewald, B.A. Luxon, J. Aronson, et al. Aptamers containing thymidine 3 '-O-phosphorodithioates: Synthesis and binding to nuclear factor-kappa B. *Bioorganic & Medicinal Chemistry Letters*, 1999. **9**(23): p. 3357-3362.

31. Gould, H.J., B.J. Sutton, A.J. Beavil, R.L. Beavil, et al. The biology of IgE and the basis of allergic disease. *Annual Review Of Immunology*, 2003. **21**: p. 579-628.

32. Sutton, B.J. and H.J. Gould. The Human Ige Network. *Nature*, 1993. **366**(6454): p. 421-428.

33. Baldwin, A.S. The NF-kappa B and I kappa B proteins: New discoveries and insights. *Annual Review Of Immunology*, 1996. **14**: p. 649-683.

34. Gilmore, T.D. The Rel/NF-kappa B signal transduction pathway: introduction. *Oncogene*, 1999. **18**(49): p. 6842-6844.

35. Dolcet, X., D. Llobet, J. Pallares, and X. Matias-Guiu. NF-kB in development and progression of human cancer. *Virchows Archiv*, 2005. **446**(5): p. 475-482.

36. Mann, D.A. and F. Oakley. NF-κB: a signal for cancer. *J. Hepatology*, 2005. **42**(4).

37. Fischer, N.O., T.M. Tarasow, and J.B.H. Tok. Protein detection via direct enzymatic amplification of short DNA aptamers. *Analytical Biochemistry*, 2008. **373**(1): p. 121-128.

38. Pavski, V. and X.C. Le. Detection of Human Immunodeficiency Virus Type 1 Reverse Transcriptase Using Aptamers as Probes in Affinity Capillary Electrophoresis. *Analytical Chemistry*, 2001. **73**(24): p. 6070-6076.

39. Zhang, H., X.-F. Li, and X.C. Le. Tunable Aptamer Capillary Electrophoresis and Its Application to Protein Analysis. *Journal of the American Chemical Society*, 2007. **130**(1): p. 34-35.

40. Tang, J., T. Yu, L. Guo, J. Xie, et al. In vitro selection of DNA aptamer against abrin toxin and aptamer-based abrin direct detection. *Biosensors and Bioelectronics*, 2007. **22**(11): p. 2456-2463.

41. Haes, A.J., B.C. Giordano, and G.E. Collins. Aptamer-Based Detection and Quantitative Analysis of Ricin Using Affinity Probe Capillary Electrophoresis. *Analytical Chemistry*, 2006. **78**(11): p. 3758-3764.

42. Sommer, G.J., A.K. Singh, and A.V. Hatch. On-Chip Isoelectric Focusing Using Photopolymerized Immobilized pH Gradients. *Anal. Chem.*, 2008. **80**: p. 3327-3333.

43. German, I., D. Buchanan, and R. Kennedy. Aptamers as Ligands in Affinity Probe Capillary Electrophoresis. *Anal. Chem.*, 1998. **70**: p. 4540-4545.

44. Baud, M., *Data Analysis, Mathematical Modeling*, in *Methods of Immunological Analysis*, R. Masseyeff, Editor. 1993, VCH Publishers, Inc.: New York, NY. p. 656-671.

45. Hlushkou, D., R. Dhopeshwarkar, R.M. Crooks, and U. Tallarek. The influence of membrane ion-permselectivity on electrokinetic concentration enrichment in membrane-based preconcentration units. *Lab on a Chip*, 2008. **8**(7): p. 1153-1162.

Chapter 7

Summary and Future Directions

Summary

This dissertation has demonstrated the ability to use the magnetorotation of superparamagnetic microbeads as a signal transduction method for measuring the concentration of a protein in solution. Two main versions of the method were shown: Label-Acquired Magnetorotation (LAM), where the attachment of 1 μm superparamagnetic beads to 10 μm mother spheres was mediated by the target protein; and Bead Assembly Magnetorotation (BAM), where the gravity- and magnetism-driven formation of 1 μm superparamagnetic bead assemblies in an inverted droplet was mediated by the target protein. BAM was shown to be the more sensitive of the two methods, with a limit of detection (LOD) of 80 fM, versus 300 pM for LAM. The LOD for BAM is one of the lowest LODs ever reported for the thrombin-aptamer pair; in a survey of twenty other signal transduction methods reported for the thrombin-aptamer pair, this LOD was lower than all but one, which is significantly more complex and time consuming.

Chapter 2 described the initial development of LAM, and demonstrated its proof-of-principle by using biotin-coated particles as the analyte mimics and streptavidin as the affinity molecule mimic. Mother spheres could acquire rotation with as few as two

daughter beads attached to them, and the rotational frequency of mother spheres increased linearly with the number of attached daughter beads. This chapter introduced the concept of using magnetic beads as analyte labels, attaching them to a larger sphere, and then achieving rotating of the resulting complex. The rotation of a mother sphere was shown to be stable for over sixty minutes. This chapter demonstrated the feasibility of magnetorotation as a signal transduction mechanism.

Chapter 3 expanded on the initial development of LAM, in chapter 2, demonstrating the performance of LAM with a real protein and affinity molecule pair, thrombin and its aptamers. This was the first time that magnetorotation was shown to work as a signal transduction mechanism for the detection of a protein. The LOD for this experiment was 300 pM, although computer simulations indicated that there was potential for improvement within this system.

Chapter 4 described the development of BAM, the second iteration of LAM. This method of bead assembly proved to be much more sensitive than its predecessor, with an LOD of 80 fM, i.e. over three orders of magnitude better than LAM. The reproducibility of BAM was also much better than LAM. In addition to magnetorotation, fractal analysis of images of the bead clusters proved to be an effective signal transduction mechanism. A simple laser-and-photodiode system proved to be an effective set-up for the detection of magnetorotation without the use of a microscope, as a possible prototype for a portable detection system.

Chapter 5 highlighted the challenges faced when trying to transfer the operation of a thrombin-based BAM into serum. The nonspecific interactions between the serum proteins and the bead surfaces were partially mitigated by functionalizing the bead

surfaces with PEG, although nonspecific interactions between the serum proteins and the aptamers were still a problem. Additionally, the partial collapse upon rotation of bead assemblies that include PEG was an additional unexpected setback. These issues combined to result in BAM having an LOD in serum four orders of magnitude lower and with worse vertical resolution than in serum. Despite these problems, BAM still had an LOD close to the lowest values reported for thrombin aptamers in serum, suggesting that, due to the fact that they were initially developed for therapeutic, not diagnostic, applications, the thrombin aptamers themselves might be ill suited for use in serum.

Chapter 6 demonstrated the use of aptamers as affinity reagents in a capillary electrophoresis detection system. The aptamers were shown to be advantageous relative to antibodies for capillary electrophoresis detection applications, because their smaller molecular weight resulted in better resolution between the free aptamer peak and the complex peak. The analyte for these experiments was the nuclear transcription factor NF-κB. Problems of nonspecific interference from serum components were mitigated by the use of excess nonspecific aptamer to compete for serum binding sites. Also, the use of an on-chip preconcentration membrane was shown to result in improved detection sensitivity.

Future Directions

The most immediate future direction for this project would be the incorporation of antibodies against clinically relevant biomarkers. While aptamers have several advantages as affinity molecules, they also have two primary disadvantages. The first is that while aptamers are very simple and inexpensive to produce, their initial development

is a very labor- and time-intensive process, and due to various intellectual property issues surrounding them, very few aptamers are available for clinically relevant analytes. Thus the thrombin aptamers used in this dissertation, as well as by the many comparison papers, were not optimized for avoiding non-specific interference from serum molecules. The second is that because they are naturally produced in the bloodstream, antibodies tend to be better at avoiding nonspecific serum interactions. Some possible clinically relevant sandwich antibody-analyte pairs that could be incorporated into BAM include PSA, CEA, CA125, cMb, and Hsp72.

However, there are several issues that are significant for considering the future of this technology. The first is the collapse of the PEG-functionalized assemblies used to mitigate the nonspecific binding of serum to the beads, under the effects of the rotating magnetic field. PEG is the primary surface coating molecule that is used to protect micro- and nano-scale surfaces from biofouling from molecules such as serum proteins. Its unsuitability for BAM necessitates identifying additional candidate molecules that could be used to allow for the performance of BAM in serum.

The second, and perhaps more critical issue to be addressed, in terms of long-term clinical applicability of this technology, is the landscape of competing technologies. Within the field of magnetic particle-based diagnostics, work in magnetic relaxation (MR) from the Weissleder group and work in giant magnetoresistance (GMR) from the Wang group represent extremely formidable competitors. They have achieved femtomolar-level detection, in serum, using clinically-relevant antibodies, in rapid, compact, portable formats. While it is certainly possible that, with additional improvements to BAM, it could reach comparable LODs, it seems unlikely that it could

surpass them. Those two techniques have been under development for a much longer period of time, and with a much greater amount of resources at their disposal, compared to the BAM technique; they are simply further along in their development. Additionally, the low femtomolar range is the floor of clinically-relevant concentrations of most biomarkers, so even if a more sensitive device could be developed, its application would be limited to only a few special cases.

In conclusion, this dissertation has demonstrated the development of bead assembly magnetorotation as a signal transduction mechanism, performed with either rotational period analysis or with fractal image analysis, with a portable laser-and-photodiode detection setup, giving a very low LOD for thrombin in buffer, and includes a discussion on strategies for and the challenges of performing BAM in serum.

Appendix A

Performance of BAM in Larger Hanging Droplets

The BAM experiments discussed in Chapters 4 and 5 all featured 1 μL inverted droplets placed in the 1.5 mm wells on Teflon-coated glass slides. However, we believe that the LOD could be significantly decreased by using larger droplets. There is a minimum number of beads in solution (about 500) needed to create an assembly large enough to produce a useful signal, and, as shown in Table 4.1, the number of thrombin molecules per bead at the limit of detection is relatively constant. Therefore, there is an absolute minimum number of thrombin molecules (roughly 500 beads x 150 thrombin molecules/bead = 75,000 molecules) in a droplet necessary for a detection event to occur. Since, for a given thrombin concentration, the number of thrombin molecules per droplet increases linearly with the volume of the droplet, we would expect that the LOD would decrease with inverse linear proportionality to the volume of the droplet, so that, for example, if we were able to perform BAM in a 10 μL droplet, we would expect to see a 10-fold decrease in the LOD.

We attempted to create larger droplets that would be stable enough to perform BAM, but, unfortunately, these attempts were not successful. The primary challenge in creating and using the larger droplets was the appearance of convection currents that were persistent in the droplet, which disrupted the formation of the bead assemblies. The

currents could be seen by the movement of beads in the droplet. These currents occurred in droplets ranging from as small as 2 μL to as large as 50 μL.

Experimental

Several strategies were explored to mitigate the effects of the currents on the droplets by stabilizing them. We attempted to immerse the droplets in silicone oil, but a combination of the gravity and the hydrophobic nature of both the aptamers and the native bead surface resulted in the beads breaking through the oil-water interface. We attempted to place a biologically inert cellulose dialysis membrane at the oil-water interface, but the beads stuck to the membrane. As a final strategy we attempted to add glycerol to the droplets to increase their viscosity and stabilize them. We examined four different droplet sizes, 2.3 μL, 4.6 μL, 8.0 μl and 12.7 μL, which were formed on Teflon-coated glass slides of four different sizes, 2 mm, 2.5 mm, 3 mm, and 3.5 mm. The volumes were chosen so as to keep to same droplet shape factor as was present in the original experiments. Four different glycerol concentrations were examined, 0.01%, 0.1%, 1% and 10%, in the same thrombin binding buffer as discussed in chapters 3, 4 and 5. A glycerol-free buffer solution was used as a control. The droplets were prepared according to the procedure given in the Materials and Methods section of Chapter 4. A series of images, one from each set of droplets, is shown in Figure A.1 below.

Results and Discussion

Figure A.1 shows a series of images of the droplets formed in glycerol solutions. Based on these images, it appears that the glycerol solutions were not effective in mitigating the convection currents in the droplets. Although there does not appear to be a specific pattern in the types of currents that form, the currents seem to be more pronounced in the 8.0 μL and 12.7 μL droplets. The 12.7 μL droplets with 10%, 1% and 0.1% glycerol appear to show cases where the currents have the most pronounced effects. In all cases, the convection currents prevented the beads from forming stable assemblies at the bottom of the droplets.

It appears that in order to attempt to perform BAM in larger droplets, a strategy to mitigate the presence of convection currents in these droplets would need to be developed. Immersing the droplets in oil, with or without a membrane, prevents the formation of assemblies, and the addition of glycerol to the solutions does not appear to prevent convection currents from disrupting the formation of bead assemblies at the bottom of the droplets.

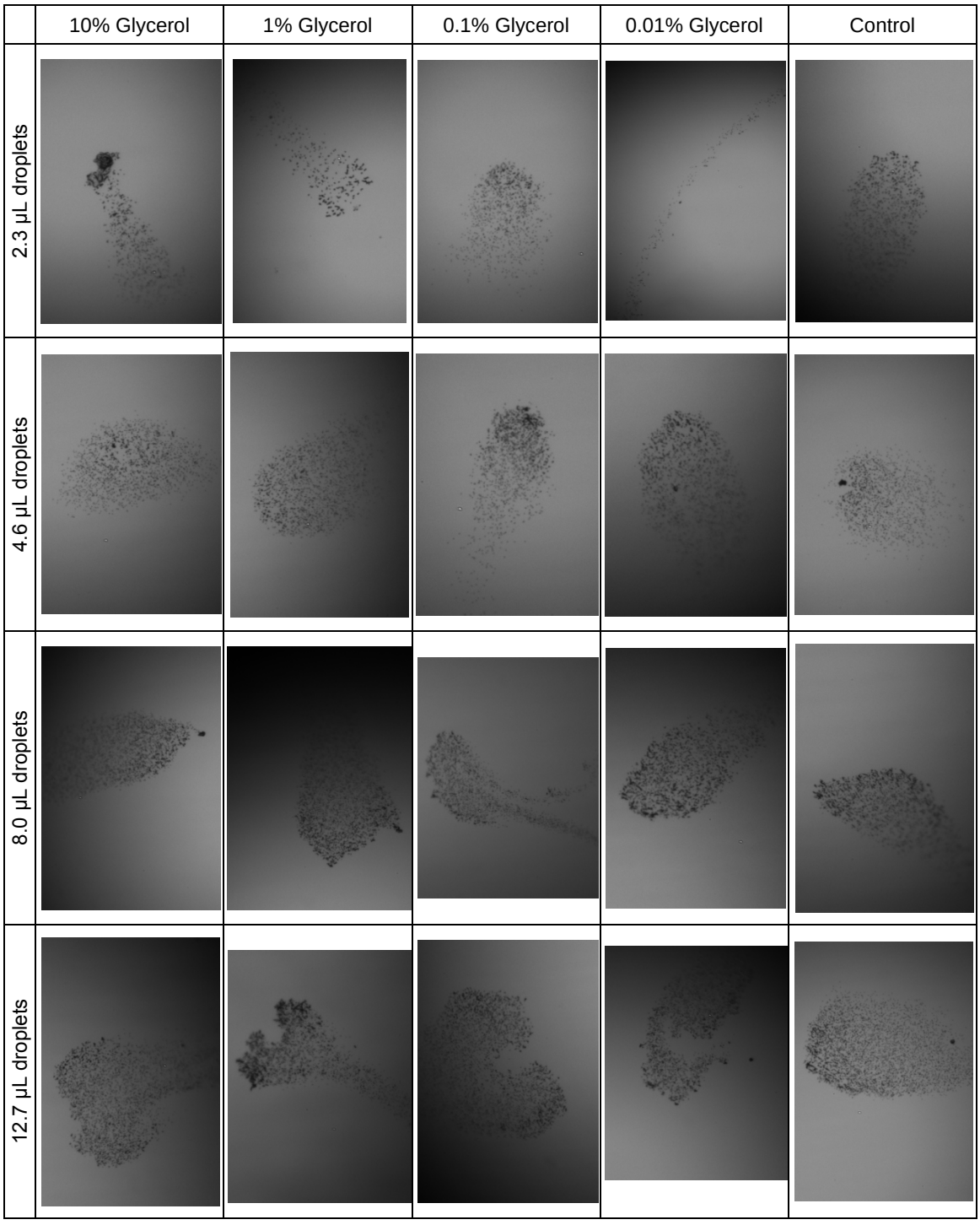

Figure A.1—A collection of images from four different droplet sizes (2.3 µL, 4.6 µL, 8.0 µL and 12.7 µL), with five different glycerol concentrations (0.01%, 0.1% 1% and 10%, plus glycerol-free buffer control), illustrating the presence of convection currents in the larger droplets. The bead assemblies should be in a tightly-packed circular arrangement. As the bead assemblies move under the influence of the convection currents, they tend to develop a head and a tail region, which is seen in all of the images.

Appendix B

Calculation of Nearest-Neighbor Bead Angles and Assembly Radius of Gyration as Potential Signal Transduction Methods

In Chapter 4, we showed three different signal transduction methods for BAM: magnetorotation, fractal dimension, and lacunarity. While these three methods worked well, we wanted to explore whether there might be additional methods by which we could measure a property of the bead assembly that would correlate well with the thrombin concentration. We chose to examine two potential methods: calculating the angle between each bead in the assembly and its adjacent neighbors, and calculating the angle of gyration of the assembly as a whole.

Experimental

The work here was performed with a computer analysis of previously collected experimental data. The experimental data used here is the 22 μg/mL bead concentration (all thrombin concentrations) dataset from Chapter 4 that was used for the fractal dimension and lacunarity calculations. The images used were collected at 20x and 40x magnifications. The computer program used to perform the calculations and analysis here was written in MATLAB, and is included in Appendix C-3.

The first step in performing this analysis was to write a program that would identify the position of each bead within the projected image; once the coordinates of each bead were identified, further analysis could be performed. To identify the center of each bead, we took advantage of the fact that, in the 2-dimensional projected images, due to the way the bead scatters light, the center of each bead was brighter than its edges. For each pixel, which will be referred to here as "pixel zero," its intensity was compared to that of its eight adjacent neighbors (including diagonals). If the intensity of the pixel zero was greater than 7 of its 8 neighbors, it was passed on to the second stage of analysis. In the second stage, the 16 pixels neighboring the first eight pixels (so the next-nearest neighbors from pixel zero) were examined, and if pixel zero had an intensity greater than 15 out of the 16 next-nearest pixels, then pixel zero was determined to be the center of the bead. As the final test, since each bead had a diameter of approximately 12-14 pixels (40x magnification) or 6-7 pixels (20x magnification), for a pixel to be considered the center of a bead, there could be no overlapping bead centers with a diameter of 12-14 (or 6-7) pixels (the exact radius of exclusion was individually tuned to each image, in part due to the effects of the curvature of the droplet on creating some three-dimensional behavior within the assembly).

The nearest-neighbor angle calculations were performed by finding all the beads within a distance of 1.1 times (to allow for slight errors in calculating the average center of the beads) the average diameter of each bead, and calculating all combinations of possible angles between the central bead and the adjacent beads. The angle was determined by calculating the distance between the beads, and then applying the law of cosines to calculate the angle *C*, as shown in Eq. B.1 below, where *a, b* and *c* are the

distances between each of the three beads.

$$C = \cos^{-1}\left(\frac{a^2 + b^2 - c^2}{2ab}\right) \tag{B.4}$$

Based on the results shown in Figure 4.4, since at high protein concentration the fractal dimension of the assembly is approximately 1.7, the same as that of a diffusion limited aggregate (DLA) [1], our hypothesis was that the angular distribution of the bead assembly should be the same as that of a DLA. To test this hypothesis, we created a 1000-bead DLA simulation with full range of motion (beads not confined to moving in discrete steps along a square lattice), for comparison of the angular distribution with the experimental data.

The radius of gyration, R_g, [2] of each assembly was calculated from the formula in Equation B.2 below, where r_k is the position of each bead and r_{mean} is the center of mass of the assembly of N beads.

$$R_g^2 = \frac{1}{N}\sum_{k=1}^{N}\left(r_k - r_{\text{mean}}\right)^2 \tag{B.5}$$

Results and Discussion

A series of images of bead assemblies, and the positions of three bead assemblies (100 fM, 1 pM and 10 pM at a bead concentration of 22 μg/mL), as determined by the MATLAB program, are shown below in Figure B.1.

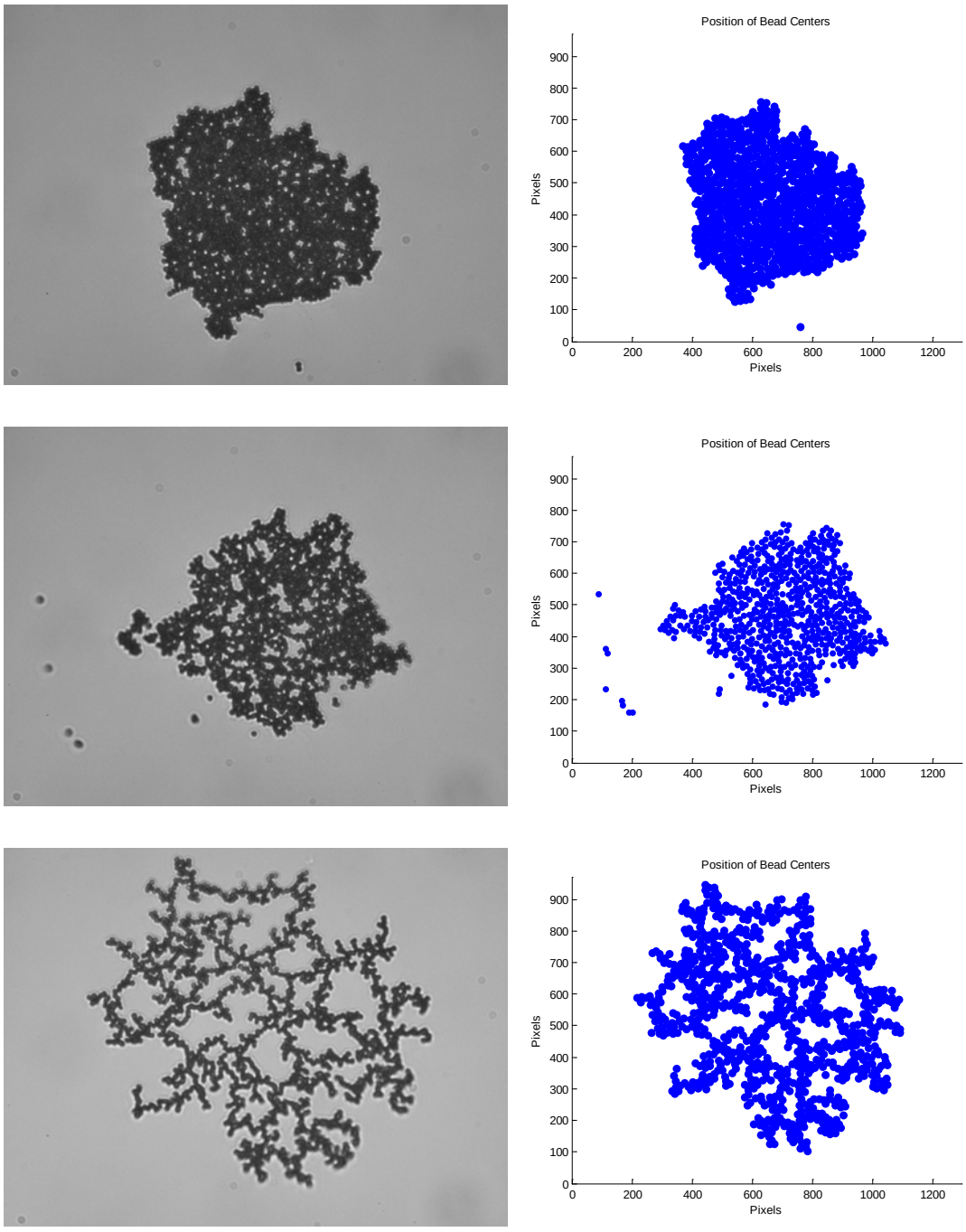

Figure B.1—Images of 22 μg/mL bead assemblies (at 40x magnification) at three different thrombin concentrations: 100 fM (top), 1 pM (middle) and 10 pM (bottom).

Based on the program that calculates the position of each bead in the assembly, the nearest-neighbor angular distribution for nine assemblies of different thrombin

concentrations, ranging from 100 fM to 46 pM, were calculated and plotted on a histogram, as shown in Figure B.2 below. This figure does not show any significant trend across the plots, other than perhaps a slight increase in the relative size of the peak at 60 degrees as the thrombin concentration increases. We had expected to see a peak in the distribution at 180 degrees, and decreasingly monotonically to 60 degrees, which is clearly not present in these images. However, such a trend could be seen in the DLA angle distribution, as shown in Figure B.3 below.

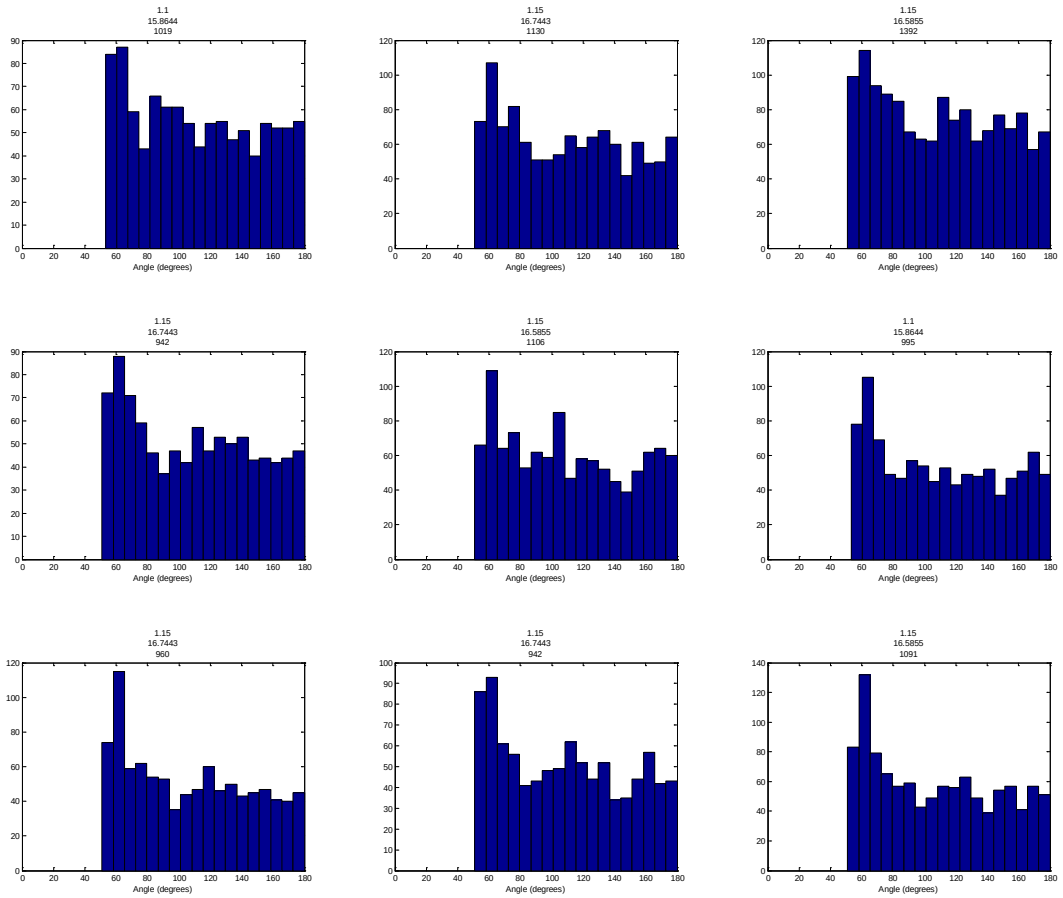

Figure B.2—A series of histograms showing the distribution of adjacent nearest-neighbor beads within nine bead assemblies of varying thrombin concentrations at 22 μg/mL bead concentrations: 100 fM, 216 fM and 464 fM (left to right, top row), 1 pM, 2.16 pM and 4.64 pM (left to right, middle row), 10 pM, 21.6 pM and 46.4 pM (left to right, bottom row).

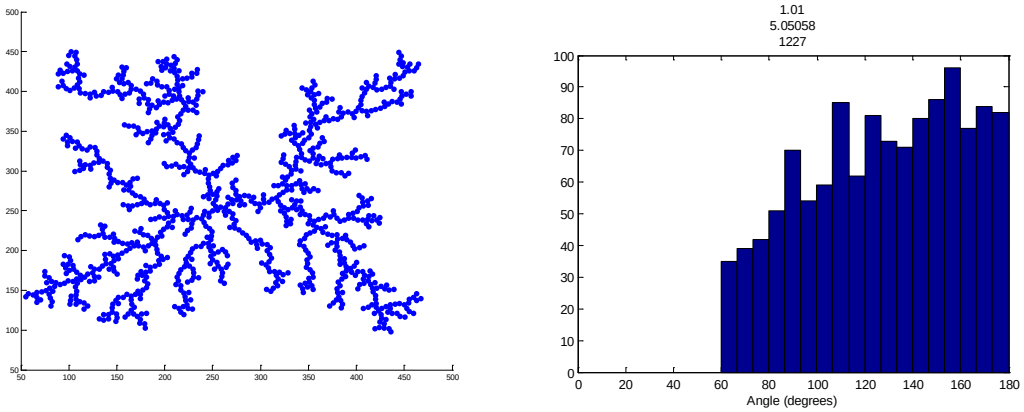

Figure B.3—The result of a 1000 bead DLA simulation (left). The distribution of nearest-neighbor bead angles from the 1000 bead DLA simulation (right).

Additionally, the data in Figure B.3 shows the distribution that we had expected: a maximum near 180 degrees, decreasing monotonically down to 60 degrees. This distribution is significantly different from those shown in Figure B.2. This suggests that our bead assemblies have at least some characteristics that differ from those of DLAs.

The radius of gyration of bead assemblies of nine different thrombin concentrations, as measured in pixels, were calculated, and are shown in Figure B.4 below.

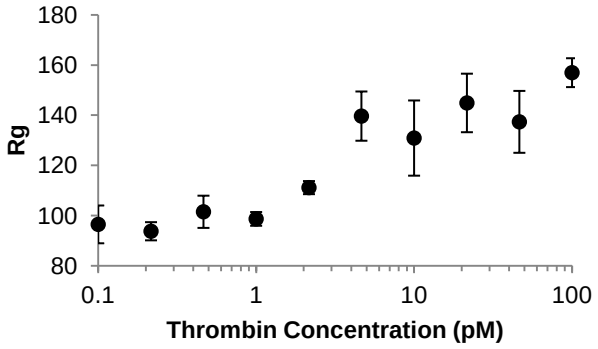

Figure B.4—Plot of the average radius of gyration (± SD) of bead assemblies at ten different thrombin concentrations (each point represents the average of four measurements).

While the plot in Figure B.4 shows the expected trend, an increase in radius of gyration with increasing thrombin concentration, there is a lot more error in the data than was expected. Compared to the plots for fractal dimension and lacunarity, this data appears to be much noisier, and does not appear to fit well to the shape of a logistic curve. In conclusion, it appears that, compared to magnetorotation, fractal dimension and lacunarity, the nearest-neighbor bead angular distribution and radius of gyration do not appear to sufficiently robust signal transduction mechanisms.

Acknowledgments

I would like to thank Visiting Professor Panos Argyrakis of the University of Thessaloniki in Greece for his assistance in the development of the concepts and principles discussed in this appendix.

References

1. Witten, T.A., Jr. and L.M. Sander. Diffusion-Limited Aggregation, a Kinetic Critical Phenomenon. *Physical Review Letters*, 1981. **47**(19): p. 1400-1403.
2. Fixman, M. Radius of Gyration of Polymer Chains. II. Segment Density and Excluded Volume Effects. *The Journal of Chemical Physics*, 1962. **36**(12): p. 3123-3129.

Appendix C

MATLAB Computer Codes

C-1

Code for Calculating the Rotational Frequency of a Sandwich Complex

```
function rotational_frequency

%*********************************************************
%INSTRUCTIONS
%*********************************************************
%1. Copy and paste this file into the same folder as the data
%2. Make sure the data file is a .txt file
%3. Enter the file name below where it says M(:,2)=csvread('*.txt');
%4. Enter the frame rate (in frames per second) right below that
%5. Run the program
%6. Output is rotational frequency in mHz
%7. If the results don't look good, tweak the cutoff and threshold
values
%below.

%This version modified on 7/21/2010 to turn the iterations into a
proper
%while loop and to recalculate the cook's distance based on the final
data
%set.

%*********************************************************
%FILE INPUT AND PARAMETERS
%*********************************************************
%This is where you input the text file with the angles
M(:,2)=csvread('1.4 amp 1.txt');

%x is the frame rate (in fps)
x=50;

%cutoff is the fraction of the standard deviation above the median for
%which influential points will be discarded
cutoff=0.5;
```

```
%threshold is the largest value for delta for which we will try to
remove
%points. If the delta does not exceed the threshold, then no more
points
%will be removed. The units of the threshold is degrees. The default
%setting of the threshold is +/- 2%.
threshold=0.02*360;

%If intermediate is set equal to 1, then the plots of the each
iteration
%will be shown. If intermediate is set equal to 0, then the plots of
each
%iteration will not be shown.
intermediate=0;

%************************************************************
%PROCESSING THE RAW DATA
%************************************************************

%len is the length of the matrix
len=length(M);

%x is the frame rate in fps. This line inserts the time stamp for each
%point based on the frame rate
M(:,1)=(0:1/x:1/x*(len-1));
%N is the new matrix with the zero values removed. The x-values (time)
are
%in column 1. The y-values (angle) are in column 2.

N=[];
for i=1:len
   if M(i,2)~=0;
       N(end+1,:)=M(i,:);
   end
end

time=N(end,1);
%This fits a linear line to the values in N. p(1) is the slope of the
line.
%p(2) is the y-intercept
%S contains error information for the polyval function
[p S]=polyfit(N(:,1),N(:,2),1);

%polyval evaluates the polynomial. p is the polynomial. N(:,1) are the
%x-values at which we will evaluate the polynomial.
%y is the the polynomial p evaluated at points N(:,1). This means that
y is
%the y-values for the best-fit line of the data.
%delta is the limit of the confidence region. To plot error bands, plot
%y+delta and y-delta
[y,delta]=polyval(p,N(:,1),S);
delta_mat(1)=delta(1);

%r_squared is the calculation of the R^2 value for the fitted line.
r_squared=sum((y-mean(N(:,2))).^2)/sum((N(:,2)-mean(N(:,2))).^2);
```

```
% %plots both the raw data points, and the best fit line. The data
points are
% %in blue dots, the line is black. The confidence lines are in red.
subplot(2,3,1),
plot(N(:,1),N(:,2),'.',N(:,1),y,'k',N(:,1),y+delta,'r',N(:,1),y-
delta,'r')
xlabel('Time (sec)')
ylabel('Degrees')
title('Raw Data')
axis([0 time 0 500])
%Preserve the N matrix by copying it into the R matrix, for use later
on.
R=N;
freq=p(1)/(360)*1000;
freq_mat(1)=freq;
%original_size is the number of points in the original data set, before
we
%start removing points based on Cook's Distance
original_size=length(N);

%*************************************************************
%ANALYZING THE RESULTS TO REMOVE OUTLIERS THROUGH COOK'S DISTANCE
%*************************************************************

%Counter counts the number of iterations the program runs through
%N is the matrix of values that enters the loop. The points that are
%preserved are written in the matrix Q. The original N is then erased,
and
%Q becomes the new N. Therefore, N and Q are erased and rewritten every
%time the loop runs. The final set of data points is Q.

counter=0;
while delta>threshold
    counter=counter+1;
%This is the correct formula for the hat matrix. Confirmed through R. X
is
%the matrix of X values
X=N(:,1);
hat=X*inv(X.'*X)*X.';
% Sigma is the deviation. N(:,2) is the actual data points. y is the
fitted
% data points based on a linear regression. This is for 1 degree of
% freedom.
sigma=sqrt(sum((N(:,2)-y).^2)/(length(N)-2));
%epsilon is the residuals
epsilon=N(:,2)-y;
%r_stud is the studentized residuals
r_stud=epsilon./(sigma*sqrt(1-(diag(hat))));
%jack is the jackknife residuals
jack=r_stud.*sqrt((length(N)-2)./(length(N)-1-r_stud.^2));
%cook is the Cook's Distance, which measures the influence of a point
on
%the regression
cook=1/1*r_stud.^2.*(diag(hat)./(1-diag(hat)));
%For 148 points, and alpha = 0.05, Bonf criteria = -3.67
```

```
%For 148 points, and alpha = 0.1, Bonf criteria = -3.47
%subplot(2,4,5), plot(jack,'.')
%This plots the Cook's Distance of the first iteration
if counter==1;
subplot(2,3,4),
plot(N(:,1),cook,'.',(0:1/x:max(N(:,1))),median(cook)+cutoff*std(cook),
'k--')
xlabel('Time (sec)')
ylabel('Cooks Distance')
end
%This plots the Cook's Distance of the final iteration
subplot(2,3,5),
plot(N(:,1),cook,'.',(0:1/x:max(N(:,1))),median(cook)+cutoff*std(cook),
'k--')
xlabel('Time (sec)')
ylabel('Cooks Distance')

%plots the results of each interation. this occurs only if intermediate
=
%1;
if intermediate==1;
    figure

subplot(1,2,1),plot(N(:,1),N(:,2),'.',N(:,1),y,'k',N(:,1),y+delta,'r',N
(:,1),y-delta,'r')
    xlabel('Time (sec)')
    ylabel('Degrees')

subplot(1,2,2),plot(N(:,1),cook,'.',(0:1/x:max(N(:,1))),median(cook)+cu
toff*std(cook),'k--')
    xlabel('Time (sec)')
    ylabel('Cooks Distance')
end
%Q is the new matrix with the outliers removed
Q=[];
len=length(N);
%Any points that lie under the cutoff Cook's Distance (mean +
cutoff*std)

for j=1:len
    if cook(j)<median(cook)+cutoff*std(cook)
        Q(end+1,:)=N(j,:);
    end
end

%Same as above, fiting the line and then calculating the delta.
[p S]=polyfit(Q(:,1),Q(:,2),1);
[y,delta]=polyval(p,Q(:,1),S);
delta_mat(2)=delta(1);
r_squared=sum((y-mean(Q(:,2))).^2)/sum((Q(:,2)-mean(Q(:,2))).^2);
%Plotting the new data set
subplot(2,3,2),
plot(Q(:,1),Q(:,2),'.',Q(:,1),y,'k',Q(:,1),y+delta,'r',Q(:,1),y-
delta,'r')
xlabel('Time (sec)')
ylabel('Degrees')
```

```
title('Final Iteration')
axis([0 time 0 500])
N=[];
N=Q;
end

freq=p(1)/(360)*1000;
freq_mat(2)=freq;

%*********************************************************************
%RE-EVALUATING THE ORIGINAL DATA POINTS BASED ON THE FINAL REGRESSION
%*********************************************************************

%R is a copy of the original data set (with zeros removed) from above

X=R(:,1);
%This takes the polynomial p, calculated in the last round of the above
%loop, and recaclulates the fitted values y for the full range of X
values
%in R.
y=polyval(p,X);
hat=X*inv(X.'*X)*X.';
sigma=sqrt(sum((R(:,2)-y).^2)/(length(R)-2));
epsilon=R(:,2)-y;
r_stud=epsilon./(sigma*sqrt(1-(diag(hat))));
cook=1/1*r_stud.^2.*(diag(hat)./(1-diag(hat)));
subplot(2,3,6),
plot(R(:,1),cook,'.',(0:1/x:max(R(:,1))),median(cook)+cutoff*std(cook),
'k--')
xlabel('Time (sec)')
ylabel('Cooks Distance')

%Q is the new matrix with the outliers removed
Q=[];
len=length(R);

%The cutoff for the final result is, instead of based on cook's
distance,
%based on distance from the best-fit line. The reason I do this,
instead of
%using the Cook's Distance, is because I'm no longer evaluating the
points.
%I'm simply trying to include all the points that lie on the line, and
%exclude all those that do not lie on it.
for j=1:len
    if R(j,2)>(y(j)-threshold)&&R(j,2)<(y(j)+threshold);
        Q(end+1,:)=R(j,:);
    end
end

%Same as above, fiting the line and then calculating the delta.
[p S]=polyfit(Q(:,1),Q(:,2),1);
[y,delta]=polyval(p,Q(:,1),S);
delta_mat(2)=delta(1);
r_squared=sum((y-mean(Q(:,2))).^2)/sum((Q(:,2)-mean(Q(:,2))).^2);
```

```
%Plotting the new data set
subplot(2,3,3),
plot(Q(:,1),Q(:,2),'.',Q(:,1),y,'k',Q(:,1),y+delta,'r',Q(:,1),y-
delta,'r')
xlabel('Time (sec)')
ylabel('Degrees')
title('Final Result')
axis([0 time 0 500])
N=[];
N=Q;
%final_size is the number of points used in the final data set
final_size=length(Q);
% %The slope of the line p(1) is in degrees/second. Dividing by 360
converts
% %degrees to rotations. Flipping the sign gives Hz. Multiplying by
1000
% %gives mHz.
% %freq is the rotational frequency in mHz.

freq=p(1)/(360)*1000;
freq_mat(3)=freq;
counter;
delta_mat;
r_squared;
freq_mat;
[freq_mat r_squared counter original_size final_size]
%csvwrite('data.csv', [name time x cutoff threshold freq_mat r_squared
counter original_size final_size])

end
```

C-2

Code for Calculating the Expected Dose-Response Curves for Sandwich Complex Based on Binding Kinetics

```
% The main program.  Based on the code written by Foad Mashayekhi for
BE110
% NMHW3 taught by Dr. Kamei at UCLA. The original files are in the
BE110
% folder in the 2011/04/28 Data folder. This uses a fixed step Euler
method
% and plots the output.  To run, place
% example.m, integrator3.m, solver.m, and deriv1.m in your current
MATLAB
% directory, then enter "example.m" into the MATLAB command window.

% This program attempts to model the binding kinetics of the two-site
% "sandwich" assay. There are 6 components: The protein (P), Capture
% Antibody (Q1), Detection Antibody (Q2), and three complexes (Q1P,
Q2P,
% and Q1PQ2).

% There are two primary reactions that take place:
% Q1 + P <-> Q1P (forward and reverse constants k1 and k2)
% Q1P + Q2 <-> Q1PQ2 (forward and reverse constants k3 and k4)

% And two secondary reactions that can also take place:
% Q2 + P <-> Q2P (k5 and k6)
% Q2P + Q1 <-> Q1PQ2 (k7 and k8)


clear all
clc

%Initial Concentrations
%MSC =  mother sphere concentration (spheres/uL)
MSC=1000;
%MSV = mother sphere volume (uL)
MSV=40;
%BC = bead concentration (mg/mL)
BC=1;
%BV = bead volume (uL)
BV=10;

Q1_naught=5.5e-10*0.027/831/1000*1e6*MSC;
Q2_naught=400e-12*BC*BV/1000/(150e-6);
%To set a single protein concentration value
% protein=1e-12;

% To create a dose-response curve for a range of protein concentration
```

```
% values
Pmin=1e-15;
Pmax=1e-8;
protein(1)=Pmin;
while protein<Pmax/10^0.125
    protein(end+1,1)=protein(end,1)*10^0.125;
end

for a=1:length(protein)
%This runs in two parts, representing the two steps of the sandwich
assay.
%This first part only concerns the equation Q1 + P <-> Q1P. After this
%equation reaches equilibrium, we will assume a complete wash. We will
%transfer the final concentrations of Q1 and Q1P to the second step,
and
%set the concentration of P to zero.

%***********************************
%Step 1
%***********************************

D = [Q1_naught 0 protein(a) 0 0 0]; % Sets the initial conditions for
Q1, Q2, P, Q1P, Q2P and Q1PQ2
%D(1)=Q1;
%D(2)=Q2;
%D(3)=P;
%D(4)=Q1P;
%D(5)=Q2P;
%D(6)=Q1PQ2;

ti = 0;     % Initial time
tf = 540;    % Final time
dt = 1;     % Step size
tout = 1;   % Time interval at which data points will be recorded

t = ti; % Initializes the time variable
tp = t; % Stores the time values for output
Dp = D; % Stores the solution values for output

% The while loop below continues executing the integration routine
until
% the independent variable, t, reaches its final value, tf.

while (t < tf)
    tend = t + tout;

    % This if statement corrects for situations where the interval
between
    % ti and tf isn't evenly divisible by the output interval.
    if (tend > tf)
        tend = tf;
    end
    h = dt;

    % Calls the "integrator3" function, which computes the solution for
```

```
    % a single output interval defined by "tout".
    [D,t] = integrator3(D,t,h,tend);
    tp = [tp ; t];  % Updates the array that stores time values for
output
    Dp = [Dp ; D];  % Updates the array that stores solution values for
output
end

%***********************************
%Step 2
%***********************************

%SET INITIAL CONCENTRATIONS OF Q2 HERE
D = [Dp(end,1) Q2_naught 0 Dp(end,4) 0 0]; % Sets the initial
conditions for Q1, Q2, P, Q1P, Q2P and Q1PQ2
%D(1)=Q1;
%D(2)=Q2;
%D(3)=P;
%D(4)=Q1P;
%D(5)=Q2P;
%D(6)=Q1PQ2;

ti = 0;     % Initial time
tf = 540;    % Final time
dt = 1;     % Step size
tout = 1;   % Time interval at which data points will be recorded

t = ti; % Initializes the time variable
tp = t; % Stores the time values for output
Dp = D; % Stores the solution values for output

% The while loop below continues executing the integration routine
until
% the independent variable, t, reaches its final value, tf.

while (t < tf)
    tend = t + tout;

    % This if statement corrects for situations where the interval
between
    % ti and tf isn't evenly divisible by the output interval.
    if (tend > tf)
        tend = tf;
    end
    h = dt;

    % Calls the "integrator3" function, which computes the solution for
    % a single output interval defined by "tout".
    [D,t] = integrator3(D,t,h,tend);
    tp = [tp ; t];  % Updates the array that stores time values for
output
    Dp = [Dp ; D];  % Updates the array that stores solution values for
output
end
```

```
Comp_conc(a,1)=Dp(end,6);

end

% This accounts for saturation of the mother spheres, and scales to
convert
% binding concentration to rotational frequency, based on a binding
capacity
% of the mother spheres of 300 beads.
for a=1:length(protein)
    if Comp_conc(a,1)>1.42e-9
        Comp_conc(a,1)=1.42e-9;
    end
end
Comp_conc=Comp_conc*7e11+2.5;


% Plots the model solutions.

semilogy(tp,Dp(:,1),':',tp,Dp(:,2),'--',tp,Dp(:,3),'-
',tp,Dp(:,4),'o',tp,Dp(:,5),'x',tp,Dp(:,6),'+')
legend('Q1','Q2','P','Q1P','Q2P','Q1PQ2')
xlabel('Time (sec)')
ylabel('Concentration (M)')
figure
semilogx(protein,Comp_conc)
xlabel('Protein Concentration (M)')
ylabel('Rotational Frequency (mHz)')



function [Dprime,t]=deriv1(D,t)

Dprime(1:6)=0;
%Remember that Kd=k2/k1

%For thrombin:
% k2=8.2e-4;
% k1=345125;
% k4=4.7e-3;
% k3=660289;
%Source: Muller, Freitag, et al., J. Thrombosis Hemostasis 6:2105-2112

%For Larry Gold's Aptamers:
k2=3.85e-4;
k1=k2/1e-11;
k4=k2;
k3=k1;

k5=k3;
k6=k4;
k7=k1;
k8=k2;

Q1=D(1);
```

```
Q2=D(2);
P=D(3);
Q1P=D(4);
Q2P=D(5);
Q1PQ2=D(6);

Dprime(1)=-k1*Q1*P+k2*Q1P-k7*Q1*Q2P+k8*Q1PQ2;
Dprime(2)=-k5*Q2*P+k6*Q2P-k3*Q1P*Q2+k4*Q1PQ2;
Dprime(3)=-k1*Q1*P+k2*Q1P-k5*Q2*P+k6*Q2P;
Dprime(4)=k1*Q1*P-k2*Q1P-k3*Q1P*Q2+k4*Q1PQ2;
Dprime(5)=k5*Q2*P-k6*Q2P-k7*Q2P*Q1+k8*Q1PQ2;
Dprime(6)=k3*Q1P*Q2+k7*Q2P*Q1-(k4+k8)*Q1PQ2;

end

function [dnew,tnew,error] = solver(D,t,h)


k1 = deriv1(D,t)*h;
k2 = deriv1(D+1/5*k1,t+1/5*h)*h;
k3 = deriv1(D+3/40*k1+9/40*k2,t+3/10*h)*h;
k4 = deriv1(D+44/45*k1-56/15*k2+32/9*k3,t+4/5*h)*h;
k5 = deriv1(D+19372/6561*k1-25360/2187*k2+64448/6561*k3-
212/729*k4,t+8/9*h)*h;
k6 = deriv1(D+9017/3168*k1-355/33*k2+46732/5247*k3+49/176*k4-
5103/18656*k5,t+h)*h;
k7 = deriv1(D+35/384*k1+500/1113*k3+125/192*k4-
2187/6784*k5+11/84*k6,t+h)*h;

d4 = D+5179/57600*k1+7571/16695*k3+393/640*k4-
92097/339200*k5+187/2100*k6+1/40*k7;

d5 = D+35/384*k1+500/1113*k3+125/192*k4-2187/6784*k5+11/84*k6;

tnew=t+h;

if 0.00001*d5(1) >= abs(d4(1)-d5(1))
    error=1;
else
    error=0;
end

dnew=d5;

end
```

```
% Computes the solution for the output interval specified by tout.

function [D,t] = integrator3(D,t,h,tend)

while (t < tend)

    % This if statement corrects for situations where the output
interval
    % isn't evenly divisible by the step size.
    if (tend - t < h)
        h = tend - t;
    end

    % Calls solver.m to compute a solution value for a given step size,
    % specified by "h".
    [Dnew,t,error] = solver(D,t,h);


    %This part deals with the error. The solver function checks the
error
    %against the given parameters, and returns a value of "1" if the
error
    %is too great. If a value of "1" is returned, then the step size is
    %reduced and is run again
    if error == 1
        h=h/2;
        [Dnew,tnew,error] = solver(D,t,h);
    end

    D = Dnew;

end
```

C-3

Code for Calculating Nearest-Neighbor Bead Angles and a Diffusion-Limited Aggregation Simulator

```
function beadfinder_ver2

%******************************
%COMMENTS
%******************************
%Written by Ariel Hecht, August 17, 2012
%A = Raw data matrix
%B = Thresholded data matrix
%C = Copy of B matrix to be manipulated in the section of the code
%converting raw x-y intensity values into bead positions
%D = Positions of Beads Matrix (m x 2 matrix)
%x = column value (corresponding to x-coordinate of bead)
%y = row value (corresponding to y-coordinate of bead)
%MATLAB does row first, column second
%******************************

%This version last revised 1/4/13

%INPUT IMAGE FILE
A = imread('4.64 pM 40x_0_120613-172925', 'bmp');

%BEAD POSITION OUTPUT FILE NAME
bead_output='junk.csv';

%ANGLE ARRAY OUTPUT FILE NAME
angle_output='junk.csv';

clc

%Size of a bead in pixels
bead_size=14;

radius_multiplier=1.75;

%Number of bins in histogram
bins=36;

%In case you need to chop out the first row/column
%A=A(:,:,1);
A=A(2:end,2:end,1);

%B contains an array of all pixel intensity values
B=double(A(:));
```

```
%SENSITIVITY THRESHOLD
%Threshold is intensity of pixels below which a pixel has to be to be
%considered as part of a bead.
upper_threshold=median(B)*0.75;
lower_threshold=median(B)*0.2;


dim=size(A);
height=dim(1);
width=dim(2);

C=zeros(((height+width)*2),2);

% B=double(reshape(A,1,height*width));
% figure
% hist(B,20)


%Takes each pixel, and checks the first layer of pixels around it (8 in
%total), and then checks the second layer of pixels around those (16 in
%total, so two degrees of neighbors away from the central point). If
the
%pixel is brighter than all the beads in the first row of neighbors,
and all
%the pixels in the second row of neighbors, then it is considered to be
the
%center of a bead.

index=0;
for j=3:height-2;
    for k=3:width-2;
        if A(j,k)<upper_threshold&&A(j,k)>lower_threshold;
            first_layer=[];
            first_layer(1)=A(j-1,k-1);
            first_layer(2)=A(j-1,k);
            first_layer(3)=A(j-1,k+1);
            first_layer(4)=A(j,k-1);
            first_layer(5)=A(j,k+1);
            first_layer(6)=A(j+1,k-1);
            first_layer(7)=A(j+1,k);
            first_layer(8)=A(j+1,k+1);
            second_layer=[];
            second_layer(1)=A(j-2,k-2);
            second_layer(2)=A(j-2,k-1);
            second_layer(3)=A(j-2,k);
            second_layer(4)=A(j-2,k+1);
            second_layer(5)=A(j-2,k+2);
            second_layer(6)=A(j-1,k-2);
            second_layer(7)=A(j-1,k+2);
            second_layer(8)=A(j,k-2);
            second_layer(9)=A(j,k+2);
            second_layer(10)=A(j+1,k-2);
            second_layer(11)=A(j+1,k+2);
            second_layer(12)=A(j+2,k-2);
```

```
            second_layer(13)=A(j+2,k-1);
            second_layer(14)=A(j+2,k);
            second_layer(15)=A(j+2,k+1);
            second_layer(16)=A(j+2,k+2);

            first=sort(first_layer,2,'descend');
            second=sort(second_layer,2,'descend');
                if A(j,k)>first(1);
                       if A(j,k)>second(1);
                            dist_mat=zeros(length(C),1);
                            for m=1:length(C)
                                dist_mat(m)=sqrt((C(m,1)-j)^2+(C(m,2)-
k)^2);
                            end

                            if min(dist_mat)>bead_size
                                index=index+1;
                                C(index,1)=j;
                                C(index,2)=k;
                            end
                       end
                end
        end
    end
end


%The first pass through this algorithm may not necessarily capture all
of
%the beads. This part of the program does a second run-through in order
to
%capture additional beads that may have failed the first time because
there
%may have been one neighboring pixel that was brighter. This run
through
%captures beads where in the first or second layer there were a few
pixels
%brighter than the central one, and then checks to see the distance
between
%beads to make sure that it won't overlap with another bead.
for j=3:height-2;
    for k=3:width-2;
        if A(j,k)<upper_threshold&&A(j,k)>lower_threshold;
            first_layer=[];
            first_layer(1)=A(j-1,k-1);
            first_layer(2)=A(j-1,k);
            first_layer(3)=A(j-1,k+1);
            first_layer(4)=A(j,k-1);
            first_layer(5)=A(j,k+1);
            first_layer(6)=A(j+1,k-1);
            first_layer(7)=A(j+1,k);
            first_layer(8)=A(j+1,k+1);
            second_layer=[];
            second_layer(1)=A(j-2,k-2);
            second_layer(2)=A(j-2,k-1);
            second_layer(3)=A(j-2,k);
```

```
            second_layer(4)=A(j-2,k+1);
            second_layer(5)=A(j-2,k+2);
            second_layer(6)=A(j-1,k-2);
            second_layer(7)=A(j-1,k+2);
            second_layer(8)=A(j,k-2);
            second_layer(9)=A(j,k+2);
            second_layer(10)=A(j+1,k-2);
            second_layer(11)=A(j+1,k+2);
            second_layer(12)=A(j+2,k-2);
            second_layer(13)=A(j+2,k-1);
            second_layer(14)=A(j+2,k);
            second_layer(15)=A(j+2,k+1);
            second_layer(16)=A(j+2,k+2);

            first=sort(first_layer,2,'descend');
            second=sort(second_layer,2,'descend');
                if xor(A(j,k)>=first(2),A(j,k)>=second(2))==1
                    dist_mat=zeros(length(C),1);
                    for m=1:length(C)
                        dist_mat(m)=sqrt((C(m,1)-j)^2+(C(m,2)-k)^2);
                    end

                    if min(dist_mat)>bead_size
                        index=index+1;
                        C(index,1)=j;
                        C(index,2)=k;
                    end
                end
        end
    end
end

D(1:index,1:2)=C(1:index,1:2);
num_beads=length(D)

% subplot(1,2,1),
figure
scatter(D(:,2),size(A,1)-D(:,1),35,'filled')
title('Position of Bead Centers')
xlabel('Pixels')
ylabel('Pixels')
axis([0 width 0 height])

%Creates an output data file
csvwrite(bead_output,D)

%R-squared calculation

mean_x=mean(D(:,2));
mean_y=mean(D(:,1));
r_squared=1/num_beads*sum((D(:,2)-mean_x).^2+(D(:,1)-mean_y).^2)

[NUMERIC,TXT]=xlsread('radius.xls');
NUMERIC;
TXT;
```

```
TXT(end+1,1)=cellstr(file_name);
TXT(end,2)=cellstr(datestr(now));
NUMERIC(end+1,1)=double(r_squared);

xlswrite('radius.xls',TXT,'Sheet1','A1');
xlswrite('radius.xls',NUMERIC,'Sheet1','C1');


%********************************
%This is the part of the program that calculates the angle between
beads
%********************************

anglearray=[];
%radius is the bead radius. The actual radius is about 5 for 1 um on
60x
%obj, but I increase it by 1 to make sure that all beads are included.


%This part of the program sets the radius from each bead center within
%which a bead would have to be to be considered a neighbor for angle
%calculation. The radius is 1.5 times the distance of the median of the
%nearest bead. This way, all neighbors are counted, without counting
%second-level neighbors.
master_distance=zeros(length(D),1);
for j=1:length(D);
    E=zeros(length(D),1);
    for k=1:length(D);
        E(k,1)=sqrt((D(j,1)-D(k,1))^2+(D(j,2)-D(k,2))^2);
    end
    F=sort(E);
    master_distance(j)=F(2);
end
radius=median(master_distance)*radius_multiplier


for j=1:length(D)-1;
    E=zeros(length(D),1); %Matrix E holds the distance between the
point j and all other points in the data set
    neighpos=[]; %position of neighbors in array
    calcbeads=[]; %the x-y coordinates of the beads that will be used
in the calculations

    %This loop calculates the distance between the point j and all
other
    %points in the array
    for k=1:length(D);
        E(k,1)=sqrt((D(j,1)-D(k,1))^2+(D(j,2)-D(k,2))^2);
    end

    %This loop checks to see if each point is within a one-bead radius
of
    %the point j, and puts all those that are within the array neighpos
%     for kk=1:length(E);
%         if E(kk,1)>radius;
```

```
%             E(kk,1)=0;
%         elseif E(kk,1)<radius && E(kk,1)>0;
%             neighpos(end+1)=kk;
%         end
%     end

    for kk=1:length(E);
        if E(kk,1)<radius && E(kk,1)>0.4*radius;
            neighpos(end+1)=kk;
        end
    end

    %calcbeads is the array into which the point j is placed in the
first row,
    %and all other neighboring points are populated into the array
    calcbeads(1,1)=D(j,1);
    calcbeads(1,2)=D(j,2);
    for m=neighpos;
        calcbeads(end+1,1)=D(m,1);
        calcbeads(end,2)=D(m,2);
    end

    %This loop calculates the angle between the point j and all other
    %points using the distance formula and the law of cosines. the
angle
    %values are populated into anglearray, from which the histogram is
    %generated.

    if length(calcbeads)>=3
    for n=2:length(calcbeads)-1;
        for p=n+1:length(calcbeads);
            dist_a=sqrt((calcbeads(1,1)-
calcbeads(n,1))^2+(calcbeads(1,2)-calcbeads(n,2))^2);
            dist_b=sqrt((calcbeads(1,1)-
calcbeads(p,1))^2+(calcbeads(1,2)-calcbeads(p,2))^2);
            dist_c=sqrt((calcbeads(n,1)-
calcbeads(p,1))^2+(calcbeads(n,2)-calcbeads(p,2))^2);
            angle=acos((dist_a^2+dist_b^2-
dist_c^2)/(2*dist_a*dist_b))*180/pi;
            anglearray(end+1,1)=angle;
%             if angle<50;
%                 [calcbeads(1,1) calcbeads(1,2) calcbeads(n,1)
calcbeads(n,2) calcbeads(p,1) calcbeads(p,2) angle]
%             end
        end
    end
    end

end


length(anglearray)

figure
hist(anglearray,bins)
```

```
xlabel('Angle (degrees)')
title('Distribution of Bead Angles')
xlim([0 180]);

csvwrite(angle_output,anglearray)

end



function dla_beads

radius=2.5; %radius of one bead
number=1000; %number of beads in sim
dim=500; %dimension of square

bead_centers=[dim/2 dim/2];

for m=2:number

    %Determining the starting position of the new bead. Each bead
starts in
    %one of the four corners
    x_start=round(rand);
    y_start=round(rand);
    m_pos=[dim*x_start dim*y_start];

    %Initializes a bunch of variables for the loop.
    %Collision=0 means there have been no collisions
    %Collision=1 means that there has been a collision

    collision=0;
    collision_coordinates=[];
    moves=0;
    reseeds=0;

    while collision==0

        D=size(bead_centers);

        %The movement is on the range [-1 1]
        x_move=-1+2*rand;
        y_move=-1+2*rand;

        %Moves the bead based on the random movement
        m_pos(1)=m_pos(1)+x_move;
        m_pos(2)=m_pos(2)+y_move;

        %Checks to see if the bead has moved out of the grid, and if it
        %has, moves it back into the grid
        if m_pos(1)>dim || m_pos(1)<0
            m_pos(1)=m_pos(1)-2*x_move;
            reseeds=reseeds+1;
        end
```

```
        if m_pos(2)>dim || m_pos(2)<0
            m_pos(2)=m_pos(2)-2*y_move;
            reseeds=reseeds+1;
        end

        %Checks to see if a collision has occured; if it has, the whole
        %while loop terminates
        for n=1:D(1)
            if 2*radius >= sqrt((m_pos(1)-
bead_centers(n,1))^2+(m_pos(2)-bead_centers(n,2))^2)
                collision=1;
            end
        end
    end

    %Once a collision has occured, this moves the bead back along the
    %direction of its final movement, by 1% of the final movement
length,
    %before the collision, until it is no
    %longer colliding with another bead
    while collision==1;
        x_adj=0.01*x_move;
        y_adj=0.01*y_move;
        m_pos(1)=m_pos(1)-x_adj;
        m_pos(2)=m_pos(2)-y_adj;
        collision=0;
        for n=1:D(1)
            if 2*radius >= sqrt((m_pos(1)-
bead_centers(n,1))^2+(m_pos(2)-bead_centers(n,2))^2)
                collision=1;
            end
        end
    end

    %The final position of the bead is recorded in the bead_centers
array,
    %which is the master array for the function
    bead_centers(end+1,1)=m_pos(1);
    bead_centers(end,2)=m_pos(2);

end

% creates a plot of bead positions. circle is a user-defined function
that
% must be copied into the same directory as the dla_beads function
for z=1:length(bead_centers)
    hold on
    circle(bead_centers(z,1),bead_centers(z,2),radius)
end

csvwrite('dlabeadpos.csv',bead_centers)

end
```